

**SYNTHESIS, FABRICATION, AND PERFORMANCE
EVALUATION OF A SELF-POWERED, HETEROSTRUCTURE,
METAL HALIDE PEROVSKITE-BASED, PHOTODETECTOR**

BY

ABDURRAHMAN IMAM

A Thesis Presented to the

COLLEGE OF GRADUATE AND INTERDISCIPLINARY STUDIES

KING FAHD UNIVERSITY OF PETROLEUM & MINERALS

DHAHRAN, SAUDI ARABIA

In Partial Fulfillment of the
Requirements for the Degree of

MASTER OF SCIENCE

In

PHYSICS

MAY 2024

KING FAHD UNIVERSITY OF PETROLEUM & MINERALS

DHAHRAN- 31261, SAUDI ARABIA

DEANSHIP OF GRADUATE STUDIES

This thesis, written by **AbdurRahman Imam** under the direction of his thesis advisor and approved by his thesis committee, has been presented and accepted by the Dean of Graduate Studies, in partial fulfillment of the requirements for the degree of **MASTER OF SCIENCE IN PHYSICS**.



Dr. Muhammad Ashraf Gondal
(Advisor)



Dr. Mohammad F. Al-Kuhaili
Department Chairman



Dr. Abdelkarim Mustafa Mekki
(Member)



Dr. Suliman Saleh Al-Homidan
Dean of Graduate Studies



Dr. Saleem Ghaffar Rao
(Member)

Date



© AbdurRahman Imam

2024

Dedication

To my family, whose love and support have been my anchor throughout this journey, I dedicate this thesis with heartfelt gratitude.

ACKNOWLEDGMENTS

Alhamdulillah. In the name of Allah, the Most Beneficent, the Most Merciful. All praise is due to Allah, the Lord of all worlds. May the blessings and peace of Allah be upon our noble Prophet Muhammad, his households, companions, and all those who follow their righteous path until the last day.

I begin by expressing my heartfelt gratitude to Almighty Allah for bestowing upon me the strength and resources needed to embark on and complete this challenging journey of thesis research.

I extend my sincere appreciation to King Fahad University of Petroleum and Minerals for providing an environment conducive to academic excellence.

A special acknowledgment goes to my esteemed thesis supervisor, Distinguished Professor Muhammed Ashraf Gondal, whose unwavering support, and guidance played a pivotal role in the successful completion of this work. I am also grateful to my committee members, Dr. Abdelkarim Mustafa Mekki and Dr. Salem Ghaffar Rao, for their valuable contributions and support throughout the research process.

I extend my sincere gratitude to the Department of Physics under the chairmanship of Dr. **Mohammad F. Al-Kuhaili**, for providing a nurturing academic environment that fostered growth and excellence throughout my journey.

I am grateful for the encouragement and wisdom provided by my lecturers at KFUPM, shaping my academic journey. I would like to express my deepest gratitude to my family, especially my beloved Mum, Saudatu Yusuf and wife-Amina Yahaya, for their unending support, understanding, and encouragement. Your love has been my pillar of strength.

I also want to acknowledge the immense support and motivation provided by my friends, particularly Dr. Yakubu Sani Wudil, a senior colleague whose technical guidance was invaluable.

Additionally, my heartfelt thanks go to the Nigerian community (NCUPM) in KFUPM for fostering a sense of belonging and providing a supportive network during my academic journey. Your camaraderie has enriched my experience.

In conclusion, I acknowledge with deep appreciation all those who have played a role, whether big or small, in the realization of this academic milestone. May Allah bless you abundantly for your contributions and support.

Alhamdulillah. |

TABLE OF CONTENTS

ACKNOWLEDGEMENTS.....	v
TABLE OF CONTENTS.....	vi
LIST OF TABLES.....	ix
LIST OF FIGURES.....	x
LIST OF ABBREVIATIONS.....	xiii
ABSTRACT.....	xv
ملخص الرسالة	xvi
CHAPTER 1: INTRODUCTION.....	1
1.1 Perovskite Materials and Their Potentials in Photodetection.....	1
1.2 Objective of the Research.....	4
CHAPTER 2: LITERATURE REVIEW.....	6
2.1 The Perovskite Materials.....	6
2.2 History of Metal Halide Perovskite Studies.....	13
2.3 MHPs Composition, Crystal Structure, Properties, and Classifications.....	15
2.3.1. Composition of MHPs.....	15
2.3.2. Crystal structure of MHPs.....	17
2.3.3. Properties of MHPs.....	22
2.3.4. Classification of MHPs.....	27
2.3.5. Discrepancies in Naming Halide Perovskites, HPs.....	28

2.4	Photodetector Physics.....	30
2.5	Classification of Photodetectors.....	33
2.5.1	Photodiodes.....	34
2.5.2	Phototransistors.....	34
2.5.3	Photonic Detectors.....	35
2.5.4	Infrared Detectors.....	35
2.5.5	Photoconductors.....	35
2.6	Photodetector Performance Metrics.....	36
2.6.1	Quantum efficiency.....	36
2.6.2	Responsivity.....	42
2.6.3	Noise- Equivalent Power (NEP).....	45
2.6.4	Detectivity.....	47
2.6.5	Dark Current.....	49
2.6.6	Gain.....	49
2.6.7	Linear Dynamic Range.....	50
2.6.8	Response Time.....	52
2.7	Noise In Photodetection.....	53
2.7.1	Thermal Noise (Johnson-Nyquist Noise)	53
2.7.2	Shot Noise.....	54
2.7.3	Flicker Noise (1/f Noise)	54
2.7.4	Amplifier Noise.....	54
CHAPTER 3: MATERIALS AND METHODS.....		56
3.1	Experimental Procedures.....	56
3.2	Material Synthesis.....	56
3.2.1	Synthesis of MAPbI ₃	56
3.2.2	Preparation of mesoporous and compact TiO ₂	57
3.2.3	Preparation of Ni ₂ O ₃ solution.....	57
3.3	Fabrication processes.....	57

3.3.1	Fabrication of Photodetector Based on NF and NN Faces.....	57
3.3.2	Photodetectors Based on T, N, and NN Faces.....	59
3.4	Material Characterizations.....	63
3.5	Device Characterizations.....	64
CHAPTER 4: RESULTS AND DISCUSSIONS.....		66
4.1	Assessment of the Material Properties.....	66
4.1.1	Morphological Investigation of Perovskite Films.....	66
4.1.2	Crystal Structure Analysis.....	68
4.1.3	Electronic Structure and Elemental Investigations.....	71
4.1.4	Optoelectrical Characterizations of the Material.....	74
4.1.5	Charge Transfer and Recombination Mechanisms.....	79
4.2	Current-Voltage (I-V) Characteristics Assessment of the Fabricated Photodetectors.....	80
4.2.1	I-V Characteristics Analysis of PDs Fabricated with Different LiI Concentrations.....	81
4.2.2	I-V Characteristics Analysis of PDs Fabricated with Single- and Double-Absorber Layer Configurations.....	86
4.3	Photodetector Figures of Merit.....	90
4.3.1	Figures of Merit of PDs Fabricated with Different LiI Concentrations.....	91
4.3.2	Figures of Merit of PDs with Single and Double-Absorber Layer Configurations.....	96
4.4	Performance Evaluations of This Work.....	100
4.5	Comparison With the Existing Literature.....	101
CHAPTER 5: CONCLUSIONS.....		106
Recommendation for Further Studies.....		108
References.....		110
Vitae.....		132

LIST OF TABLES

Table 1: Classifications of perovskite materials according to their X-site.....	8
Table 2: Ionic radii of typical metal halide perovskite ions.....	20
Table 3: Figures of merit for the fabricated photodetectors in this work.....	94
Table 4: Figures of merit for the fabricated photodetectors in this work.....	98
Table 5: Figures of merit from existing literature.....	105

LIST OF FIGURES

Figure 1: (a) CaTiO ₃ rock crystals; (b) Crystal structure of CaTiO ₃ perovskite.....	7
Figure 2: (a) ABX ₃ crystal structure of metal halide perovskite, where permutations between ions at A, B and X sites occur ⁵⁹ ; (b) Hypothetical model of CsPbI ₃ , Cs ₂ PbI ₄ , Cs ₃ PbI ₅ , and Cs ₄ PbI ₆ crystal structures ¹²³	15
Figure 3: (a) colloidal solutions in toluene under UV lamp ($\lambda = 365$ nm); (b) representative PL spectra ($\lambda_{exc} = 400$ nm for all but 350 nm for CsPbCl ₃ samples); (c) typical optical absorption and PL spectra; (d) time-resolved PL decays for all samples shown in (c) except CsPbCl ₃	17
Figure 4: Overview of different halide perovskites. (a) Standard ABX ₃ cubic halide perovskites. (b) Antiperovskites, with A being a monovalent metal (like Li ⁺ or Ag ⁺), X a halide, and Y a chalcogenide. (c) Common orthorhombic and tetragonal disordered perovskites, arising from the tilting of the octahedra. (d) Vacant BX ₃ perovskites, like AlF ₃ . (e) Ordered perovskites, where two M(II) metals are replaced by a M(I) and M(III) metal. (f) Vacancy-ordered perovskites, where a part of the B-site cations is replaced with an M(III) or M(IV) and vacancies.....	18
Figure 5: Overview of ternary metal halides not crystallizing in a perovskite structure. (a) Post-perovskites formed by ABX ₃ ternary metal halides that would form stable perovskites at higher temperatures/pressures. (b) Ternary M(II) halides with non-perovskite stoichiometries, including inorganic Ruddlesden–Popper metal halide (A ₂ BX ₄), A ₄ BX ₆ , and AB ₂ X ₅ phases. (c) Ternary bismuth halides not crystallizing in vacancy-ordered perovskites, including the isolated dimer structure (Cs ₃ Bi ₂ I ₉) and isolated octahedra (Cs ₃ BiX ₆). (d) Several ternary M(I) and M(II) (mainly transition metal and F ⁻ and Cl ⁻) phases are based on MX ₄ tetrahedra.....	19
Figure 6: Perovskite ABX ₃ cubic structure. b) Structural map of ABI ₃ compounds. Blue dots and red crosses represent stable inorganic perovskites and nonperovskites.....	21
Figure 7: Schematic representation of the Working principle of a PIN photodetector (photodiode) with an applied reverse bias.....	33
Figure 8: (a) Comparison of EQE of three types of solar cells; (b) EQE of perovskite solar cell and AM1.51 (a) spectral response for the b-Si photodiode compared with violet- and infrared-optimized photodiodes from the Hamamatsu commercial manufacturer; (b) EQE of b-Si photodiode compared with violet- and infrared-optimized photodiodes.....	40
Figure 9: Schematic of the synthesis of undoped and Li-doped perovskite material and fabrication processes of photodetectors based on NF and NN-faces.....	58
Figure 10: Proposed device architecture based on NF and NN-faces.....	59

Figure 11: Schematic of the synthesis of undoped and Li-doped perovskite material and fabrication processes of photodetectors based on T, N, and NN-faces.....	58
Figure 12: The proposed device architectures based on T, N, and NN faces.....	62
Figure 13: (a-e) Top view of the NF -faces and NN-faces (inset) of the fabricated devices based on FTO/c-TiO ₂ /m-TiO ₂ /MAPbI ₃ and FTO/Ni ₂ O ₃ /MAPbI ₃ configurations respectively, with different molar concentrations of LiI additive, (f) 5 mol% LiI @ 5 μm	67
Figure 14: (a) EDX spectra of a face with 0 mol% LiI and (b) EDX spectra of a face with 7 mol% LiI...	68
Figure 15: X-ray diffraction patterns (a) NF-faces (b) NN-faces.....	70
Figure 16: Zoomed in on the XRD spectra of two representative peaks of (a) NF-faces (110), and (b) NN-faces (224); (c) The d-spacing of the NF- and NN-faces plotted from the peaks of (110) and (224) respectively.....	70
Figure 17: (a) XPS wide scan spectra of the NF-faces and NN-faces with 5 mol% LiI compared to the sample with 0 mol% LiI. (b) XPS scans of the Pb4f measured for un-doped and Li-doped samples (c) I3d XPS core level spectra (NF-faces), and (d) N1s core level spectra (NN-faces)	73
Figure 18: (a) XPS wide scan spectra of the NN-faces; (b) XPS scans of the Pb 4f measured for un-doped and Li-doped samples (c) I 3d XPS core level spectra (NN-faces), and (d) N 1s core level spectra (NN-faces)	74
Figure 19: Absorbance spectra of (a) NF-faces based on FTO/c-TiO ₂ /m-TiO ₂ /MAPbI ₃ : Li, (b) NN-faces based on FTO/Ni ₂ O ₃ /MAPbI ₃ : Li.....	77
Figure 20: Photoluminescence spectra (a) NF-faces based on FTO/c-TiO ₂ /m-TiO ₂ /MAPbI ₃ : Li, (b) NN-faces based on FTO/Ni ₂ O ₃ /MAPbI ₃ : Li.....	78
Figure 21: (a) Energy band structure alignment showing charge transfer mechanisms; (b) Proposed radiative and non-radiative recombination mechanisms.....	80
Figure 22: Current-voltage (i-v) characteristics for the NF-faces of the fabricated photodetectors: (a) PD0 (0 mol% LiI) (b) PD2 (2 mol% LiI) 9c) PD5 (5 mol% LiI) (d) PD7 (7 mol% LiI) (e) PD10 (10 mol% LiI), and (f) Comparison between the measured dark current.....	83
Figure 23: Current-voltage characteristics for the NN-faces of the fabricated photodetectors: (a) PD0 (0 mol% LiI) (b) PD2 (2 mol% LiI) 9c) PD5 (5 mol% LiI) (d) PD7 (7 mol% LiI) (e) PD10 (10 mol% LiI), and (f) Comparison between the measured photocurrent under 0.2 mW/cm ² illumination.....	84
Figure 24: Current-voltage (i-v) characteristics for the PDOs of the fabricated photodetectors: (a) PD0-A (T-face), (b) PDO-A (N-face), (c) PD-B (T-face), and (d) PDO-B (NN-face).....	89

Figure 25: Current-voltage (i-v) characteristics for the fabricated PD5s: (a) PD5-A (T-face), (b) PD5-A (N-face), (c) PD5-B (T-face), and (d) PD5-B (NN-face)**90**

Figure 26:(a-e) Transient photoresponse of the photodetectors corresponding to optical switching conditions. (f) Estimation of Rise and Fall times during light ON and OFF times. (g) Combined i-t curves for NF-faces, and (h) combined i-t curves for the NN-faces.....**95**

Figure 27:(a-d) Transient photoresponse (i-t curves) for the fabricated PDs; (e-f) combined normalized i-t curves for the faces of the fabricated PDs.....**99**

LIST OF ABBREVIATIONS

MHPs	:	Metal halide perovskites
LEDs	:	Light emitting diodes
FTO	:	Fluorine doped titanium oxide.
HTL	:	Hole transport layer
ETL	:	Electron transport layer
PDs	:	Photodetectors
XRD	:	X-ray diffraction
PLQE	:	Photoluminescence quantum efficiency
MA	:	Methylammonium
FA	:	Formamidinium
PEA	:	Phenethyl-ammonium
NMHPs	:	Not-metal halide perovskites
DFT	:	Density-functional theory
TRPL	:	Time-resolved photoluminescence
PL	:	Photoluminescence
SHG	:	Second-Harmonic Generation
FWM	:	Four-Wave Mixing
HPs	:	Halide Perovskites
IUCr	:	International Union of Crystallography
NIST	:	National Institute of Standards and Technology
PMT	:	Photomultiplier Tubes
SPAD	:	Single-Photon Avalanche Diodes
QE	:	Quantum efficiency

SNR	:	Signal-to-noise ratio
EQE	:	External quantum efficiency
R	:	Responsivity
IQE	:	Internal quantum efficiency
NEP	:	Noise-Equivalent Power
D*	:	Detectivity
LDR	:	Linear dynamic range
DMF	:	Dimethylformamide
DMSO	:	Dimethyl sulfoxide
PTFE	:	Polytetrafluoroethylene
XPS	:	X-ray photoelectron spectroscopy
FESEM	:	Field emission scanning electron microscopy
EDX	:	Energy-dispersive X-ray spectroscopy
UV-vis	:	Ultraviolet-Visible
VBM	:	Valence band maxima
WF	:	Work function
CBM	:	Conduction band maxima

ABSTRACT

Full Name : [AbdurRahman Imam]

Thesis Title : [Synthesis, Fabrication, and Performance Evaluation of a Self-Powered, Heterostructure, Metal Halide Perovskite-Based, Dual-faced Photodetector]

Major Field : [Physics]

Date of Degree : [April, 2024]

This research presents a comprehensive investigation into the synthesis, fabrication, and performance evaluation of a novel self-powered, heterostructure metal halide perovskite (MHPs)-based dual-faced photodetector with a focus on optimizing the optoelectronic properties of the photodetector through innovative material synthesis and device engineering strategies. The study undertakes a systematic investigation into the impact of doping concentrations on the performance of MHPs-based photodetectors. Through comprehensive experimentation, various doping levels of lithium iodide (LiI) to discern their effects on device characteristics, including responsivity, detectivity, and response time were explored. Additionally, the influence of device architecture, comparing single-absorber layer and double-absorber layer (tandem) configurations to elucidate their respective advantages and limitations was also studied. This approach allows us to gain deeper insights into the intricate interplay between doping concentration, device architecture, and optoelectronic performance, facilitating the optimization of photodetector designs for enhanced functionality and efficiency. Furthermore, detailed characterizations, including SEM analysis, UV-visible spectroscopy, and current-voltage (I-V) measurements, provide insights into the underlying mechanisms driving device performance. The correlation between material properties, device architecture, and performance metrics elucidates the intricate interplay between doping concentration, crystallinity, and charge transport properties. Performance evaluations reveal significant advancements in photodetector technology. Notably, PD5, incorporating 5 mol% LiI doping, and a single-absorber layer emerges as the top-performing device, exhibiting exceptional responsivity (512.58 mA/W), detectivity (5.06×10^{11} Jones), and a rapid rise/fall time (167/197 ms). The device also demonstrates a high external quantum efficiency (EQE) of 115.78%, underscoring its superior performance in converting incident photons into electrical signals. The findings presented in this thesis not only advance our understanding of metal halide perovskite-based photodetectors but also underscore their potential for diverse applications, including imaging sensors, environmental monitoring systems, and optical communication networks. The outstanding performance of PD5 serves as a testament to the efficacy of innovative doping strategies and device engineering in enhancing photodetection capabilities, laying the groundwork for future advancements in this rapidly growing field.

ملخص الرسالة

الاسم الكامل: عبد الرحمن امام

عنوان الرسالة: التوليف والتصنيع وتقييم الأداء لكاشف ضوئي ثنائي الوجه يعمل بالطاقة الذاتية، ذو بنية متغايرة، قائم على معدن الهاليد البيروفسكايت

التخصص: الفيزياء

تاريخ الدرجة العلمية: أبريل 2024

تقدم هذه الأطروحة بحثاً شاملاً في التوليف والتصنيع وتقييم الأداء لكاشف ضوئي مزدوج الوجه يعمل بالطاقة الذاتية ومتغاير هيكل هاليد بيروفسكايت مع التركيز على تحسين الخصائص الإلكترونية الضوئية للكاشف الضوئي من خلال تخليق المواد المبتكرة. واستراتيجيات هندسة (MHPs) المعدني من خلال التجارب MHP. تجرى الدراسة تحقيقاً منهجياً في تأثير تركيزات المنشطات على أداء أجهزة الكشف الضوئية المعتمدة على لتمييز آثارها على خصائص الجهاز، بما في ذلك الاستجابة، والكشف، (LiI) الشاملة، تم استكشاف مستويات المنشطات المختلفة من يوديد الليثيوم وزمن الاستجابة. بالإضافة إلى ذلك، تمت أيضاً دراسة تأثير بنية الجهاز، ومقارنة تكوينات طبقة الامتصاص المفردة وطبقة الامتصاص المزدوجة (ترادفية) لتوضيح المزايا والقيود الخاصة بكل منهما. يتيح لنا هذا النهج الحصول على رؤى أعمق حول التفاعل المعقد بين تركيز المنشطات، وبنية الجهاز، والأداء الإلكتروني البصري، مما يسهل تحسين تصميمات الكاشف الضوئي لتعزيز الوظائف والكفاءة. علاوة على ذلك، فإن التوصيفات، توفر نظرة ثاقبة للآليات الأساسية (IV)، والتحليل الطيفي للأشعة فوق البنفسجية المرئية، وقياسات الجهد الحالي SEM التفصيلية، بما في ذلك تحليل التي تقود أداء الجهاز. توضح العلاقة بين خصائص المواد، وبنية الجهاز، ومقاييس الأداء التفاعل المعقد بين تركيز المنشطات، والبلورة، وخصائص، الذي يشتمل على 5 مول% من PD5 نقل الشحنة. تكشف تقييمات الأداء عن تطورات كبيرة في تكنولوجيا الكاشف الضوئي. ومن الجدير بالذكر أن، وطبقة امتصاص مفردة، يظهر كجهاز عالي الأداء، ويظهر استجابة استثنائية (512.58 مللي أمبير/واط)، واكتشاف (LiI 1011 × 5.06) المنشطات تبلغ 115.78%، مما يؤكد (EQE) جونز)، وأوقات صعود/هبوط سريعة (197/167 مللي ثانية). ويظهر الجهاز أيضاً كفاءة كمية خارجية عالية أدائه المتفوق في تحويل الفوتونات الساقطة إلى إشارات كهربائية. النتائج المقدمة في هذه الأطروحة لا تؤدي فقط إلى تعزيز فهمنا لأجهزة الكشف الضوئية المعتمدة على الهاليد المعدني والبيروفسكايت ولكنها تؤكد أيضاً على إمكاناتها في التطبيقات المتنوعة، بما في ذلك أجهزة استشعار التصوير بمثابة شهادة على فعالية استراتيجيات المنشطات المبتكرة وهندسة PD5 وأنظمة المراقبة البيئية وشبكات الاتصالات البصرية. يعد الأداء المتميز لـ الأجهزة في تعزيز قدرات الكشف الضوئي، ووضع الأساس للتقدم المستقبلي في هذا المجال سريع التطور.

CHAPTER 1

INTRODUCTION

1.1 Perovskite Materials and Their Potentials in Photodetection

The current semiconductor market, particularly in photovoltaics, is largely dominated by silicon-based devices^{1,2}. However, the elevated temperatures necessary for manufacturing silicon devices not only incur additional costs but also lead to the emission of greenhouse gases, which have detrimental effects on the atmosphere and the environment^{3,4}. In the search for alternatives to supplant the prevailing silicon-based technology, Organo metal halide perovskites, or simply metal halide perovskites (MHPs) such as methylammonium lead iodide ($\text{CH}_3\text{NH}_3\text{PbI}_3$), have emerged as promising contenders among various material options. This is primarily due to their outstanding structural, optical, and electronic properties^{5,6}. Some of these properties include a direct band gap that can be adjusted by altering the chemical composition⁷⁻⁹, or the arrangement of atoms within the crystal lattice¹⁰, high carrier mobility^{11,12}, a high optical absorption coefficient^{13,14}, a substantial diffusion length¹⁵⁻¹⁷, and ambipolar charge transport^{18,19}. These characteristics positioned halide perovskites as potential candidates for the development of environmentally friendly and versatile semiconductor devices²⁰. Furthermore, their ability to be manufactured at ambient temperatures and pressures, using low-cost, readily available materials, makes the production process relatively straightforward and cost-effective²¹.

However, it's important to note that solution-processed perovskite films often exhibit trap states with a typical density in the range of $\sim 10^{15}$ – 10^{16} cm^{-3} . This density is comparable to the density of photo-generated or photo-injected carriers within the working conditions of solar cells or LEDs^{22,23}. These trap states have a detrimental effect as they capture carriers, leading to subsequent non-radiative recombination. Consequently, this results in relatively low photoluminescence quantum yields, particularly in the case of methylammonium lead iodide perovskite (MAPbI₃) films. Therefore, there is a pressing need for material modifications through doping or other mechanisms aimed at enhancing the luminescent properties and overall device performance. The process of doping holds immense significance in the realm of semiconducting thin-film electronic devices. Its primary role is to establish an effective flow of charge carriers and enhance overall transport capabilities. Dopants, which serve as either donors or acceptors of charge, are typically introduced during the synthesis or deposition phase of semiconductor thin films. Alternatively, they can be incorporated through subsequent processes such as diffusion or implantation. There are two main approaches to mitigate nonradiative recombination: surface passivation and doping. Surface passivation has been extensively explored^{24,25}, involving the treatment or coating of perovskite films with various chemicals. However, this method has limitations when it comes to addressing trap states within the bulk of the material. Interestingly, in solution-processed perovskite films, the density of bulk traps can be similar to that at the surface or interfaces²⁶. This raises the significance of doping as a promising solution because it can effectively modify both the surface/interfacial and bulk properties of the material.

Recently, alkali metal doping has shown promise as an effective means of reducing nonradiative losses in perovskites ^{27,28}. The role of alkali metals (such as potassium and lithium) is often described as passivating the surface and grain boundaries. In these cases, alkali metals serve as additives rather than embodying the true essence of semiconductor doping. Semiconductor doping, in principle, involves the incorporation of dopant atoms into the host lattice, either in substitutional or interstitial positions. Thus, many studies claiming to employ doping in perovskites have essentially dealt with additives until now.

Lithium doping of MHPs has been the subject of several investigations ²⁹⁻³⁶. In a comprehensive study conducted by Cao and colleagues ³³, they examined the introduction of extrinsic alkali cations, including lithium, into perovskite materials, employing both experimental and theoretical approaches. Their findings revealed that these alkali cations take up interstitial positions within the perovskite structure, effectively curbing the migration of iodine ions. This interstitial occupancy implies that the alkali cations particularly lithium, can function as n-type dopants and introduce energy levels within the bandgap. Recent research has even showcased an augmentation in conductivity within lithium-doped perovskites ^{32,37}. Furthermore, it has been demonstrated that lithium doping can elicit a spectrum of effects on perovskite properties, encompassing alterations in their structural attributes ³³, electrical conductance ³⁷, diamagnetic behavior ³², and optical absorption properties ³². Despite these insights, the precise role of lithium in influencing carrier recombination processes and the intricate mechanisms underpinning these effects, which hold significant implications for comprehending the photo-physics within doped perovskite materials, remain largely unexplored.

Our study entails an in-depth assessment of the performance of an optimized vertical structure photodetector fabricated from Li-doped MAPbI₃, featuring both upper and lower FTO electrodes. In this configuration, incident light is directed through the transparent top and bottom FTO electrodes, traversing a structure comprising a hole transport layer (HTL), hole blocking layer (HBL), and electron transport layer (ETL), with dual absorber layers interposed between them. Previous research has observed notable benefits in vertical structure photodetectors (PDs), including efficient operation at low voltage, high responsivity, and rapid response times, attributed to diminished trap density and reduced carrier diffusion distances within these structures³⁸⁻⁴¹. This research strategically doped MAPbI₃ with Li ions and optimized diverse parameters pertaining to the absorber layer, ETL, and HTL, aiming to realize exceptional device performance. Significantly, the performance of the device is frequently dictated by the presence and impact of defects within these layers and at their interfaces, as defects markedly facilitate the facile recombination of generated photocarriers within the device.

1.2 Objectives of the Research

The main objectives of the proposed work are as follows:

- To synthesize metal halide perovskite materials using solution synthesis and thin-film deposition techniques.
- To characterize the material using various techniques such as scanning electron microscopy, X-ray diffraction, UV-visible spectroscopy, and photoluminescence spectroscopy.

- To fabricate and optimize the structure of the self-powered, heterostructure metal halide perovskite-based photodetector with multi-facial configuration.
- To evaluate the performance of the fabricated device in terms of its sensitivity, response time, and stability under different lighting conditions.
- To compare the performance of the self-powered, heterostructure metal halide perovskite-based, dual-faceted photodetector with that of other photodetectors in the literature.

CHAPTER 2

LITERATURE REVIEW

2.1 The Perovskite Materials

Perovskites are groups of chemicals with crystal structures similar to the CaTiO_3 rock crystals^{42,43} (Figure 1a-b) identified in the Ural Mountains of Russia by Gustav Rose in 1839, named after Russian mineralogist Lev Perovski (1792–1856)^{44–46}. Based on the chemical formula of the parent mineral, perovskites can be defined as compounds with the empirical formula ABX_3 ; where A is an organic/in-organic cation (e.g., $[\text{CH}_3\text{NH}_3]^+$, $[(\text{NH}_2)_2\text{CH}]^+$, $[\text{CH}_3\text{CH}_2\text{NH}_3]^+$, Ca^{2+} , Ba^{2+} , Cs^{2+} , K^+ , Rb^+ , La^+ , etc.), B is either an organic/inorganic cation (e.g., NH_4^+ , Li^+ , Pb^{2+} , Sn^{2+} , Bi^{2+} , Sr^{2+} , Cu^{2+} , Mn^{2+} , Ge^{2+} , Cd^{2+}) whose size is less than that of A, and X can be an oxide (O^{2-}), halide (Cl^- , I^- , and Br^-), sulfide (S^{2-}), nitride (N^{3-}), telluride (Te^{2-}), selenide (Se^{2-}), or hydride (H^-) anions^{47–49}.

Perovskites can be classified into three categories: all-organic, all-inorganic, and organic-inorganic (hybrid) materials. The categorization is based on the choice of cations in the ABX_3 crystal structure, where permutations between ions at A and B sites occur (Figure 2a)^{43,47,50}. Among these categories, all-organic perovskites, which involve organic cations at A and B sites, are the least commonly studied. A recent study by A. Stoddart focused on all-organic perovskites for ferroelectric applications, utilizing a divalent organic cation (such as N-methyl-N'-diazabicyclo [2.2.2] octonium) at the A site, ammonium ion (NH_4^+) at the B site, and halides at the X site⁵¹.

These all-organic perovskites can also be referred to as metal-free perovskites, as they lack metallic ions in their crystal structure.

On the other hand, all-inorganic perovskites consist of metallic cations occupying the A and B sites. Examples of all-inorganic perovskites include BaTiO_3 ⁵², CsPbI_3 ⁵³, LaYS_3 ⁵⁴, and LaWN_3 ⁵⁵. Schouwink et al. conducted a study where the X site was replaced with the borohydride (BH_4) anionic radical, resulting in a series of stable $\text{AB}(\text{BH}_4)_3$ perovskites with potential for ferroelectric applications⁵⁶. Some examples of such all-inorganic perovskites are $\text{KCa}(\text{BH}_4)_3$, $\text{CsCa}(\text{BH}_4)_3$, and $\text{RbCa}(\text{BH}_4)_3$ ^{56,57}.

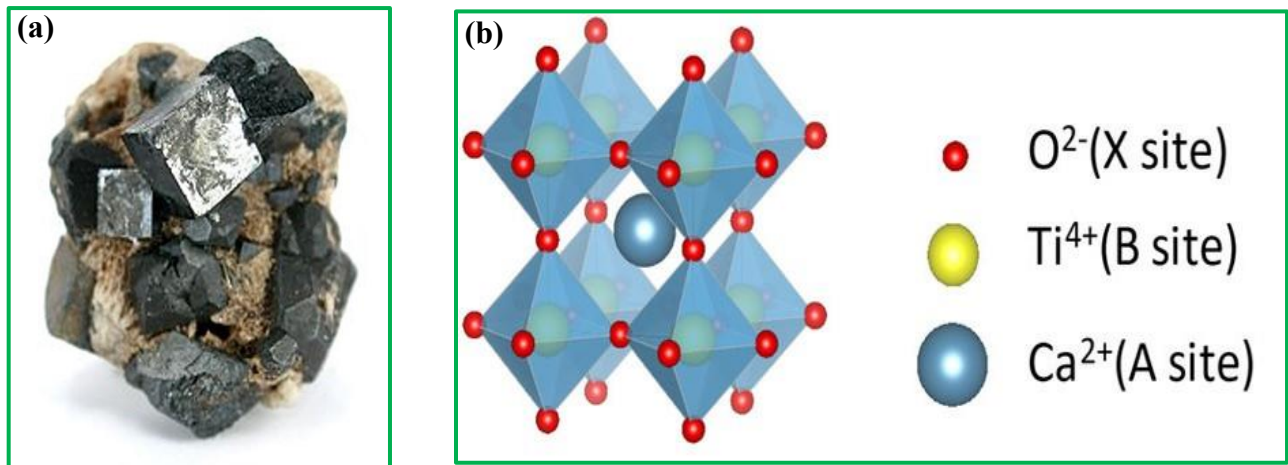


Figure 1: (a) CaTiO_3 rock crystals⁵⁸; (b) Crystal structure of CaTiO_3 perovskite⁵⁰

Table 1: Classifications of perovskite materials according to their X-site.

Class Based on X-site	Properties	Applications	References
Oxides	Exhibits properties such as ferromagnetism, piezoelectricity, magnetism, superconductivity	Commonly used in ceramic capacitors, integrated memory devices, sensors, spin electronic devices, lasers, ferroelectric diodes, photovoltaic cells, and photocatalysis applications	52,59–61
Sulfides	Exhibits semiconducting and optoelectronic properties	Particularly suitable for tandem solar cells, photoelectrodes, photovoltaic applications, and tandem devices for electrochemical water splitting	54,62–64
Telluride	Demonstrates semiconducting and optoelectronic characteristics	Primarily used in tandem solar cells, photodetectors, gamma-ray detectors, and photovoltaic applications	65
Nitrides	Possesses properties like semi-conductivity, electrical conductivity, ferromagnetism,	Widely utilized in photocatalysis for hydrogen generation, capacitors,	55,66

	magnetism, and catalytic activity	integrated memory devices, and photovoltaic applications	
Selenides	Possesses semiconducting and optoelectronic properties	Commonly employed in photovoltaic applications and photodetectors	67
Hydrides	Known for fast-ion conduction, ferroelectric behavior, and permanent nano-porosity	Utilized in various applications such as hydrogen storage, light-emitting diodes, pressure sensors, and thermal neutron detectors	56,57,68
Halides	Exhibits photovoltaic and optoelectronic behavior, ionically conducting nature, catalytic properties, and luminescence	Widely used in solar cells, supercapacitors, light-emitting diodes, phototransistors, photodiodes, photosensors, and membrane materials	69-72

Likewise, there exist organic-inorganic hybrid perovskites where the A site is occupied by organic cations and the B site is occupied by inorganic cations, or vice versa. Examples of perovskites in this category include $\text{CH}_3\text{NH}_3\text{PbX}_3$, $(\text{CH}_3\text{NH}_3)_3\text{Bi}_2\text{X}_9$, and $\text{CH}(\text{NH}_2)_2\text{PbX}_3$, where the X sites are predominantly occupied by halides^{73,74}. Another classification of perovskites is based on the type of anions present at the X site. This leads to the categorization of perovskites as oxide-, nitride-, hydride-, sulfide-, telluride-, selenide-, or halide-based, depending on the specific anions at the X

site. For instance, BaTiO_3 is an oxide-based perovskite, LaYS_3 is a sulfide-based perovskite, and LaWN_3 is a nitride-based perovskite. Furthermore, $\text{CH}_3\text{NH}_3\text{PbX}_3$ is an example of an organic-inorganic metal halide perovskite, sometimes referred to as a hybrid halide or organometallic halide perovskite. In certain cases, the X site may be occupied by a combination of different halides, resulting in mixed halide perovskites, such as $\text{ABl}_x\text{Cl}_{3-x}$, $\text{ABl}_x\text{Br}_{3-x}$, or $\text{ABBr}_x\text{Cl}_{3-x}$, where A and B represent predefined cations. Table 1 provides an overview of the properties and applications of various perovskite materials, categorized based on their anionic (-X) sites.

Additionally, some perovskites incorporate double anions, where combinations such as oxide-halide, halide-nitride, halide-sulfide, or similar compositions occupy the X site, forming double-anion perovskites ⁷⁵. Laboratory-synthesized examples of double-anion perovskites include $\text{SrFeO}_{3-0.05-0.10}\text{F}_{0.05}$ and $\text{SrFe}_{0.9}\text{Ti}_{0.1}\text{O}_{3-0.05-0.10}\text{F}_{0.05}$ ⁷⁶. Furthermore, using density functional theory (DFT) simulations, other examples in a similar category, such as $\text{CH}_3\text{NH}_3\text{BiI}_2\text{Te}$, $\text{CH}_3\text{NH}_3\text{BiI}_2\text{Se}$, and $\text{CH}_3\text{NH}_3\text{BiI}_2\text{S}$, have been predicted.

Double perovskites, represented by the general formula A_2BCX_6 , have been successfully synthesized in laboratory settings. Examples of such double perovskites include $\text{Cs}_2\text{InAgX}_6$, $\text{Rb}_2\text{CuInX}_6$, $\text{Cs}_2\text{AgBiX}_6$, and more ⁷⁷. These double perovskites can be viewed as a combination of ABX_3 and ACX_3 perovskites. Similarly, the A_3BCDX_9 triple perovskite can be understood as a combination of ABX_3 , ACX_3 , and ADX_3 perovskite, while the $\text{A}_4\text{BCDX}_{12}$ quadruple perovskite consists of ABX_3 , ACX_3 , ADX_3 , and AEX_3 perovskite components. Laboratory synthesis has successfully demonstrated the formation of the $\text{Sr}_3\text{CrFeMoO}_9$ triple perovskite for ferroelectric

applications and the $\text{CaCu}_3\text{Ru}_4\text{O}_{12}$ quadruple perovskite for water oxidation applications^{78,79}. Moreover, triple-cation double-halide perovskites like $\text{Cs}_{0.15}\text{FA}_{0.85}\text{Pb}(\text{I}_{0.9}\text{Br}_{0.1})_3$ and $(\text{MAPbBr}_3)_{0.15}(\text{FAPbI}_3)_{0.85}$ have been synthesized and utilized in optoelectronic applications^{80,81}. Patil J et al. have also synthesized quadruple-cation double-halide perovskite materials, as exemplified by $\text{Cs}_{0.05}(\text{MA}_{0.17}\text{FA}_{0.83})_{0.95}\text{Pb}(\text{I}_{0.83}\text{Br}_{0.17})_3$, for solar cell fabrications^{82,83}.

The most popular among all the classes of perovskite materials mentioned above is a class of semiconductors known as metal halide perovskites (MHPs), with the generic formula ABX_3 (where A is a cation, B is a divalent metal ion, and X is a halide), and also known with the potential to provide more affordable and effective photovoltaics and optoelectronics applications than silicon-based technology⁸⁴⁻⁹⁰. Due to their distinct optical and electrical characteristics, metal halide perovskites have gained a great deal of scientific attention during the last ten years. They have so far been used in industries including photovoltaics, light-emitting diodes, and solar energy conversion technology. Particularly, a greater comprehension of the underlying physical characteristics of the materials and workings of devices has been accompanied by rapid improvement in photovoltaic efficiency⁸⁷. Additionally, recent developments in the generation and characterization of single crystals at both the macro- and nanoscales necessitate a rationalization of the various perovskite semiconductor forms outside of the popular polycrystalline thin films. When compared to other conventional semiconductors such as crystalline Si and GaAs, MHPs stand out due to their remarkable crystallinity despite being processed at low temperatures (around 200°C)⁹¹⁻⁹³. This makes it possible to process on a variety of substrates and makes it simple to

produce perovskite materials in a variety of shapes, from nanocrystals to macroscopic single crystals^{84,94,95}.

Extensive research in recent years has focused on synthesizing MHPs with different dimensionalities, exploring the advantages and drawbacks of low- and high-dimensional structures⁹⁶⁻⁹⁹. The dimensionality of these materials significantly influences their use in photodetection. Low-dimensional structures like quantum wells, nanoplatelets, and nanowires offer enhanced stability, quantum confinement effects, and improved charge transport properties. On the other hand, high-dimensional structures such as bulk crystals and thin films face challenges related to stability and processing but hold potential for scalable device fabrication.¹⁰⁰⁻¹⁰⁶ The photodetection capabilities of one-, two-, and three-dimensional perovskites have been extensively investigated with each form of MHP possessing distinct benefits and drawbacks. For instance, 1D perovskites exhibit higher stability and photoluminescence quantum yields, but they have inferior charge transport characteristics compared to 3D perovskites. On the other hand, although 2D perovskites are less effective at light absorption than 1D perovskites, they have superior charge transport properties. 3D perovskites exhibit high absorption coefficients and effective charge transfer, but they are less stable compared to 1D and 2D perovskites¹⁰⁷. Therefore, the choice of perovskite dimension depends on the specific requirements of the photodetection application. For applications demanding great sensitivity and quick response times, 3D perovskites may be appropriate, while 1D perovskites may be suitable for applications requiring high stability and low noise^{108,109}. More details of the applications of MHPs based on dimensionality will follow in subsequent sections. One of the key advantages of perovskite photodetectors is their high

sensitivity, enabled by their high absorption coefficients and efficient charge transport properties. Moreover, the use of low-cost solution-based processes for their fabrication makes perovskite photodetectors an attractive alternative to conventional photodetectors, which often require expensive and complex fabrication methods ¹¹⁰.

Furthermore, the study of MHPs has made remarkable strides in recent years, concentrating mostly on 3D and 2D structures while leaving low-dimensional 1D and 0D structures largely unexplored. The amazing and practical features of 1D and 0D perovskites differ greatly from those of 3D and 2D perovskites due to the strong quantum confinement and site isolation. The excitement surrounding recent advancements stems not only from individual accomplishments but also from what these materials stand for in terms of a brand-new approach to material creation.

2.2 History of Metal Halide Perovskite Studies

In 1958, Moller made the first halide perovskites, CsPbX_3 ($X = \text{Cl, Br, or I}$) ¹¹¹. Later, methylammonium cation (MA) was noted as an A-site cation in organic MHPs in 1978 ¹¹². Mitzi and colleagues studied layered two-dimensional (2D) perovskites in the 1990s that contained layers of metal halide $\langle 100 \rangle$ or $\langle 110 \rangle$ in addition to three-dimensional (3D) structures ^{113,114}.

The implementation of MHPs in thin-film transistors and LEDs and later in photodetectors was made possible by their good carrier mobility and solution processability ^{114,115}. However, due to the inferior device performance compared to those based on organic and inorganic materials, MHPs had not garnered much attention at that time ¹¹⁶. The innovative work of Miyasaka in 2009, which used MAPbBr_3 and MAPbI_3 as light-harvesting components for sensitized PVs, revived

interest in metal halide perovskites ¹¹⁷. Since that time, the PCEs of perovskite-based PVs have improved by an unprecedented amount, going from 4% to more than 22% in just 6 years. Coworkers and Friend (2014) demonstrated the usage of MHPs for room-temperature electroluminescence devices in addition to PV applications ¹¹⁸.

MHPs' complex chemistry allows for a variety of band structure management and color tuning techniques by modifying the composition and dimensionality. For instance, the emission spectra of MHPs might easily be made to cover the whole visible spectral area by adjusting the halide compositions (Figure 3) ¹¹⁹⁻¹²¹. In addition to composition management, dimensionality adjustment at the molecular and morphological levels has been shown to be a successful method for modifying the photophysical characteristics of this class of materials. Pérez-Prieto and colleagues created 6 nm-sized 0D MAPbBr₃ quantum dots in 2014 using long alkyl chains as organic capping ligands ¹²². Tyagi and colleagues revealed that colloidal 2D perovskite nanoplatelets showed quantum confinement effects the next year ¹²³.

Recently, several nano-, meso-, and microstructure MHPs have been produced. By reacting Cs-oleate with a Pb(ii) halide in octadecene, monodisperse colloidal nanocrystals based on fully inorganic cesium lead halide perovskites (CsPbX₃; X = Cl, Br, I or a mixture thereof) have been produced. Figure 2b depicted a hypothetical crystal structure of zero, one-, two-, and three-dimensional CsPbI₃ perovskite as reported by Xiao Z. and his colleagues ¹²⁴. The resulting perovskite nanocrystals exhibit extraordinary spectral tunability over the whole visible spectrum (410-700 nm), narrow emission linewidths (12-42 nm), and high photoluminescence quantum

efficiency (PLQE) up to 90%. Perovskite nanocrystals can be made chemically more easily than metal chalcogenide-based quantum dots, and they don't appear to need complicated core-shell configurations, which are necessary for CdSe quantum dots to exhibit significant PLQE^{84,125–127}. Generally speaking, MHPs have achieved superior performance in solar cells^{128–134}, light-emitting diodes^{135–149}, lasers^{150–156}, and photodetectors^{157–169}.

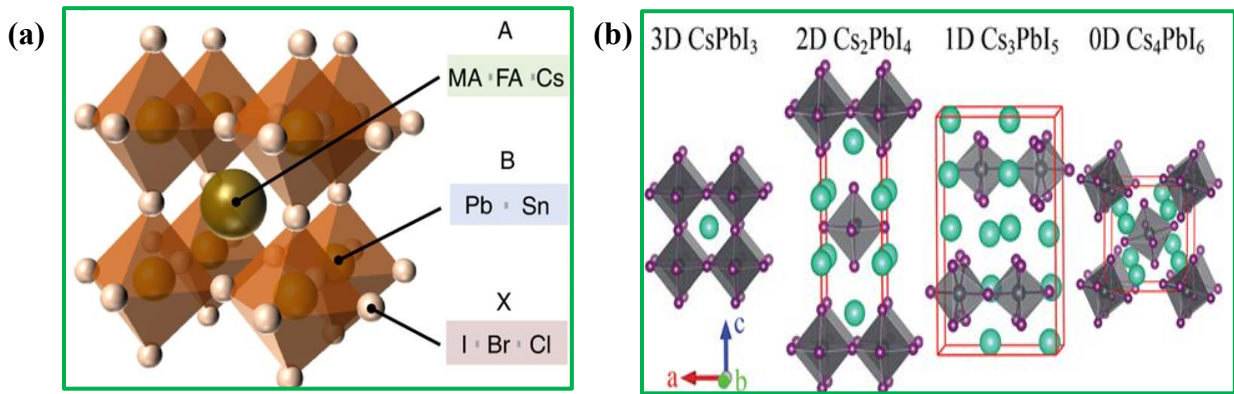


Figure 2: (a) ABX₃ crystal structure of metal halide perovskite, where permutations between ions at A, B and X sites occur¹⁷⁰; (b) Hypothetical model of CsPbI₃, Cs₂PbI₄, Cs₃PbI₅, and Cs₄PbI₆ crystal structures¹²⁴.

2.3 MHPs Composition, Crystal Structure, Properties, and Classifications

2.3.1. Composition of MHPs

The compositions of metal halide perovskites (MHPs) play a fundamental role in determining their properties and performance in various applications. MHPs have a general chemical formula of ABX₃, where A represents a monovalent organic or inorganic cation, B denotes a divalent metal cation, and X represents a halide anion. The choice of A cation is diverse and includes both organic

and inorganic options. Organic cations commonly used in MHPs include methylammonium (MA), formamidinium (FA), and phenethyl-ammonium (PEA). Inorganic cations such as cesium (Cs) are also utilized. The selection of the A cation influences the crystal structure and electronic properties of the MHPs. For example, incorporating MA or FA cations can lead to improved stability and larger bandgaps, while the use of Cs cations can enhance moisture resistance. The B cation in MHPs is typically a transition metal, with lead (Pb) and tin (Sn) being the most widely studied. Lead-based perovskites, such as methylammonium lead iodide (MAPbI₃), have received significant attention due to their excellent optoelectronic properties and photovoltaic performance. Tin-based perovskites, such as methylammonium tin iodide (MASnI₃), have also been explored, although their stability remains a challenge. The X anion in MHPs is typically a halide, including chloride (Cl), bromide (Br), and iodide (I). The choice of halide has a significant impact on the bandgap and optical properties of the MHPs. Different halides can be combined in the synthesis process to achieve mixed-halide perovskites, allowing for bandgap engineering and optimization of light absorption properties. By carefully selecting the A cation, B cation, and X anion, researchers can tailor the composition of MHPs to achieve specific properties and optimize their performance in photodetection applications. The composition of MHPs significantly influences their optical absorption, charge transport, and stability, making it a crucial aspect to consider when developing novel materials and devices.

2.3.2. Crystal structure of MHPs

Halide perovskites' crystal structure is built upon a three-dimensional framework of corner-sharing octahedra (Figures 1,2 and 3) ¹⁷¹. Particularly, the organic cations (such as methylammonium or formamidinium) or monovalent alkali metal cations (such as cesium) are situated between the halide and heavy metal cations (typically lead or tin) occupying the center of a cubic or tetragonal unit cell as in Figure 1. Depending on the precise chemical composition of the material, the arrangement of the metal, halide, and organic cations within the perovskite crystal may vary. The band gap, absorption characteristics, and carrier mobility of the perovskite, for instance, can be tailored by varying the halides or organic cations utilized in the material. Nonetheless, the basic structure of a halide perovskite always involves a repeating pattern of corner-sharing octahedra that are stabilized by the presence of the organic cations. Halide perovskite can be seen in either of the two forms, namely, Metal halide perovskites (MHPs) as in Figure 2, and Not-metal halide perovskites (NMHPs) as in Figure 4 ⁴⁵.

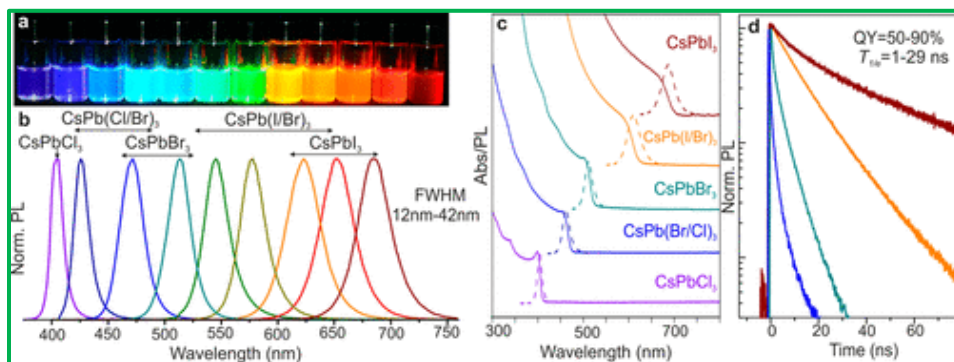


Figure 3: (a) colloidal solutions in toluene under UV lamp ($\lambda = 365$ nm); (b) representative PL spectra ($\lambda_{\text{exc}} = 400$ nm for all but 350 nm for CsPbCl₃ samples); (c) typical optical absorption and PL spectra; (d) time-resolved PL decays for all samples shown in (c) except CsPbCl₃ ¹¹⁹.

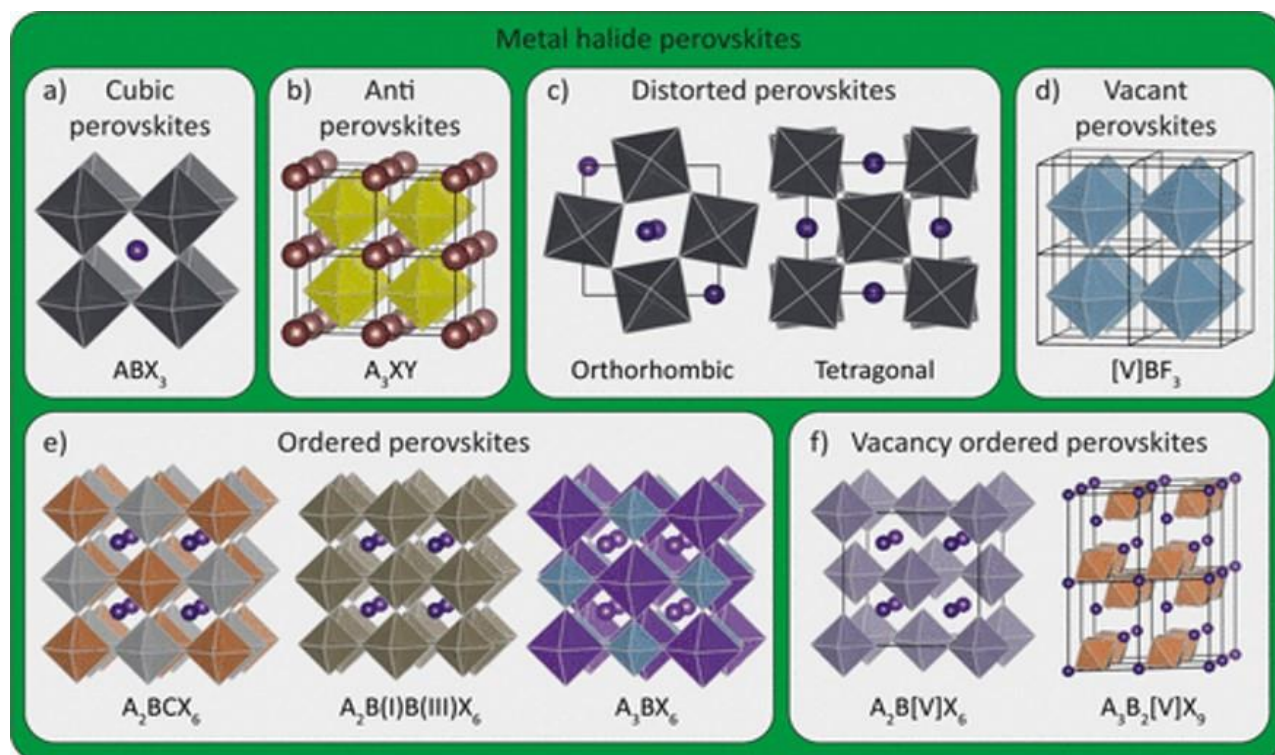


Figure 4: Overview of different halide perovskites. (a) Standard ABX_3 cubic halide perovskites. (b) Antiperovskites, with A being a monovalent metal (like Li^+ or Ag^+), X a halide, and Y a chalcogenide. (c) Common orthorhombic and tetragonal disordered perovskites, arising from the tilting of the octahedra. (d) Vacant BX_3 perovskites, like AlF_3 . (e) Ordered perovskites, where two M(II) metals are replaced by a M(I) and M(III) metal. (f) Vacancy-ordered perovskites, where a part of the B-site cations is replaced with an M(III) or M(IV) and vacancies⁴⁵.

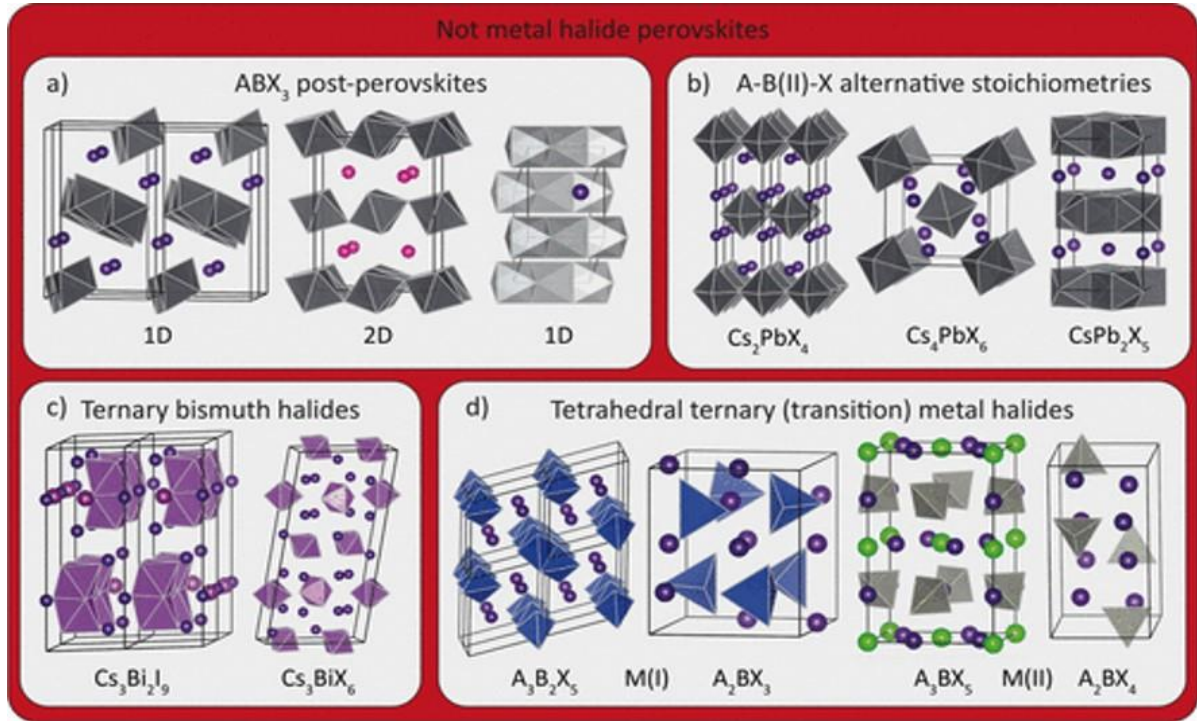


Figure 5: Overview of ternary metal halides not crystallizing in a perovskite structure. (a) Post-perovskites formed by ABX_3 ternary metal halides that would form stable perovskites at higher temperatures/pressures. (b) Ternary M(II) halides with non-perovskite stoichiometries, including inorganic Ruddlesden–Popper metal halide (A_2BX_4), A_4BX_6 , and AB_2X_5 phases. (c) Ternary bismuth halides not crystallizing in vacancy-ordered perovskites, including the isolated dimer structure ($Cs_3Bi_2I_9$) and isolated octahedra (Cs_3BiX_6). (d) Several ternary M(I) and M(II) (mainly transition metal and F^- and Cl^-) phases are based on MX_4 tetrahedra⁴⁵.

The radii of the A, B, and X ions are restricted within a particular range in order to maintain a stable MPH structure. Such a limitation is quantified by the Goldschmidt tolerance factor defined

as:

$$t = \frac{r_A + r_X}{\sqrt{2}(r_B + r_X)} \quad (2.1)$$

where, respectively, r_A , r_B , and r_X stand for A cations, B cations, and X anions^{172,173}. Empirically, a stable perovskite structure needs a t value of 0.8 to 1.0¹⁷⁴. This enables the selection of methylammonium (CH_3NH_3^+ , MA), formamidinium ($\text{CH}(\text{NH}_2)_2^+$, FA), Cs^+ , or Rb^+ as A cations, Pb^{2+} , Sn^{2+} , Ge^{2+} , or Sr^{2+} as B cations, and Cl^- , Br^- , and I^- as X anions in metal halide perovskites.

Table 2.1 lists these appropriate ions for metal halide perovskites together with their ionic radii

132,175.

Table 2: Ionic radii of typical metal halide perovskite ions.

A⁺ cation	Ionic radii (pm)	B²⁺ cation	Ionic radii (pm)	X⁻ anion	Ionic radii (pm)
MA	217	Pb	199	Cl	181
FA	253	Sn	118	Br	196
Cs	181	Ge	87	I	220
Rb	166	Sr	118		

The tolerance factor, defined in equation 1, evaluates whether the A-site ion can stabilize the corner-sharing octahedral framework $[BX_3]$, also known as the ReO_3 structure. Typically, perovskites are formed when t values fall within the range of $0.8 \leq t \leq 1$. However, towards the lower end of this range, distortions may occur due to tilting of the $[BX_6]$ octahedra and a reduction in symmetry. When $t > 1$, the A-site ion is too large to create a three-dimensional (3D) perovskite (though lower-dimensional structures may still be possible). Conversely, when $t < 0.8$, the A-site ion is too small, resulting in structures that deviate from the perovskite arrangement. The parameter μ , defined as the ratio of r_B to r_X , called Pauling's first rule¹⁷⁶, evaluates whether the B-site ion can fit into the octahedral voids within the X-site anion sublattice. The radius of an octahedral void, r_{hole} , formed within six closely packed rigid spheres of radius r_X , is given by $r_{\text{hole}} = 0.414r_X$. according to this rule, B-site cations with μ smaller than 0.414 will not touch the six X-site anions, resulting in instability and a lower coordination number. Slightly greater than 0.414, the octahedral geometry becomes more stable as the B-site cation is still in contact with the six X-site anions, though the X-site anions are now farther from each other, reducing their mutual repulsion. However, as μ increases and reaches 0.592, a 7-coordinated capped octahedron becomes more favorable. Therefore, to stabilize the $[BX_6]$ octahedra, it is necessary to have a range of $0.414 \leq \mu < 0.592$. Travis et al. utilized revised ionic radii to create a t - μ plot for iodide compounds of the ABX_3 type, as depicted in Figure 4a-b¹⁷⁷. The lower horizontal boundary line remains constant, representing the octahedral factor critical for perovskite formation when μ exceeds 0.414. The vertical boundary line is set at $t = 0.875$; compounds falling to its left, such as ABi_3 , do not adopt the perovskite structure. The boundary defining the stable perovskite region on the high tolerance

factor side (right-hand side of Figure 6b) is less distinct. Achieving a high t value approaching 1 necessitates an exceedingly large A-site cation relative to the B-site and X-site ions. Cesium (Cs) is among the largest group-I elements on the periodic table. Nevertheless, it is still insufficiently large to stabilize the cubic iodide perovskite structure. Thus, it must be substituted with a slightly larger monovalent molecule to achieve structural stability. This explains why materials like MAPbI₃ and FAPbI₃ exhibit greater stability than CsPbI₃. While the t - μ plot has been employed by numerous research teams to evaluate the stability of metal halide perovskites, a more comprehensive assessment of stability should be conducted using advanced theoretical techniques like density-functional theory (DFT).

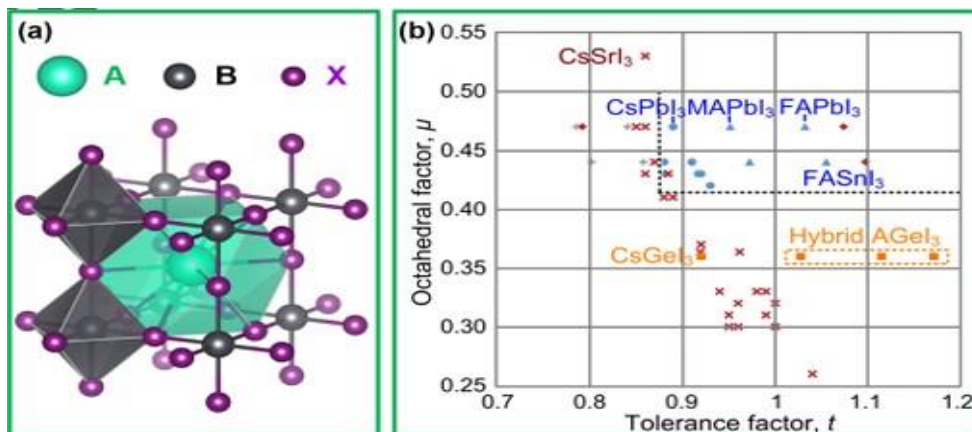


Figure 6: Perovskite ABX₃ cubic structure. b) Structural map of ABX₃ compounds. Blue dots and red crosses represent stable inorganic perovskites and non-perovskites.

2.3.3. Properties of MHPs

The properties of perovskite materials are predominantly influenced by the interactions between A and X as well as B and X as shown in Table 1^{47,77}. These interactions can take the form of bond

lengths, bond angles, or a combination of atomic orbital mixing. For example, the band gap of perovskites is determined by the electronic occupancy of the p-orbitals of the B cation and the s- or d-orbitals of the X anion¹⁷⁸. Almost all optical properties of perovskites revolve around the band gap of the material. The strength of bonds between A–X and B–X has been utilized to predict the preferred growth direction, dimensional characteristics, and size of perovskite crystals¹⁷⁹. These factors also influence the electrical and optical properties of perovskite materials. Hence, the anions at the X sites play a significant role in determining the properties of perovskite materials. Optical and electrical properties are fundamental characteristics that underpin the remarkable performance of metal halide perovskites in a wide range of optoelectronic devices. Here, we delve into these properties and highlight key research findings, citing relevant references along the way.

- ***Steady-State and Transient Optical Properties:*** Researchers extensively study the steady-state and transient optical properties of perovskites using techniques like absorption spectroscopy, photoluminescence spectroscopy, and time-resolved photoluminescence (TRPL)¹⁸⁰. These studies provide insights into the materials' behavior under different excitation conditions and help optimize device performance.
- ***Photoluminescence (PL) Spectra:*** Typical semiconductors' PL spectra will closely follow the relationship¹⁸¹:

$$Y_{PL}(E) = \alpha(E)\phi_{bb}(E).e^{\left[\frac{\Delta E_f}{k_B T}\right]} \quad (2.2)$$

which connects a semiconductor's absorptance $\alpha(E)$ (or absorptivity) to its luminescence spectrum ($Y_{PL}(E)$). According to Equation (1.2), an extension of Kirchhoff's equation for thermal emission, a body's emissivity and absorptance are the same. Würfel P.¹⁸¹ generalized this equation to luminescence, or non-thermal emission in semiconductors. The fundamental premise underlying this generalization is that the emission results from the recombination of free electrons and holes, whose occupation probability can be expressed by Fermi-Dirac statistics. The quasi-Fermi level splitting has a spatially independent value in equation (1.2). Although this criterion of a spatially independent quasi-Fermi level splitting is never quite accurate, it is a decent approximation for thin films of lead-halide perovskites but not for mm-thick crystals. The PL spectrum of a semiconductor is determined by the absorption edge on the low energy side and by the Boltzmann tail of the Bose-Einstein distribution that is a part of Φ_{bb} on the high energy side because the absorptance of a semiconductor,

$$\alpha(E) = (1-R) (1 - \exp(-\alpha d)) \quad (2.3)$$

increases steeply around the band gap for typical direct gap absorption coefficients, α , and then approaches a constant value¹⁸². Figure 15 displays the photoluminescence spectrum and associated absorption coefficient of a MAPbI₃ film on glass that was measured using photothermal deflection spectroscopy (PDS) on the high energy side and superimposed with the absorption coefficient obtained from Equation 2 on the low energy side.

- ***Strong Nonlinear Optical Response:*** Perovskites display a strong nonlinear optical response, making them suitable for applications in nonlinear optics and optical signal processing. This property has implications for the development of efficient frequency converters and modulators ^{183,184}. The term "Strong Nonlinear Optical Response" within the realm of MPHs signifies the remarkable capacity of these materials to undergo substantial alterations in their optical characteristics when exposed to high-intensity light or intense optical fields. Unlike linear optical materials like traditional semiconductors, metal halide perovskites exhibit a nonlinear optical response characterized by phenomena that deviate from the linear relationship between incident light and the material's reaction ¹⁸⁵. In the domain of MPHs, this robust nonlinear optical response takes on several distinct forms:
 - a. ***Optical Nonlinearity:*** When subjected to intense light, MPHs display nonlinear alterations in their refractive index, absorption coefficient, or other optical properties. This nonlinear behavior holds immense potential for applications in nonlinear optics, encompassing processes such as frequency doubling, optical switching, and parametric amplification ¹⁸⁶.
 - b. ***Second-Harmonic Generation (SHG):*** Certain MPHs exhibit a remarkable capacity for SHG, a nonlinear optical process wherein two incident photons of identical frequency combine within the material to produce a new photon with double the frequency. This property positions MPHs as suitable candidates for generating coherent light at shorter wavelengths, holding promise for a range of optical applications ¹⁸⁷.
 - c. ***Four-Wave Mixing (FWM):*** MPHs with robust nonlinear responses can partake in FWM, another nonlinear optical phenomenon that involves the interaction of four optical waves

within the material. This capability opens doors to applications like wavelength conversion and signal processing, wherein MHPs can be effectively employed ^{188,189}.

- d. ***Kerr Effect:*** In some instances, MHPs exhibit the Kerr effect, signifying a change in the material's refractive index when subjected to an applied electric field. This property facilitates the manipulation of light in electro-optic devices, presenting opportunities for innovative optical technologies ^{190,191}.
- e. ***Optical Limiting:*** MPHs endowed with a robust nonlinear optical response find utility in optical limiting applications. Optical limiters are instrumental in safeguarding optical sensors and detectors by attenuating intense light, ensuring that only safe levels of light reach these sensitive components ¹⁹².

The profound nonlinear optical response observed in MHPs can be attributed to their distinctive electronic and structural properties. Their remarkable interactions between light and matter, coupled with high carrier mobilities and extended carrier lifetimes, underlie their nonlinear optical behavior ¹⁹³. Researchers are actively engaged in exploring these nonlinear optical properties for a multitude of applications spanning the fields of photonics, telecommunications, and optical signal processing. By harnessing the potent nonlinear optical response exhibited by metal halide perovskites, new horizons are being unveiled for the development of compact and efficient photonic devices ¹⁹⁴.

2.3.4 Classification of MHPs

MHPs can be classified in various ways depending on their properties and characteristics of interest. Here are a few possible classifications, along with references to further reading:

- **By composition:** MHPs can be classified based on the specific combination of metal, halide, and organic/inorganic cations used in their synthesis. For example, some common metal halide perovskites include methylammonium lead iodide (MAPbI₃), formamidinium lead iodide (FAPbI₃), and cesium lead bromide (CsPbBr₃). This classification is often used in the context of materials synthesis and characterization ¹⁹⁵.
- **By dimensionality:** MPHs can also be classified based on their dimensional structure. For example, 3D metal halide perovskites have a bulk crystal structure that is three-dimensional, while 2D metal halide perovskites have a layered structure that is only two-dimensional. Similarly, 1D metal halide perovskites have a linear structure, while 0D metal halide perovskites are nanoparticles or quantum dots ¹⁹⁶. This classification is often used in the context of materials physics and optoelectronics. Details will follow in subsequent sections.
- **By crystal symmetry:** MPHs can also be classified based on their crystal symmetry. The most common crystal systems for metal halide perovskites are cubic, tetragonal, and orthorhombic, but some materials may also exhibit other crystal symmetries. This classification is often used in the context of crystallography and materials science ¹⁹⁷.
- **By stability:** MPHs can also be classified based on their stability, which is a critical property for their use in practical applications. Some researchers have focused on developing stable metal halide perovskites that can resist degradation over time, while others have studied the

causes of instability and the factors that can lead to degradation. This classification is often used in the context of materials engineering and device fabrication^{198,199}.

These are just a few examples of the many possible ways to classify MPHs. The references provided should serve as a starting point for further reading and exploration.

2.3.5 Discrepancies in Naming Halide Perovskites, HPs

Even though there are many distinct kinds of HPs, recent and fast breakthroughs in the field have confused the proper manner to name all the reported diverse compounds. The nomenclature and naming of HPs material have indeed posed challenges and led to discrepancies in the scientific community. These discrepancies arise from the complex structural variations and compositional diversity within the broad category of halide perovskites. Below, we will discuss some of the key reasons behind these discrepancies and provide references to support these points.

- **Structural Variations:** HPs structures can exhibit various degrees of distortion and complexity, which can make naming conventions less straightforward. For instance, some perovskite materials may have octahedral tilts or structural phases that deviate from the ideal cubic or tetragonal perovskite structure^{200,201}. These structural variations can lead to different naming schemes. Akkerman Q. et al⁴⁵ opinioned that, if a compound is to be considered a "perovskite", it must have an ABX_3 (or equivalent) stoichiometry consisting of a cubic network of corner-sharing BX octahedra, with the following exceptions:(i) the A and B sites can be partially or fully vacant or ordered; (ii) the A cations can consist of small organic molecules or inorganic clusters; (iii) the formation of anti-halide perovskites, with a halide occupying either

the A or B site. They contend that 1D and 0D hybrid organic-inorganic metal halides do not meet these criteria and are not, therefore, perovskites. Even though this is a somewhat contentious topic, they have maintained that 2D hybrid organic-inorganic metal halides and layered Ruddlesden–Popper phases do not meet these requirements either. Therefore, in their opinion, they shouldn't be called perovskites. They emphasized the significance of specifying whether a perovskite is vacant, ordered, anti, or a combination of these in their conclusion as depicted in Figures 4 and 5 ⁴⁵.

- ***Compositional Diversity:*** HPs can have different cations and halide anions, and the specific combination of these elements affects their properties and crystal structures. For example, methylammonium lead iodide (MAPbI₃) and formamidinium lead bromide (FAPbBr₃) are popular halide perovskite compositions²⁰². The use of different cations and halides has led to variations in naming.
- ***Synthetic Modifications:*** Researchers often tailor halide perovskite materials through synthetic modifications to improve their properties or stability. These modifications can result in materials with distinct characteristics that may warrant a separate naming convention.
- ***Historical Naming:*** Some discrepancies in naming may be due to historical reasons, where different research groups adopted their own naming conventions before standardized nomenclature was established. This can lead to confusion when comparing studies conducted by different groups.

- ***International Collaboration:*** The global nature of scientific research means that researchers from different countries may use different naming conventions based on their traditions and language. This can further contribute to discrepancies in naming.
- ***Evolution of Standards:*** The field of halide perovskite research is dynamic, and standards and conventions evolve over time as new insights emerge. This evolution can lead to inconsistencies in naming.

Efforts are underway to standardize the naming of halide perovskites to reduce discrepancies. For example, the International Union of Crystallography (IUCr) has established guidelines for naming perovskite-related structures²⁰³. Additionally, organizations like the National Institute of Standards and Technology (NIST) have published guidelines for reporting perovskite compositions in scientific literature.

2.4. Photodetector Physics

A photodetector is a device that is used to detect and measure light. It converts light signals into electrical signals, enabling the measurement of light intensity or the detection of light in various applications^{204–206}. Photodetectors are crucial components in various technologies, including optical communication, imaging systems, and sensors^{206–208}.

The fundamental concept underlying photon detection involves the generation of electron-hole pairs when light with an appropriate wavelength or energy interacts with semiconductors. These semiconductors can be either intrinsic or extrinsic.

Intrinsic semiconductors exist in their pure state, where the number of electrons equals the number of holes. Examples of intrinsic semiconductors include silicon, germanium, and arsenic, each possessing four electrons in their valence shells, enabling them to create four holes during electron transitions. In addition to traditional semiconductor elements, certain materials like perovskites (e.g., CaTiO_3 , MAPbI_3) and Gallium Arsenide also exhibit intrinsic semiconductor behavior.

Extrinsic semiconductors, on the other hand, are intrinsic semiconductors that have been doped with pentavalent or trivalent elements. Pentavalent elements, with five electrons in their valence shell, can still supply one free electron when bonded with intrinsic semiconductors like silicon. Trivalent elements, with three electrons in their valence shell, create a hole in the process as they become short of one electron, which they obtain from surrounding atoms. Extrinsic semiconductors can either supply holes or electrons, with N-type extrinsic semiconductors providing electrons and P-type extrinsic semiconductors supplying holes.

Materials such as TiO_2 , ZnO_2 , MOS_2 , and PCBM exhibit behavior akin to N-type extrinsic semiconductors, while NiO , Ni_2O_3 , CuO_x , CoO_x , and PEDOT: PSS behave as P-type extrinsic semiconductors. Understanding the distinctions between intrinsic and extrinsic semiconductors, as well as their specific behavior, is essential for comprehending the principles behind photon detection. Understanding the working principle of photodetectors (Figure 7)²⁰⁹ is essential for optimizing their performance in different applications and for designing devices that rely on their light-detection capabilities. For metal halide perovskite (such MAPbI_3) based photodetector with P-type/intrinsic/N-type (PIN) structure, here's an explanation of the working principle:

- ***Incident Light Absorption:*** When photons from incident light strike the intrinsic layer, they are absorbed by the MAPbI₃ perovskite material. This absorption generates electron-hole pairs within the perovskite crystal lattice.
- ***Generation of Electron-Hole Pairs:*** The absorbed photons promote electrons from the valence band to the conduction band, leaving behind positively charged holes in the valence band. This process creates free electrons and holes, resulting in an increased concentration of charge carriers.
- ***Charge Carrier Transport:*** The PIN structure is crucial for efficient charge carrier transport. The structure includes a P-type layer (hole transport layer, such as Ni₂O₃), an intrinsic layer (light-absorbing like MAPbI₃), and an N-type layer (electron transport layers, such as c-TiO₂, and m-TiO₂).
- ***Hole Transport (P-type):*** The holes (positive charge carriers) generated in the MAPbI₃ layer move towards the P-type layer (Ni₂O₃) due to the internal electric field within the device.
- ***Electron Transport (N-type):*** Simultaneously, the electrons (negative charge carriers) move towards the N-type layers (c-TiO₂ and m-TiO₂) due to the electric field.
- ***Charge Separation and Collection:*** The intrinsic layer (MAPbI₃) serves as the region where charge carriers are initially generated. Due to the PIN structure and the internal electric field, electrons and holes are efficiently separated and directed toward their respective transport layers. The efficient separation and transport of charge carriers ensure that they reach their respective electrodes, contributing to the generation of a measurable electrical signal.

- **Photocurrent Generation:** As *electrons* and holes reach the electrodes (FTO), they contribute to the overall photocurrent of the device. The flow of this photocurrent is a measurable response to the incident light, allowing the photodetector to detect and quantify light intensity.

In normal operation, a reverse bias voltage is applied across the device so that no free electrons or holes exist in the intrinsic region.

In summary, the PIN structure in a MAPbI₃ photodetector enhances the efficiency of charge carrier transport and separation, leading to improved performance in detecting incident light. This design is essential for achieving high sensitivity and responsiveness in perovskite photodetectors.

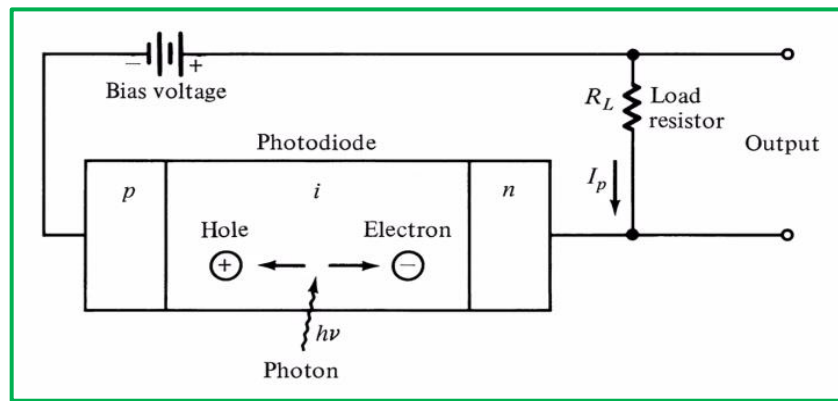


Figure 7: Schematic representation of the Working principle of a PIN photodetector (photodiode) with an applied reverse bias^{206,209}.

2.5 Classification of Photodetectors

There are different types of photodetectors, each designed for specific purposes. Common types include photodiodes, phototransistors, and photonic detectors. Photodiodes, for example, operate based on the principle of the photoelectric effect, where incident photons generate electron-hole

pairs in a semiconductor material, resulting in a measurable current. In physics and technology, understanding the principles behind photodetectors can be valuable, especially in the context of renewable energy technologies, imaging devices, and other applications where the detection and measurement of light play a crucial role. Photodetectors can be categorized into several classes based on their operating principles, materials, and applications. Here are some common classes of photodetectors:

2.5.1 Photodiodes

- ***p-n Junction Photodiodes:*** These are the most common types of photodiodes, operating based on the photoelectric effect. They are widely used in various applications, including optical communication and light detection.
- ***Avalanche Photodiodes (APD):*** APDs utilize the avalanche multiplication effect, where carriers gain energy through impact ionization, resulting in an increased photocurrent. This leads to higher sensitivity but requires higher bias voltages.
- ***PIN Photodiodes:*** These photodiodes have a p-type layer, an intrinsic (undoped) layer, and an n-type layer. The intrinsic layer allows for a larger depletion region and enhanced sensitivity.

2.5.2 Phototransistors

Phototransistors are similar to regular transistors but are designed to respond to light. They have a three-layer structure (collector, base, emitter), and the base current is modulated by incident light, affecting the overall transistor behavior.

2.5.3 Photonic Detectors

- ***Photomultiplier Tubes (PMT)***: PMTs are vacuum tubes with multiple dynodes that amplify the photoelectrons generated by incident photons. They are sensitive to low light levels and are widely used in applications like spectroscopy.
- ***Single-Photon Avalanche Diodes (SPAD)***: SPADs are designed to detect individual photons. They operate in the avalanche mode and are commonly used in applications such as quantum optics and quantum communication.

2.5.4 Infrared Detectors

- ***Thermopiles***: These detectors measure the temperature change caused by the absorption of infrared radiation. They are commonly used in non-contact temperature measurements.
- ***Infrared Photodiodes and Phototransistors***: Specifically designed to detect infrared light, these detectors are used in applications such as night vision and proximity sensors.

2.5.5 Photoconductors

Photoconductors exhibit changes in electrical conductivity when exposed to light. Common materials include amorphous selenium and cadmium sulfide. They find applications in photocopiers and some imaging devices.

These categories provide a broad overview, and within each class, there can be variations and specialized types based on specific requirements. The choice of a photodetector depends on factors such as sensitivity, speed, wavelength range, and intended application.

2.6 Photodetector Performance Metrics

Photodetectors are evaluated through several performance metrics, also known as figures of merit. These metrics provide insights into their efficiency and effectiveness in converting light signals into electrical currents. Let's delve into each metric:

2.6.1 Quantum efficiency

Quantum efficiency (QE) is a fundamental metric used to assess the performance of photodetectors, particularly in terms of their ability to convert incident photons into electrical carriers, such as electrons or holes. It quantifies the effectiveness of a photodetector in generating charge carriers in response to incident light. Understanding quantum efficiency is crucial for optimizing the sensitivity and overall performance of photodetectors in various applications, including imaging, spectroscopy, and communication systems. Quantum efficiency is mathematically expressed as the ratio of the number of generated carriers ($N_{carriers}$) to the number of incident photons ($N_{photons}$) as depicted in equation (2.4).

$$QE = \frac{N_{carriers}}{N_{photons}} \quad (1.4)$$

QE has several significances including:

- **Sensitivity:** A higher quantum efficiency indicates that more incident photons are effectively converted into electrical signals, leading to increased sensitivity in detecting light.

- **Signal-to-Noise Ratio (SNR):** Quantum efficiency directly influences the signal-to-noise ratio of the photodetector, as it determines the strength of the signal relative to the inherent noise of the device.
- **Energy Efficiency:** Photodetectors with higher quantum efficiency require lower optical power levels to achieve the same signal strength, thus conserving energy in optical systems.
- **Dynamic Range:** Quantum efficiency impacts the dynamic range of the photodetector, defining its ability to accurately detect both weak and strong optical signals across a wide range of intensities.

There also several factors influencing quantum efficiency including:

- **Material Properties:** Quantum efficiency depends significantly on the material properties of the photodetector, including its bandgap energy, absorption coefficient, and carrier mobility.
- **Wavelength Range:** The quantum efficiency of a photodetector varies with the wavelength of incident light, influenced by the material's absorption characteristics and band structure.
- **Surface and Interface Effects:** Surface and interface states within the photodetector structure can impact quantum efficiency by affecting carrier recombination and extraction processes.
- **Device Design:** The design parameters of the photodetector, such as layer thicknesses, doping profiles, and surface passivation techniques, can be optimized to enhance quantum efficiency.

➤ **Operating Conditions:** Quantum efficiency may change under different operating conditions, such as temperature, bias voltage, and illumination intensity.

In photodetectors, not all generated electrons are necessarily collected at the output, even though they contribute to the overall quantum efficiency. The collection efficiency depends on various factors, including the material properties, device structure, and operational conditions. Quantum efficiency (QE) can be categorized into two main types. Let's explore this aspect in the context of External Quantum Efficiency (EQE) and Internal Quantum Efficiency (IQE). These metrics provide insights into different aspects of a photodetector's performance and efficiency in converting incident photons into electrical signals.

a. External Quantum Efficiency

External quantum efficiency (EQE) refers to the efficiency of a photodetector in converting incident photons into electrical carriers and subsequently detecting them. EQE quantifies the fraction of incident photons that are converted into useful electrical signals at the output of the photodetector. It encompasses all factors influencing the overall performance of the photodetector in practical applications, including optical losses, surface recombination, and collection efficiency. External quantum efficiency (EQE) is expressed as the ratio of the number of collected charge carriers ($N_{collected}$) to the number of incident photons ($N_{incident}$) as given in equation (2.5).

$$EQE = \frac{N_{collected}}{N_{incident}} \quad (2.5)$$

EQE considers all electrons generated throughout the photodetector, both in the active and non-active regions, due to incident photon absorption. While EQE evaluates the overall collection

efficiency of the photodetector, it does not guarantee that all generated electrons will be collected at the output. Factors such as carrier mobility, recombination losses, trapping effects, and extraction efficiency can lead to a lower collection efficiency than the total number of generated electrons. Figure 8 compared the EQE of b-Si photodiode with that of violet- and infrared-optimized photodiodes²¹⁰

The External Quantum Efficiency (EQE) can be related to Responsivity (R) and wavelength (λ) using the following mathematical relationship in equation (2.6).

$$EQE = R(\lambda) \frac{hc}{e\lambda} \quad (2.6)$$

Where: $R(\lambda)$ is the Responsivity at wavelength λ , h is the Planck's constant (6.626×10^{-34} J·s), c is the speed of electromagnetic radiation in vacuum (3×10^8 m/s), e is the elementary charge (1.602×10^{-19} C).

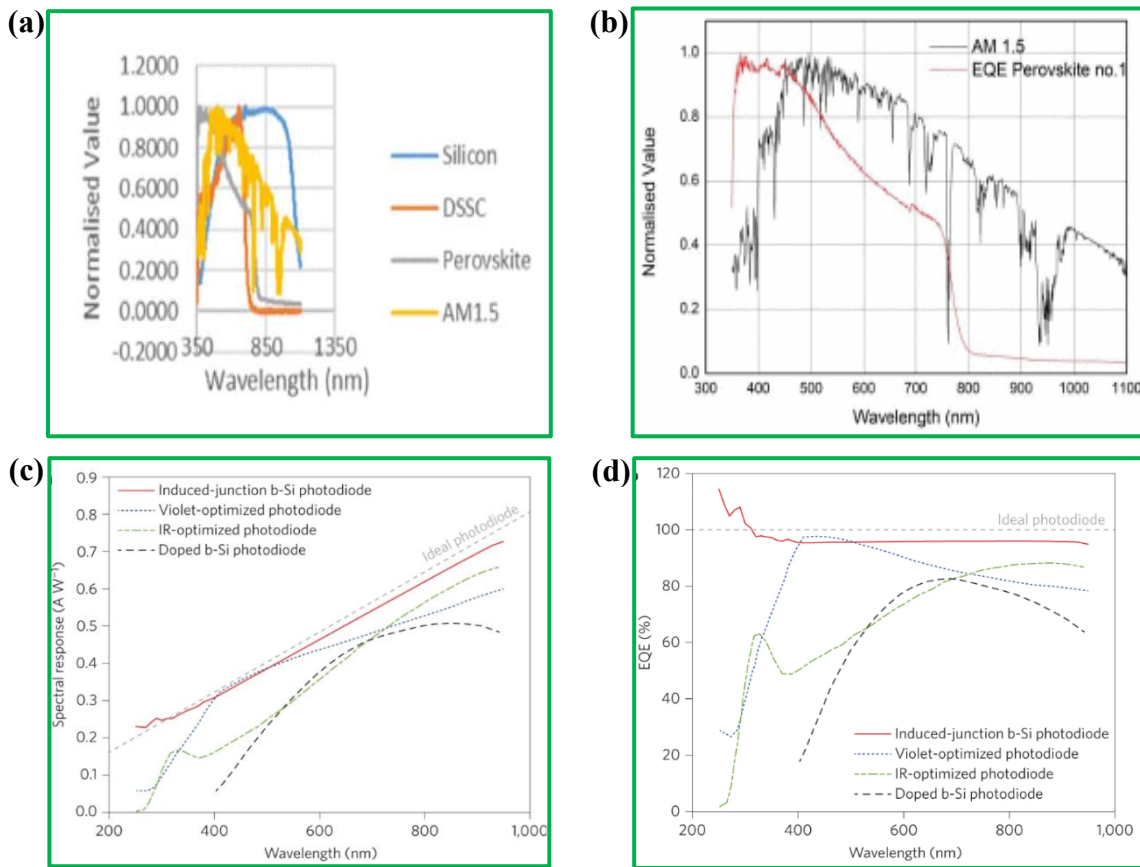


Figure 8: (a) Comparison of EQE of three types of solar cells; (b) EQE of perovskite solar cell and AM1.51 (c) spectral response for the b-Si photodiode compared with violet- and infrared-optimized photodiodes from the Hamamatsu commercial manufacturer; (d) EQE of b-Si photodiode compared with violet- and infrared-optimized photodiodes²¹⁰.

b. Internal Quantum Efficiency

Internal quantum efficiency (IQE) focuses on the efficiency of carrier generation and collection processes within the active region of the photodetector. It specifically evaluates the fraction of absorbed photons that contribute to the generation of useful electrical signals before any losses

occur due to factors such as surface recombination or optical absorption within non-active regions of the device.

Internal quantum efficiency (IQE) is expressed as the ratio of the number of generated carriers ($N_{generated}$) to the number of absorbed photons ($N_{absorbed}$) as given by equation (2.7).

$$IQE = \frac{N_{generated}}{N_{absorbed}} \quad (2.7)$$

IQE focuses on the efficiency of electron generation specifically within the active region of the photodetector, where photon absorption leads to the creation of electron-hole pairs.

Similar to EQE, IQE does not ensure that all generated electrons within the active region will be collected. It evaluates the intrinsic efficiency of the carrier generation and collection processes, considering factors such as carrier recombination, trapping, and extraction efficiency within the active material.

The key differences between EQE and IQE are:

- **Scope:** EQE considers all factors affecting the overall performance of the photodetector, including optical losses and surface recombination, whereas IQE focuses solely on the efficiency of carrier generation and collection processes within the active region.
- **Measurement:** EQE is typically measured experimentally by comparing the output electrical signal to the incident optical power, while IQE requires additional characterization techniques to isolate the contributions of carrier generation and absorption processes.

- ***Design Optimization:*** EQE guides the optimization of photodetector designs for practical applications by considering factors beyond the active region, while IQE provides insights into the intrinsic efficiency of the device and aids in the design of more efficient photodetection structures. The actual collection efficiency of a photodetector is typically less than 100%, even though the quantum efficiency (EQE or IQE) may be high (as depicted in Figure 6d). This discrepancy arises due to various factors affecting electron generation, trapping, recombination, and extraction within the device. Both EQE and IQE are crucial for evaluating and optimizing the performance of photodetectors in various applications, such as imaging, sensing, and communication systems. By understanding and characterizing both external and internal quantum efficiency, researchers and engineers can develop photodetection devices with enhanced sensitivity, efficiency, and functionality.

Quantum efficiency is typically measured experimentally using calibrated (monochromatic) light sources and specialized test setups. Various techniques, such as photoconductivity measurements, photoluminescence spectroscopy, and external quantum efficiency measurements, are employed to quantify quantum efficiency across different spectral ranges and operating conditions. By understanding the factors influencing quantum efficiency and employing appropriate measurement techniques, researchers and engineers can optimize photodetector designs for specific applications, leading to enhanced performance and functionality in optical systems.

2.6.2 Responsivity

Responsivity (R) is a pivotal parameter in the characterization of photodetectors, serving as a metric for evaluating the efficiency with which incident photons are converted into electrical

signals. Mathematically defined as the ratio of the output current or voltage generated by a photodetector to the incident optical power, responsivity (R) is expressed as in equation (2.8).

$$R = \frac{I_{ph} - I_{dark}}{P_{optical}} \quad (2.8)$$

This parameter quantifies the sensitivity of photodetectors across various spectral ranges and is inherently influenced by the semiconductor material employed, device design, and operating conditions. Silicon-based photodetectors typically exhibit responsivity values ranging from 0.1 A/W to 1 A/W in the visible and near-infrared spectral ranges, whereas gallium arsenide (GaAs) and indium gallium arsenide (InGaAs) photodetectors can achieve higher responsivity values exceeding 1 A/W, particularly in the near-infrared spectral range.

The selection of semiconductor material significantly impacts the responsivity of photodetectors due to variations in material properties, bandgap energy, carrier mobility, and optical absorption characteristics. For instance, perovskite materials have garnered considerable attention in recent years due to their remarkable optoelectronic properties, including high absorption coefficients, tunable bandgaps, and low defect densities. Perovskite solar cells have demonstrated EQE efficiencies exceeding 70-80% across a broad spectral range (Figure 8a), aligning with their high responsivity values and making them highly suitable for tandem solar cell configurations and low-light photodetection applications. EQE defined above can also be related to Responsivity (R) and wavelength (λ) using the mathematical relationship in equation (2.9).

Where: $R(\lambda)$ is the Responsivity at wavelength λ , h is the Planck's constant (6.626×10^{-34} J·s), c is the speed of electromagnetic radiation in vacuum (3×10^8 m/s), e is the elementary charge (1.602×10^{-19} C).

Responsivity values are often reported in Amperes per Watt (A/W) or Volts per Watt (V/W) and provide insights into the photodetector's performance and suitability for specific applications. The responsivity of a photodetector is typically optimized for particular spectral ranges based on material properties and application requirements. For example, InGaAs photodetectors offer high responsivity values ranging from 0.5 A/W to 2 A/W in the near-infrared spectral range, making them ideal for telecommunications and spectroscopy applications. Similarly, HgCdTe

$$EQE = R(\lambda) \frac{hc}{e\lambda} \quad (2.9)$$

photodetectors exhibit high responsivity values exceeding 1 A/W in the mid-infrared and thermal imaging spectral ranges, positioning them as preferred choices for infrared sensing and imaging applications.

The responsivity of a photodetector can be further enhanced through device design optimization, including the implementation of anti-reflection coatings, surface passivation techniques, and engineering of the active region of the photodetector. These strategies aim to minimize optical losses, improve carrier extraction efficiency, and enhance the overall performance and efficiency of photodetectors across specific spectral ranges. Moreover, careful characterization and calibration of photodetectors are essential to account for variations in responsivity under different

operating conditions such as temperature, bias voltage, and illumination intensity, ensuring accurate performance assessment and reliable operation in practical applications.

In summary, responsivity serves as a critical parameter for evaluating the sensitivity and performance of photodetectors across different spectral ranges and applications. The reported values of responsivity for various semiconductor materials, including silicon, gallium arsenide, indium gallium arsenide, perovskites, and HgCdTe, offer valuable insights into the capabilities and potential of different photodetection technologies. This information guides the selection, design, and optimization of photodetectors for specific applications, contributing to advancements in optoelectronic devices, imaging systems, telecommunications, and solar energy conversion technologies.

2.6.3 Noise- Equivalent Power (NEP)

Noise-Equivalent Power (NEP) is a critical parameter used to quantify the sensitivity and performance of photodetectors by indicating the minimum detectable optical power level that can be distinguished from the inherent noise of the device. NEP serves as a comprehensive figure of merit, encapsulating the effects of both external and internal noise sources, including thermal noise, shot noise, and amplifier noise. Mathematically, NEP is defined as the amount of optical power required to generate a signal comparable in magnitude to the noise of the photodetector, expressed as in equation (2.10).

$$NEP = \frac{P_{noise}}{R} \quad (2.10)$$

Where P_{noise} is the noise power spectral density and R is the responsivity of the photodetector. The NEP values of photodetectors are inherently influenced by various factors, such as semiconductor material properties, device design, operating conditions, and fabrication techniques. For instance, Silicon (Si) photodetectors typically exhibit NEP values ranging from 10^{-12} to 10^{-14} W/Hz^{1/2} in the visible and near-infrared spectral ranges. In contrast, advanced photodetectors based on Gallium Arsenide (GaAs) and Indium Gallium Arsenide (InGaAs) can achieve lower NEP values in the range of 10^{-15} to 10^{-17} W/Hz^{1/2}, particularly in the near-infrared spectral range, making them highly suitable for high-sensitivity optoelectronic applications and low-light-level detection.

Moreover, NEP serves as a crucial metric for assessing the performance limitations and optimizing the noise characteristics of photodetectors. Lower NEP values indicate higher sensitivity and lower noise levels, enabling enhanced detection capabilities and improved signal-to-noise ratios for various applications, including imaging, spectroscopy, telecommunications, and scientific research. Additionally, careful characterization and optimization of photodetectors are essential to minimize noise contributions from external and internal sources, thereby achieving optimal performance and efficiency across specific spectral ranges and operating conditions.

Furthermore, it is essential to recognize that NEP is inversely proportional to the responsivity (R) and directly proportional to the square root of the bandwidth (B) of the photodetector, as expressed by equation (2.11).

$$NEP \propto \frac{1}{R} \sqrt{B} \quad (2.11)$$

Therefore, improving the responsivity and bandwidth characteristics of photodetectors can lead to reduced NEP values, thereby enhancing the overall sensitivity and performance of the photodetector. In summary, Noise-Equivalent Power (NEP) serves as a critical parameter alongside Quantum Efficiency and Responsivity for evaluating and optimizing the sensitivity, noise performance, and efficiency of photodetectors. Reported NEP values for various semiconductor materials provide valuable insights into the noise characteristics, limitations, and potential of different photodetection technologies, guiding the selection, design, and optimization of photodetectors for specific applications in optoelectronics, imaging, sensing, and scientific research.

2.6.4 Detectivity

Detectivity (D^*) is another important figure of merit used to evaluate the performance and sensitivity of photodetectors by quantifying their ability to detect weak optical signals in the presence of noise. Detectivity combines the effects of Responsivity (R) and Noise-Equivalent Power (NEP), providing a comprehensive metric that accounts for both the signal detection capability and noise characteristics of the photodetector. Mathematically, detectivity is defined as in equation (2.12).

$$D^* = \frac{R\sqrt{A}}{NEP} \quad (2.12)$$

where R is the responsivity, A is the active area of the photodetector, and NEP is the Noise-Equivalent Power.

The detectivity values of photodetectors are inherently influenced by various factors, such as semiconductor material properties, device design, operating conditions, and fabrication techniques. For instance, Silicon (Si) photodetectors typically exhibit detectivity values ranging from 10^{10} to 10^{12} $\text{cm}\cdot\text{Hz}^{1/2}/\text{W}$ in the visible and near-infrared spectral ranges. In contrast, advanced photodetectors based on Gallium Arsenide (GaAs) and Indium Gallium Arsenide (InGaAs) can achieve higher detectivity values in the range of 10^{12} to 10^{14} $\text{cm}\cdot\text{Hz}^{1/2}/\text{W}$, particularly in the near-infrared spectral range, making them highly suitable for high-sensitivity optoelectronic applications and low-light-level detection.

Moreover, detectivity serves as a critical metric for assessing the performance limitations and optimizing the sensitivity, noise performance, and efficiency of photodetectors. Higher detectivity values indicate enhanced detection capabilities, lower noise levels, and improved signal-to-noise ratios, enabling superior performance in various applications, including imaging, spectroscopy, telecommunications, and scientific research. Additionally, careful characterization, optimization, and integration of photodetectors with advanced materials, structures, and technologies are essential to maximize detectivity and achieve optimal performance across specific spectral ranges and operating conditions.

Furthermore, it is essential to recognize that detectivity (D^*) is directly proportional to the square root of the R) and the active area (A) of the photodetector, and inversely proportional to the NEP, as expressed by equation (2.12) above. Therefore, improving the responsivity, active area, and noise characteristics of photodetectors can lead to enhanced detectivity values, thereby enabling superior sensitivity, detection capabilities, and performance of the photodetector.

2.6.5 Dark Current

Dark current is a critical parameter in photodetectors, representing the leakage current that flows through the device even in the absence of incident light. This intrinsic current arises due to thermally generated carriers or defects within the semiconductor material, leading to unwanted noise and reduced signal-to-noise ratio. Mathematically, dark current is typically measured in terms of current density (J) and is defined as the current flowing through the photodetector under dark conditions, expressed in units of amperes per square centimeter (A/cm^2).

The dark current values of photodetectors are inherently influenced by various factors, including semiconductor material properties, device design, operating temperature, fabrication techniques, and the presence of defects or impurities within the material. For instance, Silicon (Si) photodetectors typically exhibit dark current densities ranging from 10^{-9} to 10^{-12} A/cm^2 at room temperature, while advanced photodetectors based on Gallium Arsenide (GaAs) and Indium Gallium Arsenide (InGaAs) can achieve lower dark current densities in the range of 10^{-12} to 10^{-15} A/cm^2 , particularly at lower operating temperatures. These lower dark current values in advanced materials contribute to improved signal quality, higher signal-to-noise ratios, and enhanced performance in various optoelectronic applications requiring low noise and high sensitivity.

2.6.6 Gain

Gain is a pivotal parameter in photodetectors, quantifying the amplification capability by representing the ratio of the output current or voltage to the incident optical power. This metric plays a crucial role in enhancing sensitivity, signal-to-noise ratio, and overall performance by

amplifying weak optical signals and mitigating noise effects. Mathematically, the gain is defined as in

equation (2.13).

$$G = \frac{I_{output}}{P_{incident}} \text{ or } G = \frac{V_{output}}{P_{incident}} \quad (2.13)$$

where I_{output} and V_{output} represent the output current and voltage, respectively, and $P_{incident}$ incident optical power. The gain values of photodetectors are significantly influenced by semiconductor material properties, device design, operating conditions, and fabrication techniques. For instance, Silicon (Si) photodetectors typically exhibit gain values ranging from 10^2 to 10^5 in the visible and near-infrared spectral ranges, while advanced photodetectors based on Gallium Arsenide (GaAs) and Indium Gallium Arsenide (InGaAs) can achieve higher gain values in the range of 10^4 to 10^7 , particularly in the near-infrared spectral range. These higher gain values in advanced materials make them highly suitable for high-sensitivity optoelectronic applications, low-light-level detection, and imaging systems requiring superior performance in various scientific and technological domains.

2.6.7 Linear Dynamic Range

The linear dynamic range (LDR) of a photodetector is a critical parameter that characterizes its ability to detect and measure optical signals across a broad range of input power levels while maintaining linearity in its response. The LDR is defined as the ratio of the maximum detectable

optical power (P_{max}) to the minimum detectable optical power (P_{min}) expressed in decibels (dB). The mathematical representation of LDR in dB is given by equation (2.14).

$$LDR (dB) = 20 \log \left(\frac{P_{max}}{P_{min}} \right) \quad (2.14)$$

A higher LDR value indicates a wider dynamic range, enabling the photodetector to accurately measure both weak and strong optical signals without significant distortion or saturation. Optimizing the LDR is essential for various applications such as imaging, spectroscopy, and telecommunications, where precise measurements over a broad range of operating conditions are required. Achieving a high LDR in photodetector systems involves careful selection of materials, device design optimization, and implementation of signal processing techniques to minimize noise and enhance the signal-to-noise ratio. By maximizing the LDR, researchers, and engineers can design photodetector systems that provide reliable and accurate measurements across a wide range of optical power levels, thereby enhancing the system's sensitivity, reliability, and performance in diverse optical sensing and detection applications.

Understanding and accurately characterizing the LDR of photodetectors are crucial steps in selecting and optimizing these devices for specific applications based on the desired dynamic range and sensitivity requirements. It enables researchers and engineers to design and implement photodetector systems tailored to the application's needs, ensuring optimal performance and reliability in various optoelectronic applications, including imaging, spectroscopy, remote sensing, telecommunications, and scientific research. By optimizing the LDR of photodetectors, it is possible to enhance their utility and effectiveness in capturing and analyzing optical signals across

a wide range of operating conditions, thereby advancing research and development in optoelectronics and photonics.

2.6.8 Response Time

Response time, a crucial parameter in photodetectors, characterizes the speed at which the device reacts to changes in incident light intensity. It is defined as the time taken for the photodetector to achieve a specified percentage (commonly 10% to 90%) of its final output signal in response to a sudden change in illumination. Mathematically, response time (t_r) can be expressed as the time taken for the output signal to transition from 10% to 90% of its final value as in equation (2.15).

$$t_r = t_{90\%} - t_{10\%} \quad (2.15)$$

where $t_{10\%}$ and $t_{90\%}$ are the times at which the output signal reaches 10% and 90% of its final value, respectively. The response time of a photodetector is influenced by various factors, including the device's material properties, structural design, and operating conditions. For instance, Silicon (Si) photodetectors typically exhibit response times ranging from microseconds to milliseconds due to the inherent carrier transport properties and device structure. Advanced photodetectors based on compound semiconductors, such as Gallium Arsenide (GaAs) and Indium Gallium Arsenide (InGaAs), can achieve much faster response times, often in the nanosecond to picosecond range, owing to their superior carrier mobility and shorter carrier transit times.

Optimizing the response time of photodetectors is crucial for applications requiring rapid signal detection and processing, such as high-speed communications and time-resolved spectroscopy.

Strategies for improving response time include material engineering to enhance carrier mobility, device design optimization to minimize parasitic capacitances and resistances, and operating condition adjustments. Careful characterization and measurement of response time are essential for accurately assessing the device's speed and responsiveness, guiding the selection and optimization of photodetectors for specific applications in optoelectronics, sensing, and scientific research.

2.7 Noise in Photodetection

Noise in photodetectors is a multifaceted phenomenon that can be described and analyzed through various mathematical models and equations. The following are the types of noise commonly encountered in photodetectors:

2.7.1 Thermal Noise (Johnson-Nyquist Noise)

Thermal noise arises from the random thermal motion of charge carriers within the photodetector's semiconductor material. The noise voltage spectral density (S_V) due to thermal noise in a resistor (R) at temperature (T) is given by equation (2.16).

$$S_V = 4k_B TR\Delta f \quad (2.16)$$

where k_B is Boltzmann's constant, T is the absolute temperature in Kelvin, and Δf is the bandwidth.

2.7.2 Shot Noise

Shot noise results from the discrete nature of charge carriers and is proportional to the square root of the photocurrent. The noise current spectral density (S_I) due to shot noise can be expressed as in equation (2.17).

$$S_I = 2qI\Delta f \quad (2.17)$$

where (q) is the charge of an electron, (I) is the photocurrent, and Δf is the bandwidth.

2.7.3 Flicker Noise (1/f Noise)

Flicker noise is characterized by its increase at lower frequencies and is often modeled using a power law relationship. The noise voltage spectral density (S_V) due to flicker noise can be represented as in equation (2.18).

$$S_V = Af^{-\alpha} \quad (2.18)$$

where A is a constant, f is the frequency, and α is the noise exponent typically between 0 and 2.

2.7.4 Amplifier Noise

Amplifier noise contributes to the overall noise in the photodetector system and is often described by the amplifier's noise figure (NF) and the amplifier's gain (G). The noise power (N_{amp}) due to amplifier noise can be calculated using equation (2.19).

$$N_{amp} = NF \times k_B T \times \Delta f \times G \quad (2.19)$$

Understanding these noise sources and their mathematical descriptions is crucial for optimizing photodetector performance by minimizing noise and maximizing signal-to-noise ratio, thereby enhancing the device's sensitivity and reliability in various applications.

The total noise in a photodetector is the cumulative effect of various noise sources present within the device and its associated electronics. It can be expressed as the sum of the individual noise contributions from thermal noise, shot noise, flicker noise, amplifier noise, and any other sources that may be present. Mathematically, the total noise (N_{total}) in a photodetection can be calculated as the root sum square (RSS) of the individual noise components given in equation (2.20).

$$N_{total} = \sqrt{N_{thermal}^2 + N_{shot}^2 + N_{flicker}^2 + N_{amplifier}^2 + \dots} \quad (2.20)$$

where $N_{thermal}^2$, N_{shot}^2 , $N_{flicker}^2$, $N_{amplifier}^2$, etc., represent the individual noise contributions from thermal noise, shot noise, flicker noise, amplifier noise, and other relevant sources, respectively.

Each noise component contributes differently to the total noise depending on factors such as the device's operating conditions, bandwidth, and electronic components used in the photodetector system. Understanding and accurately characterizing the total noise in a photodetector system is crucial for optimizing its performance and ensuring reliable operation in various applications, including imaging, spectroscopy, communications, and scientific research.

CHAPTER 3

MATERIALS AND METHODS

3.1 Experimental Procedures

Chemicals and materials: Methyl ammonium iodide ($\text{CH}_3\text{NH}_3\text{I}$, MAI, 99.95%), Lead (II) iodide (PbI_2 , 99.999%) and Lithium iodide (LiI , 99.999%), Dimethyl sulfoxide (DMSO, ≥ 99.9), N, N-dimethylformamide (DMF, $\geq 98.8\%$) and Titanium isopropoxide, Ti-Nanoxide (mesoporous titanium dioxide, T/SP, m- TiO_2) were all purchased from Sigma-Aldrich. Ethanol and 2-propanol were purchased from Alfa Aesar. All these chemicals were used without any modification.

3.2 Material Synthesis

3.2.1 Synthesis of MAPbI_3

The undoped-methyl ammonium lead iodide (MAPbI_3), which is the absorber layer material, was synthesized based on the procedure described elsewhere²¹¹. 162mg of MAI and 462 mg of PbI_2 was dissolved in a 1ml mixture of DMF and DMSO (7:3, v/v). The mixture was then stirred at 1000 rpm for 24hrs at 80 °C. The light-yellow solution was then filtered with PTFE filters to remove an unreacted portion of the mixture. The Li dope MAPbI_3 was prepared by adding varying molar concentration ratios of LiI (2, 5, 7, and 10 mol%) to make the precursor solutions, stirred, and filtered as in the previous. All preparations were carried out in a glovebox filled with nitrogen gas.

3.2.2 Preparation of mesoporous and compact TiO₂

The m-TiO₂, which is the electron transport layer material, was prepared by diluting T/SP nanoxide in ethanol at a mass ratio of (2:7) in a small vial and the mixture was sonicated in a Branson ultrasonic bath for 1hr. As for compact TiO₂ (c-TiO₂), the hole-blocking layer material, two different solutions were formed. First, 369 μl of titanium isopropoxide was diluted in 2.53 ml of 2-propanol in a small vial forming solution 1; Solution 2 was formed by diluting 35μl of 2 M-solution HCL in 2.53 ml of 2-propanol forming 0.013 M of HCL. The two solutions were then mixed and stirred vigorously to obtain a clear jelly-like solution which was used within 2 hours after preparation.

3.2.3 Preparation of Ni₂O₃ solution

The Nickel (III) oxide (Ni₂O₃) solution was prepared by diluting 20mg of Ni₂O₃ powder in a 1ml mixture of water and ethanol with a ratio of 2:1 (v/v).

3.3 Fabrication processes

3.3.1 Fabrication of Photodetector Based on NF and NN Faces

The deposition and fabrication processes are schematically depicted in Figure 9. An FTO glass sized 2.5 x 2.5 cm² was cleaned with soap, then ultrasonicated in deionized water, ethanol, and acetone for 20 min each respectively, and dried afterward.

- **Fabrication of NF-face:** Fabrication of NF-faces of the photodetectors (PDs) was carried out by spin-coating 150 μl of c-TiO₂ at 4000 rpm for 30 s and then annealed at 450 °C in a fume-

hood for 30min. After cooling down a layer of m-TiO₂ was then deposited by spin-coating 150 μl of m-TiO₂ solution at 4000 rpm for 30 s and then annealed at 450 °C in a fume-hood for 30 min. The absorber layer material was then deposited by spin-coating 150 μl of as-synthesized MAPbI₃ with varying molar ratios of LiI (0, 2, 5, 7, and 10 mol%) at 4000 rpm for 30 s and then annealed at 80 °C inside the glovebox for 30 min.

- **Fabrication of NN-face:** The NN-faces of the PDs were fabricated by spin-coating 150 μl of Ni₂O₃ solution at 4000 rpm for 30 s. The films were annealed at 110 °C for 30 min inside the glovebox. After it cools down a layer of absorber material is then deposited and annealed as before.

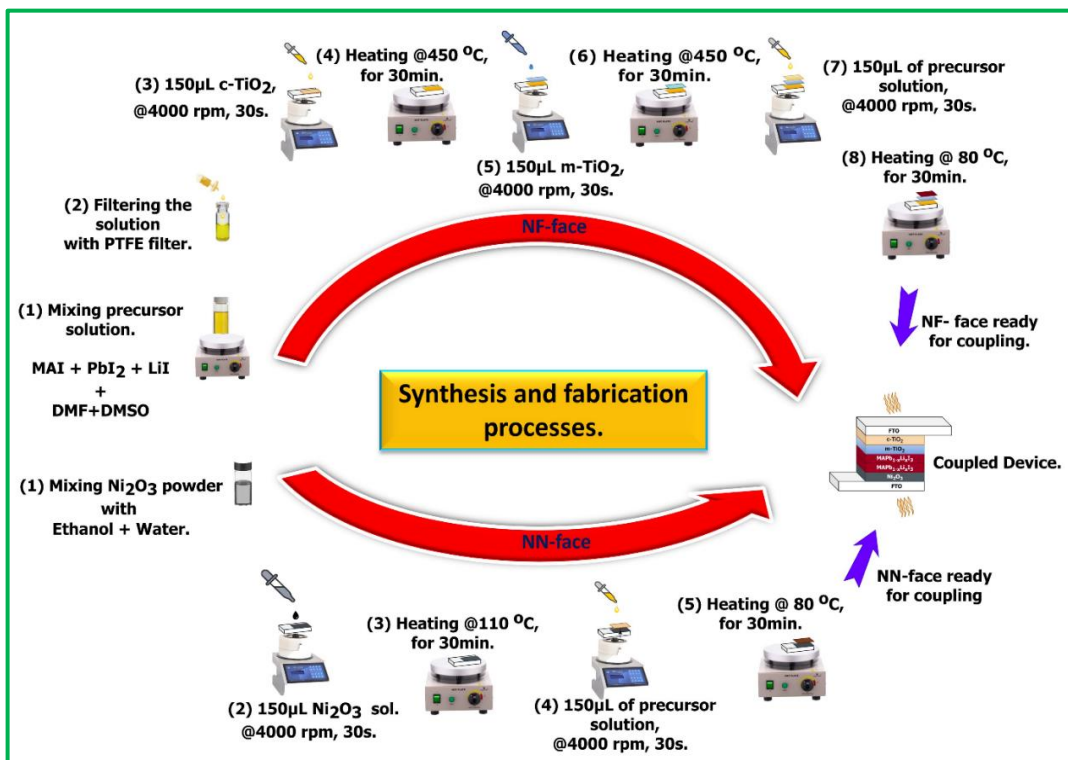


Figure 9: Schematic of the synthesis of undoped and Li-doped perovskite material and fabrication processes of photodetectors based on NF and NN-faces.

The film thicknesses of the ETL (FTO/m-TiO₂), HTL (FTO/Ni₂O₃), and HBL (FTO/m-TiO₂) were measured to be 56nm, 64nm, and 68nm respectively. The thicknesses of the doped (FTO/MAPbI₃) and undoped (FTO/MAPbI₃: Li) absorber layers averaged at 550nm and for the complete NF and NN-faces the film thicknesses averaged at 665nm and 203nm respectively. The two faces of the PDs were then coupled together to complete the device architecture as shown in Figures 7 and 8. The fabricated devices were code-named PD0 (0 mol%), PD2 (2 mol%), PD5 (5 mol%), PD7 (7 mol%), and PD10 (10 mol%) accordingly. The complete architectures of the fabricated devices were shown in Figure 10.

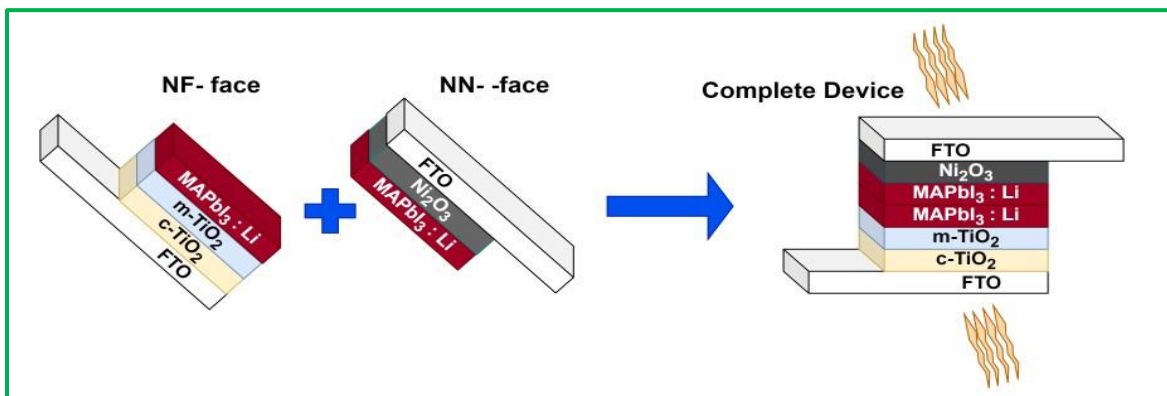


Figure 10: Proposed device architecture based on NF and NN-faces.

3.3.2 Photodetectors Based on T, N, and NN Faces

The complete fabrication processes of T, N, and NN-faces are schematically depicted in Figure 11.

- **Fabrication of T-face:** The fabrication of T-faces was carried out in a similar way to NF faces described above.
- **Fabrication of N-face:** The N-faces were fabricated by spin-coating 150 μL of Ni_2O_3 solution at 4000 rpm for 30 seconds. The resulting films underwent annealing at 110 $^\circ\text{C}$ for 30 minutes inside the glovebox.
- **Fabrication of NN-face:** Also, fabrication of NN-face was the same as described above (Figure 10).

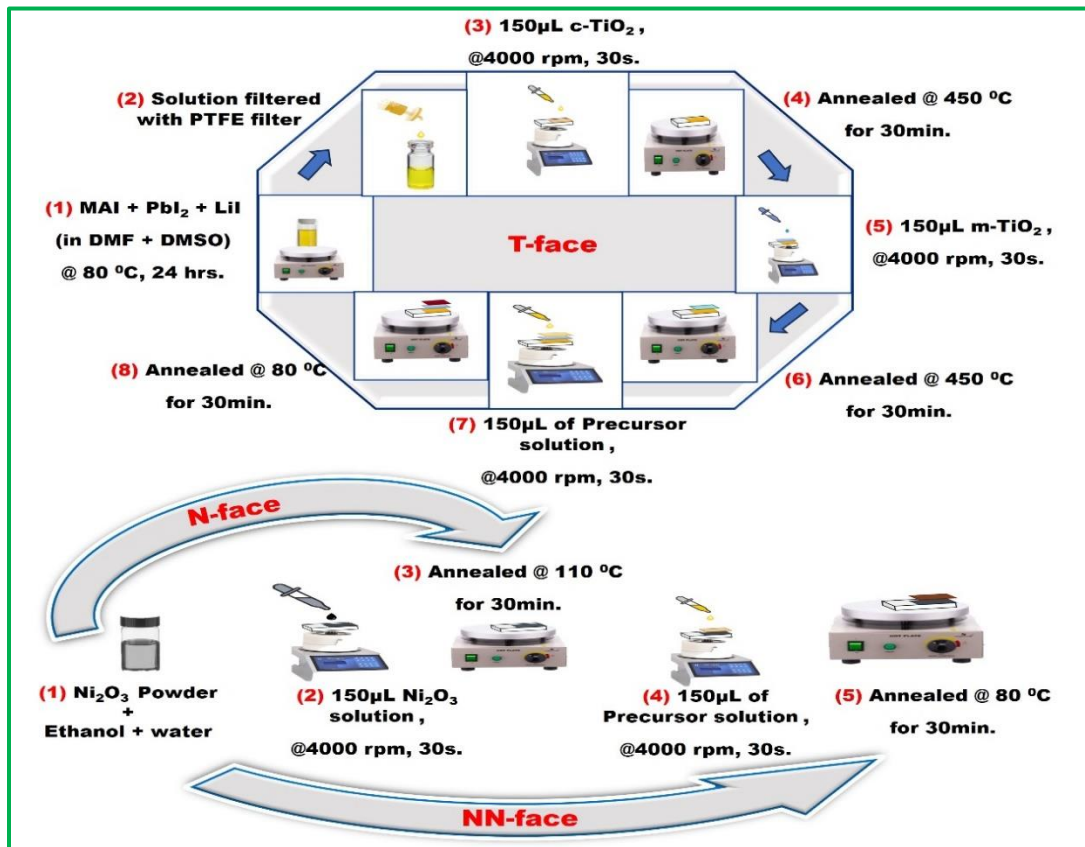


Figure 11: Schematic of the synthesis of undoped and Li-doped perovskite material and fabrication processes of photodetectors based on T, N, and NN-faces.

The PDs fabricated based on T, N, and NN-faces have been systematically code-named for clarity in referencing (Figure 11a-d). PD0-A, PD0-B, PD5-A, and PD5-B represent devices with and without LiI additives and different absorber layer configurations (Figure 9a-d). Specifically, PD0-A is constructed with a single layer of absorber material containing 0 mol% LiI, PD0-B has a double absorber layer with 0 mol% LiI, PD5-A features a single layer with 5 mol% LiI, and PD5-B incorporates a double absorber layer with 5 mol% LiI. The face designations include T-faces for all photodetectors based on the architecture FTO/c-TiO₂/m-TiO₂/MAPbI₃ for PD0-A, and PD0-B, FTO/c-TiO₂/m-TiO₂/MAPbI₃-Li for PD5-A and PD5-B. Additionally, PD0-A and PD5-A have N-faces based on FTO/Ni₂O₃, while PD0-B and PD5-B have NN-faces based on FTO/Ni₂O₃/MAPbI₃ and FTO/Ni₂O₃/MAPbI₃-Li respectively. The complete architecture of the fabricated devices is shown in Figure 12.

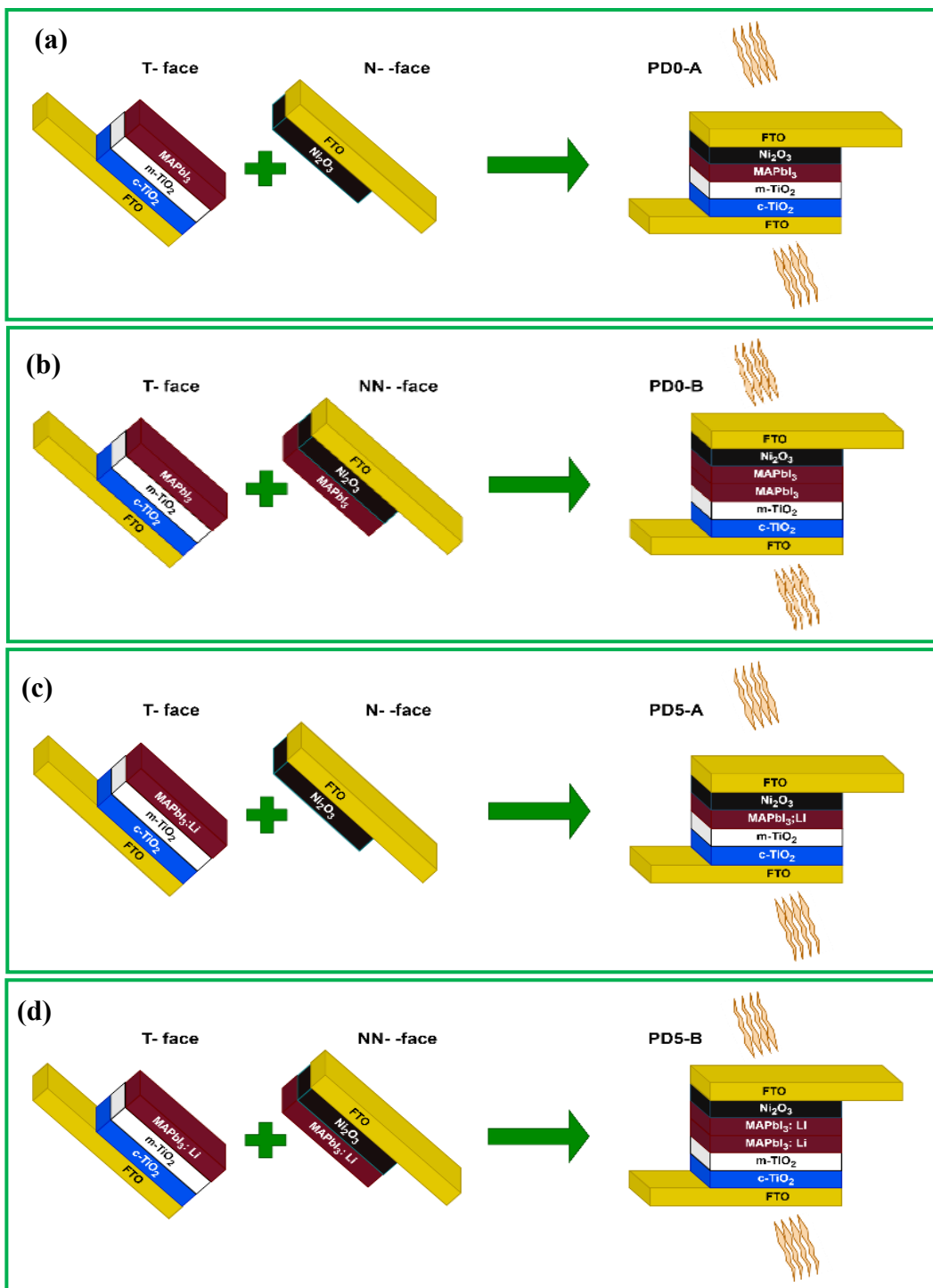


Figure 12: The proposed device architectures based on T, N, and NN faces.

3.4 Material Characterizations

Various sophisticated techniques were employed for in-depth material characterizations to ensure the quality and composition of the prepared films. Film thickness measurements were conducted using a Bruker DektakXT profilometer equipped with a stylus radius tip of 12.5 μm . Field emission scanning electron microscopy (FESEM/FIB/GIS-Tescan Lyra3) was utilized to generate high-resolution images of the films. X-ray diffraction (XRD) was conducted using a D2 Phaser 2nd Generation diffractometer equipped with a Cu K α ($\lambda = 1.54 \text{ \AA}$ wavelength) X-ray source. This method facilitated the identification and quantification of perovskite phases within the films, contributing crucial information about the crystalline structure and purity of the materials. X-ray photoelectron spectroscopy (XPS) analysis was carried out using an ESCALAB 250Xi spectrometer. With a spatial resolution of 100 μm , this technique enabled the determination of the distribution of binding energies of excited electrons. Additionally, XPS provided insights into the chemical composition and chemical states of elements present in the top few atomic layers of the as-prepared films. Absorption spectra of both faces of each device were obtained using a UV-Vis Spectrophotometer (Jasco v 670) equipped with a double monochromator. This allowed for a detailed analysis of the devices' optical properties, providing information about their absorption characteristics across the UV and visible spectra. Steady-state photoluminescence (PL) spectra were captured using an FP-8250 Spectrofluorometer. This technique provided valuable insights into the emission properties of the materials, aiding in the understanding of their electronic structure and performance. These comprehensive material characterizations collectively ensured a thorough understanding of the structural, compositional, and optical properties of the fabricated

films and devices, contributing to the overall assessment of their performance and potential applications.

3.5 Device Characterizations

The performance of the fabricated devices was meticulously characterized through a series of electrical and optical measurements. The current-voltage (I-V) characteristics of the devices were assessed using a Tektronix-Keithley 2450 source meter. This measurement was conducted in both manual trigger mode and swift mode, employing a scanning rate of 100 mV/s and a bias voltage range from -2 to 2V. These I-V curves provide essential information about the electrical behavior and performance of the devices. A solar simulator from Newport-Oriel instruments, featuring a xenon lamp powered by OPS-A150 (50-500W, RS-232/USB) power supply, was employed to illuminate the devices at varying power intensities. This allowed for a systematic investigation into the response of the devices under different illumination conditions. A T206 Digital Solar Power Meter was utilized to precisely measure the power of the light irradiance provided by the simulator, ensuring accurate characterization. The transient photocurrent characteristics, represented by I-t curves, were measured using a CORRTEST Potentiostat/Galvanostat/electrochemical workstation model CS350. This analysis was conducted under the illumination of Helium-neon lasers (10mW power). The transient behavior of photocurrent provides insights into the response time and dynamic performance of the devices under specific optical excitation conditions. These comprehensive characterizations collectively offer a detailed understanding of the electrical and optical properties of the fabricated devices. The combination of I-V characteristics, illumination

studies, and transient photocurrent measurements provides a holistic assessment of the devices' performance, aiding in the evaluation of their suitability for photodetection applications.

CHAPTER 4

RESULTS AND DISCUSSIONS

4.1 Assessment of the Material Properties

Firstly, it should be noted that NF and T-faces were fabricated with the same material and layer structures. Therefore, we restrict the discussion to NF-faces, which encompasses both NF and T-face accordingly.

4.1.1 Morphological Investigation of Perovskite Films

Morphological assessment of the perovskite absorber layer was conducted (Figure 13a-f) using advanced field-emission scanning electron microscopy (FESEM) to examine the structure and coverage of MAPbI₃ thin films and grains, comparing samples prepared with LiI to a control sample without LiI. The images of both NF and NN-faces revealed a nearly common characteristic among perovskite films made with the same face architecture, with NF-faces displaying high coverage, forming continuous, well-distributed layers as depicted in Figure 13a–f. This coverage uniformity reflects the efficacy of the deposition process and the impact of additives in ensuring consistent substrate coverage, a crucial factor in optimizing device performance and reliability for potential applications. At a scale of 10 μm, the predominant morphology of the faces (in both NF and NN) is characterized by structures resembling roots or brooms, extending from both ends in a branching pattern. Further magnification to 5 μm (Figure 13f), exposes the nature of these structures, in both NF and NN-faces revealing a network of root-like formations beneath which

micro-sized m-TiO₂ particles are discernible. The observed variations between NF and NN-faces in terms of coverage and crystallinity may likely be attributed to more favorable surfaces provided by m-TiO₂. Considering the properties of m-TiO₂ and Ni₂O₃ and their interaction with the precursor solution, it is likely that m-TiO₂ will provide a greater surface area for the nucleation and growth of perovskite crystals. The high surface area of m-TiO₂ due to its porous structure will allow for a greater amount of precursor solution to be adsorbed, providing more available reaction sites for the growth of perovskite crystals.

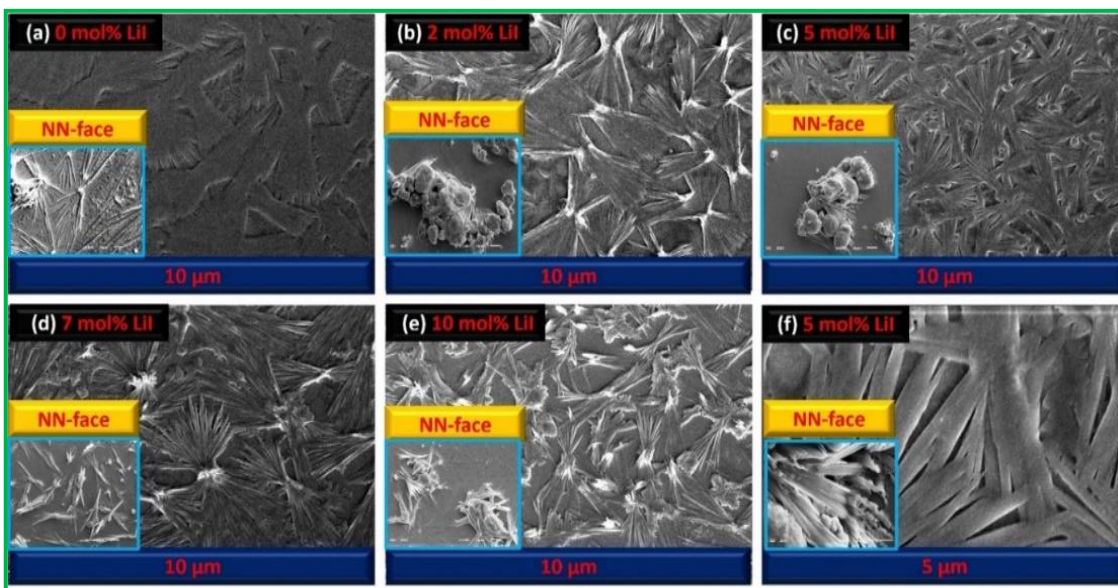


Figure 13: (a-e) Top view of the NF -faces and NN-faces (inset) of the fabricated devices based on FTO/c-TiO₂/m-TiO₂/MAPbI₃ and FTO/Ni₂O₃/MAPbI₃ configurations respectively, with different molar concentrations of LiI additive, (f) NF-face with 5 mol% LiI @ 5 μm

Figure 14a-b depicted the EDX spectra of NF-face with 5 mol% LiI showing elemental compositions with most expected elements appearing in reasonable proportions. The observed

morphological variances significantly influence the overall performance disparities between the two faces, and in turn, the performance of individual photodetectors. This underscores the critical role that morphology plays in tailoring the functionality and performance of merits of these devices, aligning with the broader objectives of optimizing photodetection technologies.

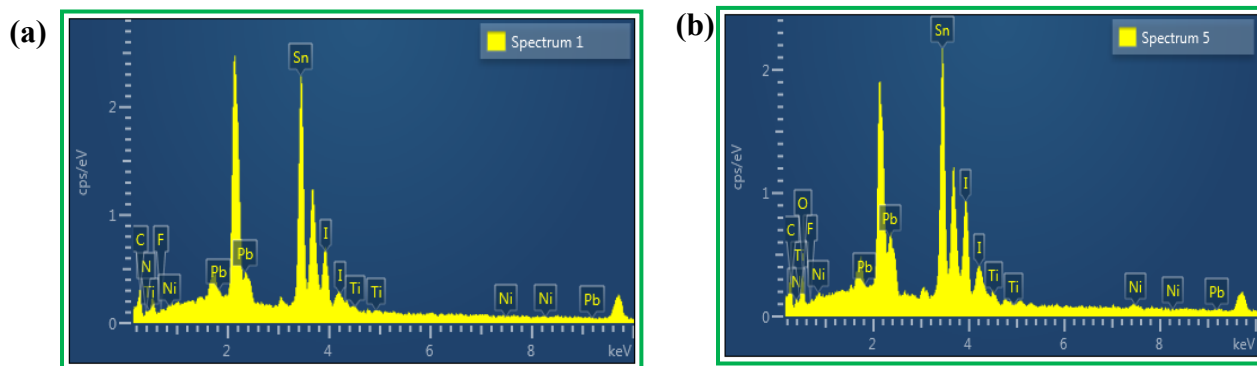


Figure 14: (a) EDX spectra of a face with 0 mol% LiI and (b) EDX spectra of a face with 7 mol% LiI.

4.1.2 Crystal Structure Analysis

Figure 15 provides the X-ray diffraction (XRD) pattern for the perovskite films prepared with varying concentrations of LiI incorporated into the precursor solutions. Notably, the XRD pattern of all perovskite films consistently exhibits characteristic diffraction peaks corresponding to the (110), (220), (310), (224), and (314) crystal planes at 2θ values of 14.18° , 28.97° , 31.81° , 41.31° and 43.58° respectively. These sets of peaks are all indexed to a tetragonal structure²¹². Additionally, the presence of a discernible peak related to PbI_2 (at about 12.40°), a common observation in MAPbI_3 films, is noted across all samples²⁸. The variations in XRD patterns

exhibited by the NF-face and NN-face highlight the inherent structural disparities resulting from the tailored growth conditions and the use of distinct materials. The variations in crystallographic orientation and diffraction peaks can be linked to the specific layers and interfaces in each architecture. Remarkably, upon closer examination, all the peaks (in both NF and NN faces) shifted towards lower angles due to the introduction of LiI, as shown when we zoomed in at representative peaks of NF-faces (110) and NN-faces (224) in Figure 16a-c, which is consistent with previous studies²¹³⁻²¹⁵. This has enabled us to quantitatively deduce the lattice expansions of the inter-planer spacing as shown in Figure 16c for the two representative peaks. Although both substitutional and interstitial occupancy are thermodynamically possible, this shift to lower angles suggests that the lattice expands due to interstitial occupancy as supported by the theoretical studies^{214,215}. Moreover, the slight variation in the widths of the diffraction peaks for all samples suggests that the doping does not cause many significant alterations in grain size, a notable departure from findings in previous studies involving Na and K doping, where substantial changes in grain size were observed²⁸. The impact of several other dopants was also reported from experimental²¹⁶ and theoretical studies^{214,217}. These underscore the nuanced effects of different dopants on the perovskite structure and properties. This crucial observation signifies that the inclusion of LiI as an additive does not induce significant alterations in the crystal structure of the perovskite films, thereby affirming the structural stability of the perovskite material under present doping conditions.

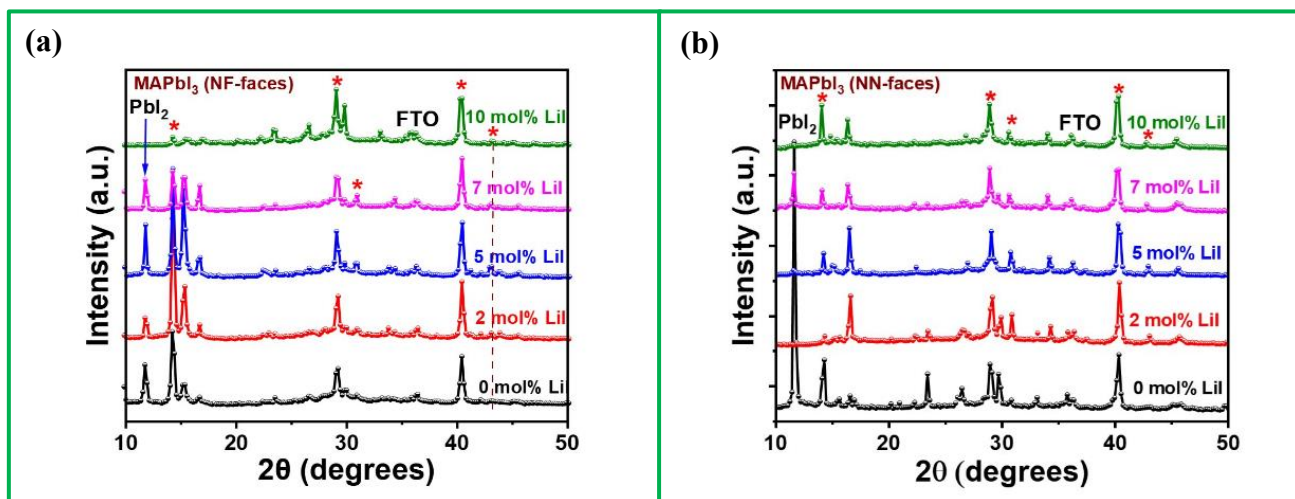


Figure 15: X-ray diffraction patterns (a) NF-faces (b) NN-faces.

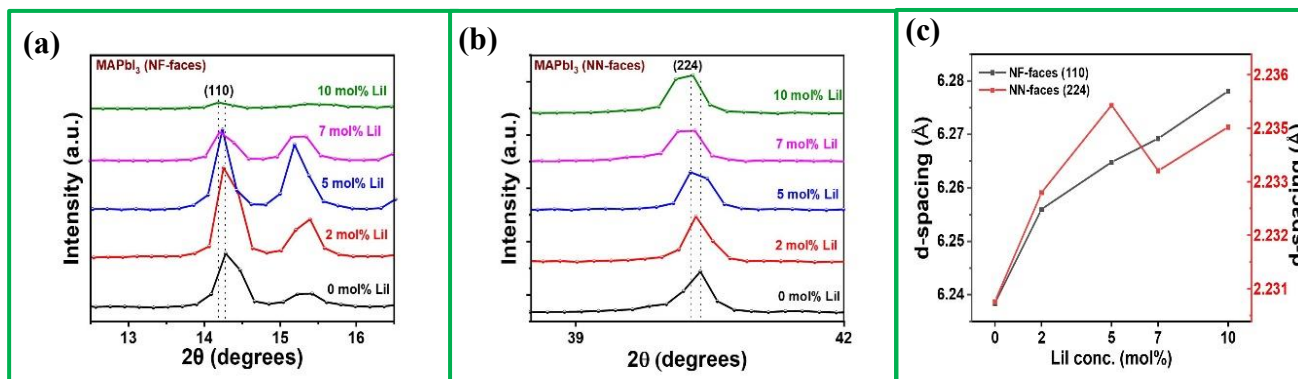


Figure 16: Zoomed in on the XRD spectra of two representative peaks of (a) NF-faces (110), and (b) NN-faces (224); (c) The d-spacing of the NF- and NN-faces plotted from the peaks of (110) and (224) respectively.

4.1.3 Electronic Structure and Elemental Investigations

The XPS (Figure 17 and 18) measurements were also conducted to ascertain the presence of Li ions (Li^+) and to investigate the chemical states of elements within the perovskite film. However, quantitatively determining the lithium (Li) content in the films presents a challenge due to the extremely low sensitivity factor of Li in X-ray photoelectron spectroscopy (Figure 17f)²¹⁵. Compared to other halide perovskites, MAPbI_3 possesses a relatively larger unit cell and experiences less distortion of its octahedra PbI_6 ³⁵. These structural features make it energetically favorable for Li atoms to occupy interstitial sites in the lattice, contributing to the stability of the material even at low Li concentrations. Interestingly both NF and NN-faces of the fabricated devices showed identical XPS spectra as depicted in Figures 17a and 18a. Figure 17e showed the identified peaks in the zoom-out view of the representative spectra obtained from the sample with 5mol% compared to the pristine MAPbI_3 . Importantly, in our experiments, the addition of LiI does not cause the liberation of Pb^0 due to conversion reaction, as reported for high doping levels³⁵. This information suggests that the incorporation of Li in the low doping range is thermodynamically stable and does not introduce significant structural changes in the perovskite material, which is an important consideration for its potential use in various applications. The two peaks symmetrically located around 143 eV and 139 eV are assigned to the Pb $4f_{5/2}$ and Pb $4f_{7/2}$, respectively (Figures 17b and 18b). The two I 3d signals, corresponding to I3 $d_{3/2}$ and I3 $d_{5/2}$ peaks, are also clearly seen at 631 and 619 eV (Figures 17c and 18c). A single peak attributed to N1s also appeared around 402.5 eV (Figures 17d and 18d). Remarkably, the incorporation of LiI into the MAPbI_3 film resulted in a noticeable downward shift of all peaks to lower binding energies. This

shift strongly suggests changes in the chemical environment, electronic states, and charge transfer processes among the constituent atoms within the material. The observed spectral shifts serve as clear indicators of lattice expansions in the MAPbI₃ crystals, attributed to the introduction of Li⁺ ions, leading to elongated Pb–I bonds and lower binding energies for both Pb 4f and I 3d. This phenomenon aligns with findings reported by Fun Yang et al., who observed similar peak shifts to lower energy with the incorporation of MgI₂²¹⁸. Additionally, Alahbakhshi M. reported a high-energy shift upon adding LiPF₆ to CsPbBr₃: PEO film²¹⁵. This information indicates that the XPS measurements confirm the presence of Li ions (Li⁺) in the perovskite films and provide insight into the chemical states of the atoms within the material. This observation aligns with the expected behavior when Li occupies vacancies of Pb in the crystal lattice and agrees with both experimental and theoretical findings^{219,220}.

The observed back-and-forth shifting of peaks (in both NF and NN-faces) observed may indeed be related to the optimum concentration of LiI. Initially, the introduction of Li may disrupt the local electronic environment, leading to shifts towards lower binding energies. However, as equilibrium is established, these shifts may revert or even exceed their original values, indicating a dynamic restructuring of the material's electronic states. Achieving an optimal concentration is crucial in influencing the material's properties, including its electronic structure. The shifting patterns could be indicative of a delicate balance between the introduction of LiI and its impact on the local environment, electronic states, and charge transfer processes within the perovskite lattice. This phenomenon highlights the importance of carefully tuning the concentration of LiI to

maximize the desired effects while avoiding undesirable alterations that might lead to shifts in XPS peaks.

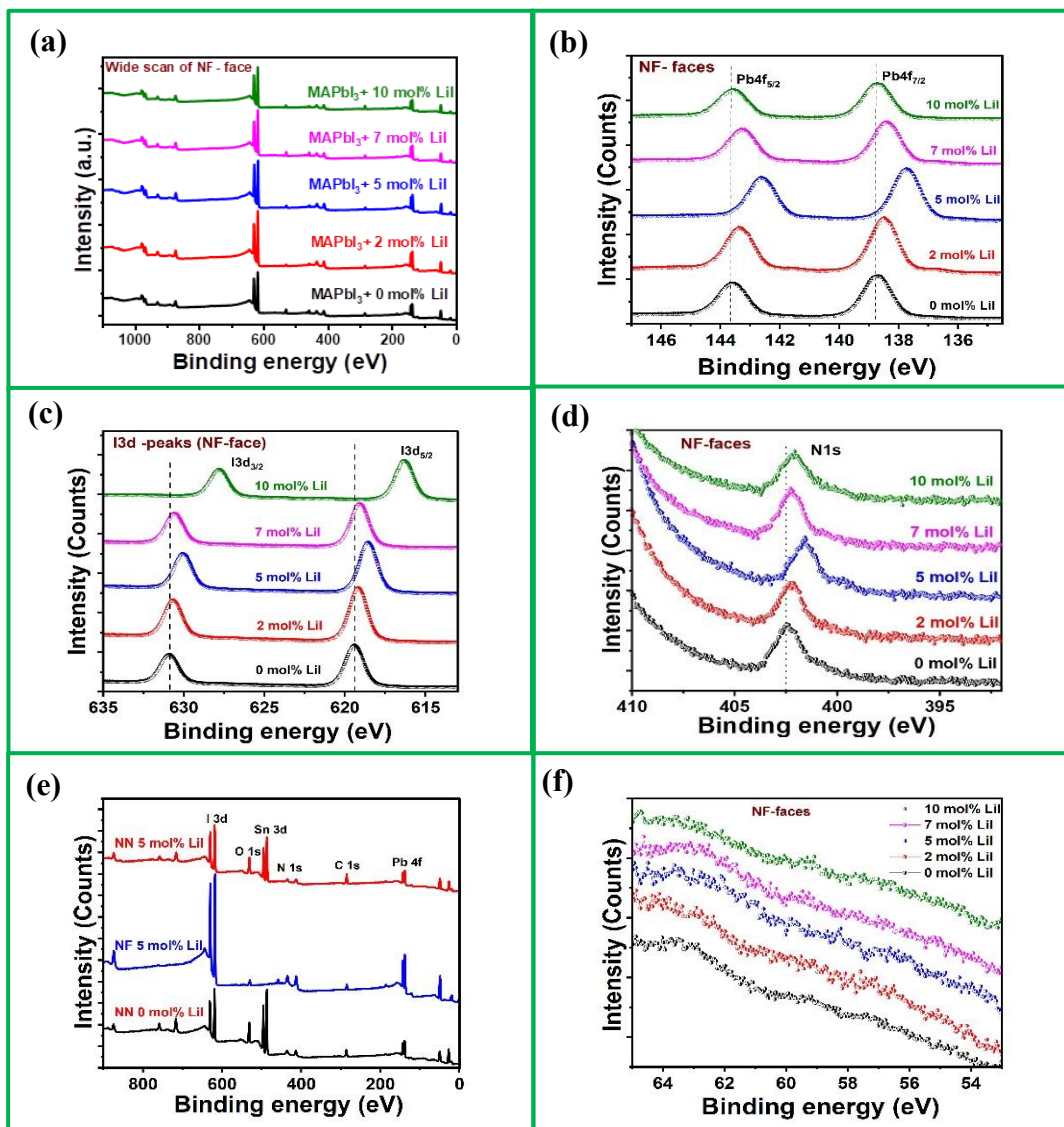


Figure 17: (a) XPS wide scan spectra of the NF-faces; (b) XPS scans of the Pb 4f measured for un-doped and Li-doped samples (c) I 3d XPS core level spectra (NF-faces), and (d) N 1s core level spectra (NF-faces); (e) XPS wide scan spectra of the NF-faces and NN-faces with 5 mol% LiI compared to the sample with 0 mol% LiI; (f) Expected position of lithium peak.

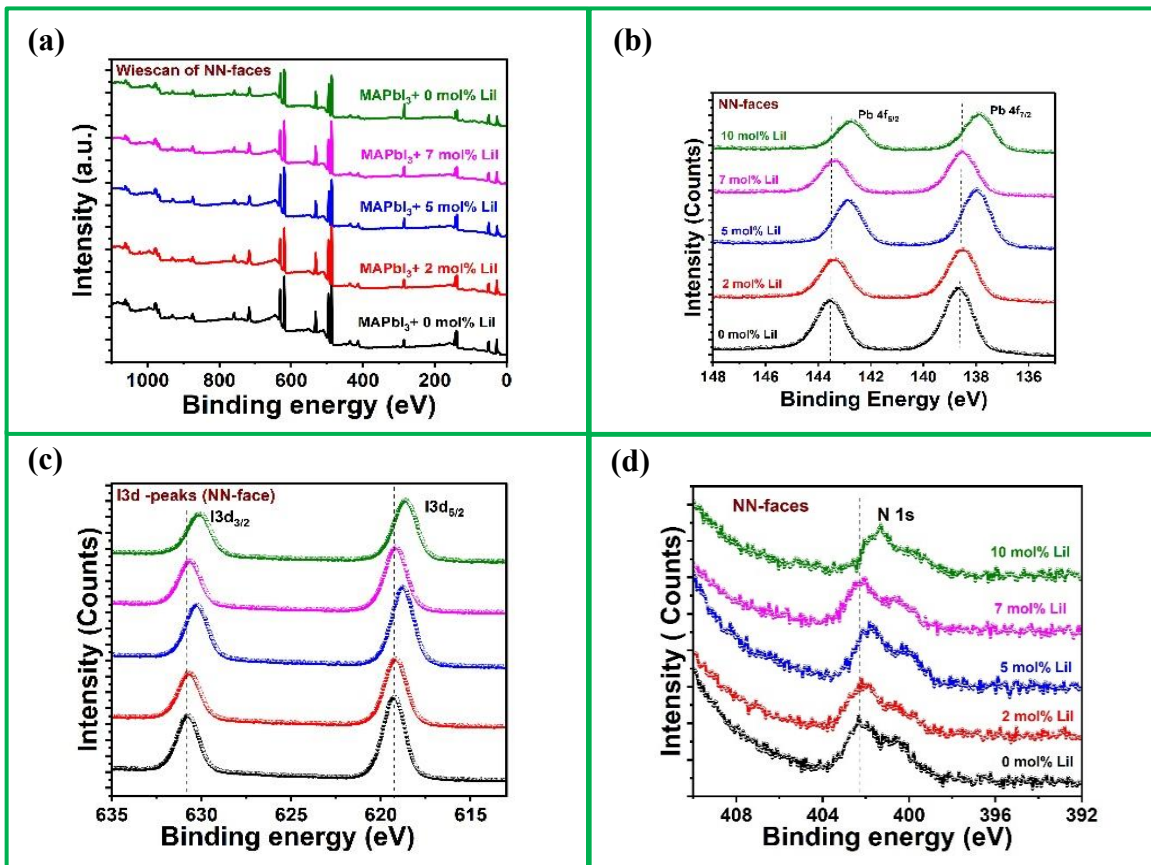


Figure 18: (a) XPS wide scan spectra of the NN-faces; (b) XPS scans of the Pb 4f measured for un-doped and Li-doped samples (c) I 3d XPS core level spectra (NN-faces), and (d) N 1s core level spectra (NN-faces).

4.1.4 Optoelectrical Characterizations of the Material

The introduction of LiI into the precursor solution for perovskite films brings about a significant enhancement in their Ultraviolet-Visible (UV-vis) light absorption characteristics ²²¹. This phenomenon is visually represented in Figure 19a-b, which showcases the UV-vis absorption spectra of these films produced using different concentrations of LiI in the precursor solution.

Notably, the incorporation of LiI doesn't induce changes in the optical bandgap of perovskite films. This observation is evident not only from the absorption spectra shown in Figures 18a-b but also from the photoluminescence (PL) spectra depicted in Figures 19c-d. However, the addition of LiI has profoundly elevated the capacity of light absorption across the Ultraviolet-Visible spectrum^{222,223}. As the concentration of LiI increases, the perovskite films exhibit a gradual escalation in their absorption of visible light, ultimately reaching a maximum when LiI content reaches 5 mol%. This intriguing trend can plausibly be attributed to the superior film coverage and quality of the perovskite crystals attained under these conditions. However, it's worth noting that exceeding a 5 mol% LiI concentration results in a decline in light absorption, aligning with the observations elucidated in Figure 13a-f. This phenomenon, as illustrated, underscores the intricate relationship between LiI doping and the photophysical properties of the resulting perovskite films. It appears that within the studied range of LiI concentrations, there exists an optimal level, at 5 mol%, which induces a remarkable increase in light absorption. This improvement is likely tied to the crystalline quality of the perovskite material, or due to the introduction of defect states within the bandgap of the material. The likely introduced defects state can induce new energy levels within the bandgap, which means that there are more available energy levels for electrons to transition to when absorbing photons with energies close to the bandgap. Suggesting that at this specific dopant concentration, the perovskite structure is most favorably modified. Beyond this point, a diminishing trend in light absorption is observed, revealing the delicate balance that governs these optical properties. These findings closely align with the results presented in Figure

13a-f and have been reported in literature^{31,222}, providing further evidence of the impact of LiI doping on perovskite film characteristics.

The distinctive patterns in the absorbance spectra of NF-faces and NN-faces (Figure 19a-b) underscore the structural disparities between the two faces of the constructed devices. Specifically, the absorbance spectra of NF-faces exhibit a consistent pattern, as do the spectra of NN-faces. In general, NF-faces display higher absorbance across a broader range of the visible spectrum compared to NN-faces. This contrast could be attributed to variances in how the electron transport material (TiO_2) and the hole transport material (Ni_2O_3) interact with incident light, suggesting that the design and composition of each face play a crucial role in their optical properties. However, the moderately high absorbance observed below 400 nm suggests that these photodetectors have the potential for utilization as ultraviolet (UV) detectors. Moreover, the range of wavelengths within which these devices exhibit light absorption is extensive enough to categorize them as broadband photodetectors, as the devices displayed light absorption characteristics spanning ultraviolet, visible, and even a portion of the near-infrared (IR) regions.

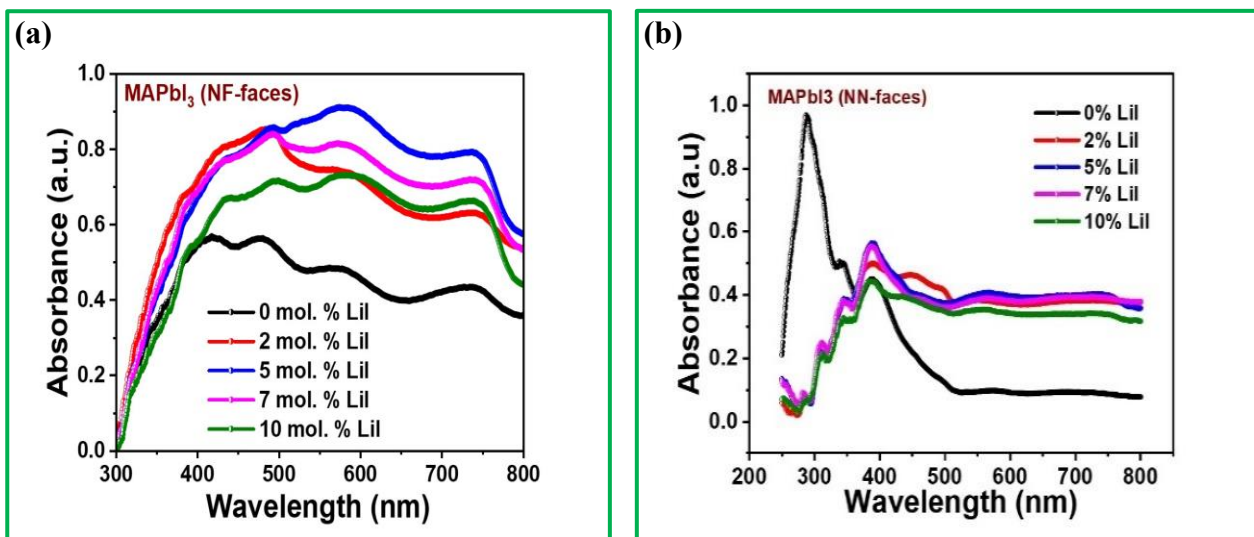


Figure 19: Absorbance spectra of (a) NF-faces based on FTO/c-TiO₂/m-TiO₂/MAPbI₃: Li, (b) NN-faces based on FTO/Ni₂O₃/MAPbI₃: Li.

Steady-state photoluminescence (PL) measurements carried out on perovskite films with varying concentrations of LiI revealed a consistent peak at around 650 nm as shown in Figure 20a-b. The consistent optical bandgap, as revealed by both absorption and PL spectra, highlights that the introduction of LiI maintains the characteristic features of the perovskite films without significant alterations in their optical properties. Notably, the intensity of PL spectra indicates that the addition of LiI to the precursor solution results in more efficient extraction of charge carriers, particularly in 5 mol% samples. The increased PL intensity in the material with 5 mol% relates to the decreased trap density (or defects state) which would facilitate carriers in the excited state to recombine radiatively to the ground. The results dictate that introducing the LiI is an effective way to achieve

better film quality and reduction in trap density in perovskite crystals. This optimized charge-carrier extraction is essential for enhancing the performance of perovskite-based photodetectors.

In this context, the observation that 5 mol% LiI performs better than 7 mol% and 10 mol% suggests that there is an optimal concentration range for LiI that maximizes film quality and device performance²²². While LiI incorporation can enhance the film quality by promoting better crystallinity, reduced defects, and improved charge carrier mobility, the optimal concentration may not necessarily be the highest one³¹. Excessive LiI concentration beyond an optimal level may lead to undesirable effects such as phase segregation, increased defect density, or altered stoichiometry, ultimately compromising film quality and device performance. Additionally, higher LiI concentrations may affect the perovskite crystallization process, leading to non-ideal film morphology or incomplete coverage.

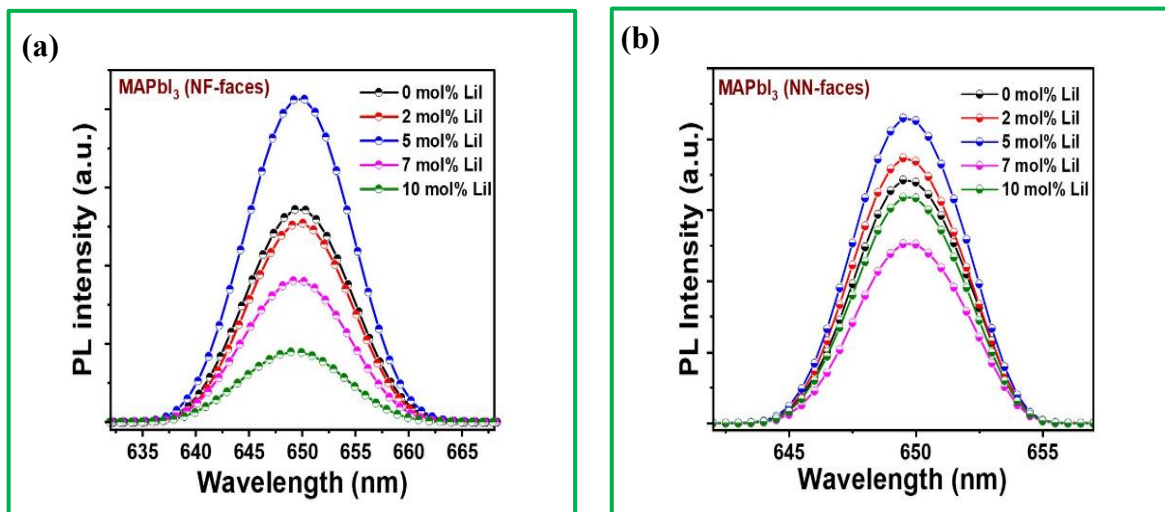


Figure 20: Photoluminescence spectra (a) NF-faces based on FTO/c-TiO₂/m-TiO₂/MAPbI₃: Li, (b) NN-faces based on FTO/Ni₂O₃/MAPbI₃: Li.

4.1.5 Charge Transfer and Recombination Mechanisms

The efficient movement of electrons and holes within the absorber material, as well as their ability to jump or slide to or between transport materials and electrodes, plays a crucial role in the overall performance of photon detection devices. The energy band structure of the fabricated devices reveals a concordant alignment of energy levels, as illustrated in Figure 21a. The matching of conduction band maxima (CBM) of TiO_2 and MAPbI_3 suggests good alignment in energy levels^{224,225}. A barrier height of 1 eV is established between FTO and the TiO_2 layers, facilitating efficient electron collection onto the FTO electrode. Additionally, there's a barrier height difference of approximately 0.38 eV between the valence band maxima (VBM) in Ni_2O_3 and MAPbI_3 , promoting swift hole sliding onto the Ni_2O_3 layer²²⁶. The work function (WF) of the FTO electrodes, about 0.12 eV higher than the VBM of Ni_2O_3 , facilitates efficient hole collection at this junction. These variations in Schottky barrier heights explain the observed asymmetry in the device characteristics depicted in Figures 22, 23, 24, and 25, indicating efficient electron and hole transfer between the interfaces of perovskite, transport materials, and the FTO.

Figure 21b provides a schematic representation of the proposed radiative and non-radiative mechanisms in undoped and Li-doped MAPbI_3 material. In undoped MAPbI_3 films, photoelectrons may undergo radiative recombination or become trapped by defective bands within the bandgap, leading to non-radiative pathways. In Li-doped films, the presence of Li^+ within the MAPbI_3 lattice prevents photoelectrons' entrapment by trap states, promoting the radiative pathway and resulting in increased photoluminescence emissions. These insights contribute to a

comprehensive understanding of the charge transfer mechanisms and energy level alignments critical for the enhanced performance of photodetection devices.

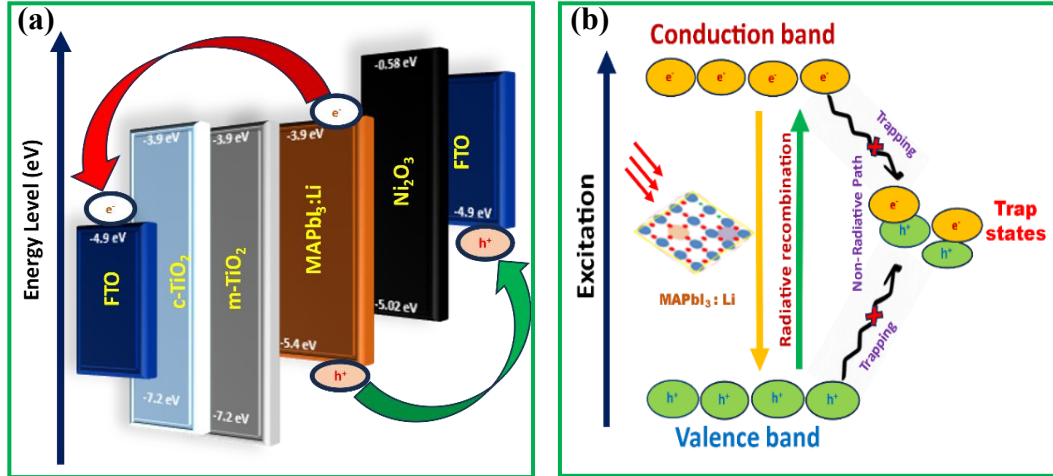


Figure 21: (a) Energy band structure alignment showing charge transfer mechanisms; (b) Proposed radiative and non-radiative recombination mechanisms.

4.2 Current-Voltage (I-V) Characteristics Assessment of the Fabricated Photodetectors

This study was conducted in two ways. First, we systematically investigated the effects of LiI incorporation into MAPbI₃ and evaluated the performance of an optimized vertical structure photodetector with FTO upper and lower electrodes. Secondly, we explored the role of configuration engineering of single and tandem absorber layers based on Li-doped MAPbI₃ perovskite material. Both studies involved photodetectors (PDs) fabricated with dual-face capabilities.

4.2.1 I-V Characteristics Analysis of PDs Fabricated with Different LiI Concentrations

Notably, the fabricated devices exhibit hybrid current-voltage (I-V) characteristics (Figures 22 and 23), combining the attributes of a back-to-back symmetric Schottky behavior, indicative of photodiode characteristics, with an asymmetric Ohmic-like behavior, which is suggestive of photoconductor characteristics. This observed asymmetry as clearly shown in the I-V characteristics of all the fabricated devices can likely be ascribed to variations in barrier heights across distinct junctions within the devices as explained in the previous section. All the photodetectors produced in this study exhibit consistently low dark currents, conforming to typical photodiode behavior²²⁵. Notably, due to variations in barrier heights (Figure 21a), higher photocurrents are observed under reverse bias conditions for the photodetectors in this research. This observation supports the idea that although photodetectors function effectively under both forward and reverse bias conditions, the optimal operating region for photodetectors lies within the third quadrant^{225,227}, as shown in Figures 22 and 23. Furthermore, in all instances, the magnitude of the photocurrent escalates with increasing incident light power, aligning with the expected behavior of conventional photodetectors²²⁷. MAPbI₃ can be characterized as a mixed electronic-ionic semiconductor^{225,228}. This means in addition to conducting through the mobility of electrons and holes, MAPbI₃ also conducts via ions (specifically CH₃NH₃⁺, Pb²⁺, and I⁻ ions). Consequently, at low external bias voltages, the movement of CH₃NH₃⁺, Pb²⁺, and I⁻ ions within MAPbI₃ and Li⁺ and I⁻ from LiI can hinder electronic conduction. The reason behind this is that these ions have lower mobility compared to electrons and holes, primarily due to the higher mass

density. Therefore, these ions introduce additional resistance to the flow of electrons and holes. This explains why lower photocurrent is observed at lower voltages compared to higher voltages. Another phenomenon that contributes to the conduction of charge carriers (electron and holes) in MAPbI₃ and profoundly influences the performance of photodetectors is the presence of ionic space charge effects, stemming from the accumulation of ions at the interfaces, due to absorption, particularly near the junctions between the MAPbI₃ layer and the charge-selective layers such as TiO₂ or Ni₂O₃. These effects give rise to high electric fields at the interfaces, facilitating the efficient dissociation and transport of photogenerated charge carriers within the device. This phenomenon enhances charge carrier extraction and collection, reducing the likelihood of carrier recombination before reaching the electrodes. Consequently, the photodetector exhibits improved characteristics such as enhanced photocurrent, responsivity, detectivity, and response speed, crucial for its practical applications.

The impact of LiI addition on the I-V characteristics of the fabricated devices is evident in Figures 22 and 23, showing a notable enhancement in photocurrent as we systematically increased the concentration of LiI from 0 mol% to 10 mol%. This enhancement is apparent as the photocurrent steadily transitions from micro-amperes (in PD0, PD2, and PD5) to milli-amperes (in PD7 and PD10). The observed improvement can be attributed to the introduction of additional charge carriers, specifically holes, into the material. This increase in the carrier concentration (n) and the enhancement of carrier mobility (μ) lead to a reduction in defects and scattering centers within the crystal lattice. Consequently, the electrical conductivity of the doped MAPbI₃ material is greatly improved, resulting in a more current-voltage relationship in the fabricated devices. This can be

elucidated using fundamental semiconductor physics where the electrical conductivity (σ) of a semiconductor can be quantified by the equation:

$$\sigma = q\mu n \quad (4.1)$$

This dual effect results in a substantial improvement in the material's electrical conductivity, making it a more efficient conductor of electricity. Consequently, the I-V characteristics of the doped MAPbI₃ devices show enhanced performance due to these changes in electrical properties. As depicted in all the images in Figures 21 and 22, the photocurrent exhibits distinct jumps under varying light intensities. For instance, when exposed to 3.5 mW/cm² of solar radiation, the fabricated devices display a minimum photocurrent of approximately -7.5 μ A (in PD0), which then increases to about -10.5 mA for both the NF- and NN-faces due to enhanced carrier generation, which is a highly advantageous feature for photodiodes. In contrast, the dark current consistently rises from PD0 to PD10 as expected, owing to the increased thermally generated carriers, which is undesirable behavior, as high dark current leads to lower device performance. The slightly elevated photocurrent observed in NF-faces compared to NN-faces can be attributed to the superior mobility of anions, specifically electrons, in contrast to cations like holes. This disparity arises from the lower density of anions. Furthermore, the prevalence of less dense I⁻ ions as the primary ionic carriers in MAPbI₃, given their remarkably low activation energy of 0.58 eV²²⁹ in comparison to the respective 2.31 eV²²⁹ and 0.84 eV²²⁹ activation energies of Pb²⁺ and CH₃NH₃⁺, contributes to the phenomenon. As a result, negative ions flow more rapidly toward the NF-faces than the NN-faces, elucidating the generation of higher photocurrent in the NF-faces of the devices.

These differences in photocurrent values among the device faces underscore the rationale for characterizing our devices as bifacial photodetectors.

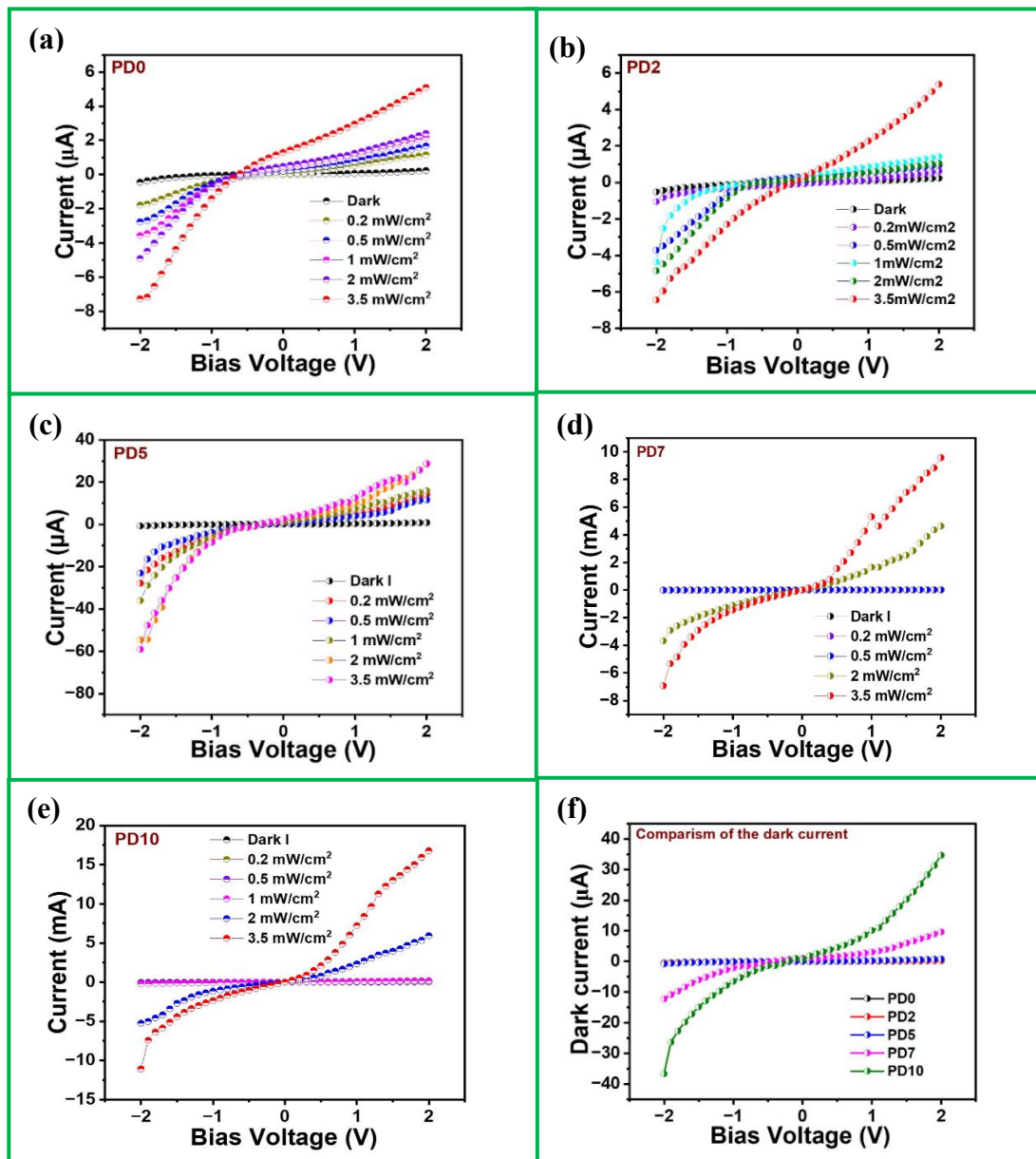


Figure 22: Current-voltage (i-v) characteristics for the NF-faces of the fabricated photodetectors: (a) PD0 (0 mol% LiI) (b) PD2 (2 mol% LiI) (c) PD5 (5 mol% LiI) (d) PD7 (7 mol% LiI) (e) PD10 (10 mol% LiI), and (f) Comparison between the measured dark current.

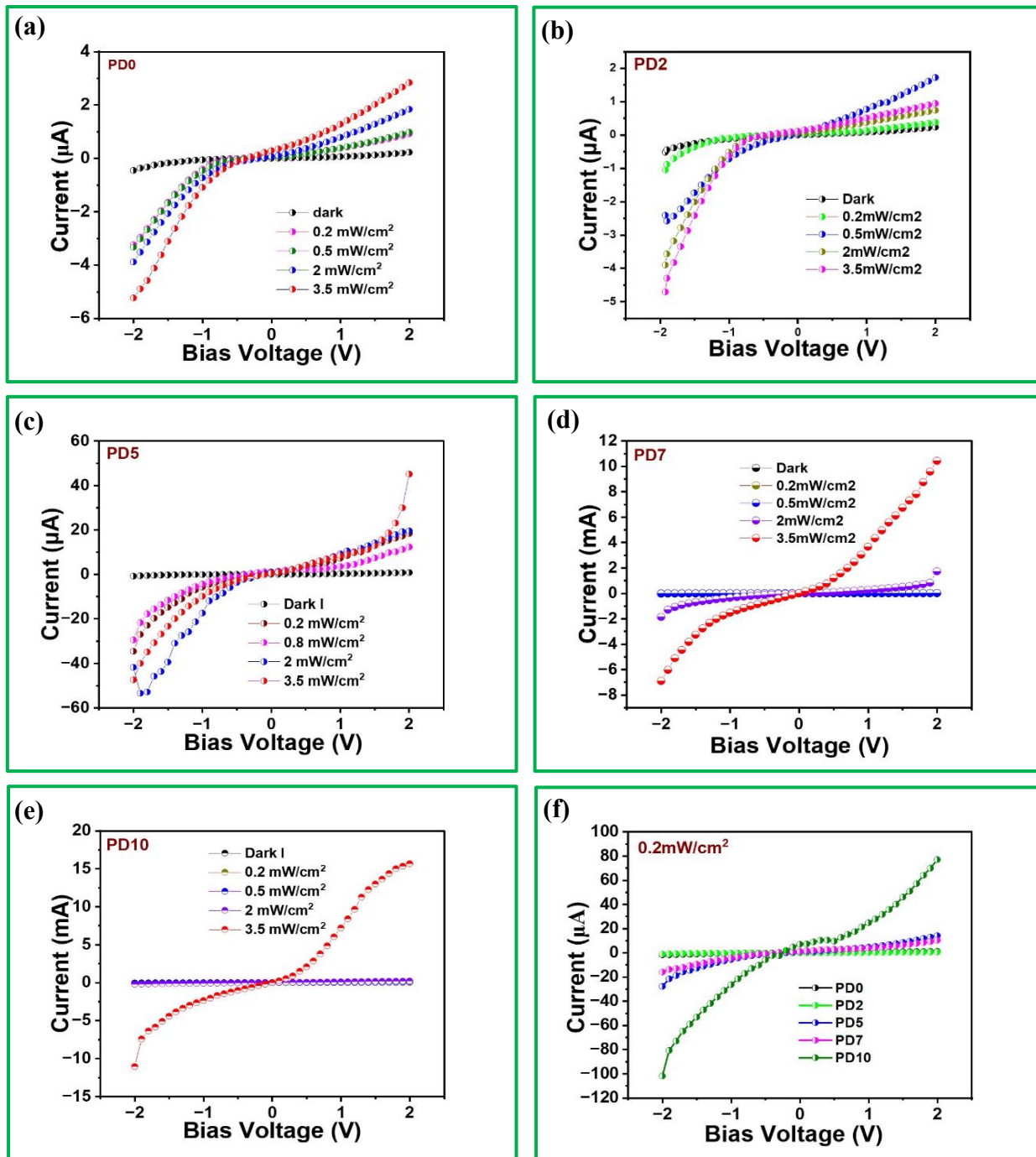


Figure 23: Current-voltage characteristics for the NN-faces of the fabricated photodetectors: (a) PD0 (0 mol% LiI) (b) PD2 (2 mol% LiI) (c) PD5 (5 mol% LiI) (d) PD7 (7 mol% LiI) (e) PD10

(10 mol% LiI), and (f) Comparison between the measured photocurrent under 0.2 mW/cm² illumination.

4.2.2 I-V Characteristics Analysis of PDs Fabricated with Single- and Double-Absorber Layer Configurations

The PDs fabricated with single and tandem (double) MAPbI₃ absorber layers based on T, N, and NN-faces have been systematically code-named for clarity in referencing (Figure 12a-d). PD0-A, PD0-B, PD5-A, and PD5-B represent devices with and without LiI additives and different absorber layer configurations (Figure 11a-d). Specifically, PD0-A is constructed with a single layer of absorber material containing 0 mol% LiI, PD0-B has a double absorber layer with 0 mol% LiI, PD5-A features a single layer with 5 mol% LiI, and PD5-B incorporates a double absorber layer with 5 mol% LiI. The face designations include T-faces for all photodetectors based on the architecture FTO/c-TiO₂/m-TiO₂/MAPbI₃ for PD0-A and PD0-B and FTO/c-TiO₂/m-TiO₂/MAPbI₃-Li for PD5-A and PD5-B. Additionally, PD0-A and PD5-A have N-faces based on FTO/Ni₂O₃, while PD0-B and PD5-B have NN-faces based on FTO/Ni₂O₃/MAPbI₃ and FTO/Ni₂O₃/MAPbI₃-Li, respectively. The complete architectures of the fabricated devices are shown in Figure 12.

The PDs produced in this study exhibit distinct current-voltage (I-V) characteristics, as depicted in Figures 22 and 23. All PDs in this study consistently demonstrate low dark currents, aligning with typical photodiode behavior²²⁵.

The comparative analysis between the PDs fabricated with a single MAPbI₃ absorber layer (PD0-A and PD5-A) and those with a double absorber layer (PD0-B and PD5-B) reveals intriguing

insights into the influence of the absorber layer configuration on the I-V characteristics. Particularly, the photodetector with a single MAPbI₃ absorber layer exhibits superior I-V characteristics compared to its double-layered counterpart. This superiority of PDs with single-layer absorbers over those with double-layer absorbers in terms of current-voltage (I-V) characteristics can be attributed to several factors:

- **Reduced Interfacial Resistance:** Single-layer absorbers typically have fewer interfaces between different materials compared to double-layer absorbers. The total resistance in a photodetector can be represented by the sum of the series resistance (R_s) and the shunt resistance (R_{sh}). The R_s contributes to the voltage drop across the device and can be expressed as $R_s = (\rho/A) \times L$ where: ρ is the resistivity of the material, A is the cross-sectional area through which current flows, and L is the thickness of the material. PDs with single-layer absorbers typically have lower series resistance due to their simplified device structure and reduced number of interfaces, resulting in improved charge transport and less voltage drop across the device under bias conditions.
- **Enhanced Charge Carrier Transport:** Single-layer absorbers often exhibit a more uniform and continuous morphology, which can facilitate efficient charge carrier transport within the device. The transport of charge carriers within the photodetector depends on factors such as mobility (μ) and carrier lifetime (τ). In semiconductor devices like PDs, the mobility-lifetime product ($\mu \cdot \tau$) is a crucial parameter. Higher values of $\mu \cdot \tau$ lead to more efficient charge transport and collection, resulting in better device performance. In devices with single-layer absorbers,

charge carriers experience fewer interfacial obstacles, leading to improved transport properties and reduced recombination losses, leading to improved i-v characteristics.

- ***Improved Charge Collection Efficiency:*** The simplified structure of single-layer absorbers may lead to more efficient charge collection at the electrodes, reducing losses associated with charge recombination and trapping. This can result in higher photocurrent and a more linear response in the I-V characteristics, particularly under varying illumination conditions. Overall, the superior I-V characteristics observed in PDs with single-layer absorbers are often attributed to the optimized charge transport, reduced interface resistance, and improved charge collection efficiency afforded by the simplified device.

Summarily, the synergistic effect of LiI doping and the single absorber layer configuration results in improved current-voltage characteristics, emphasizing the significance of engineering strategies in tailoring the functionality of perovskite-based devices.

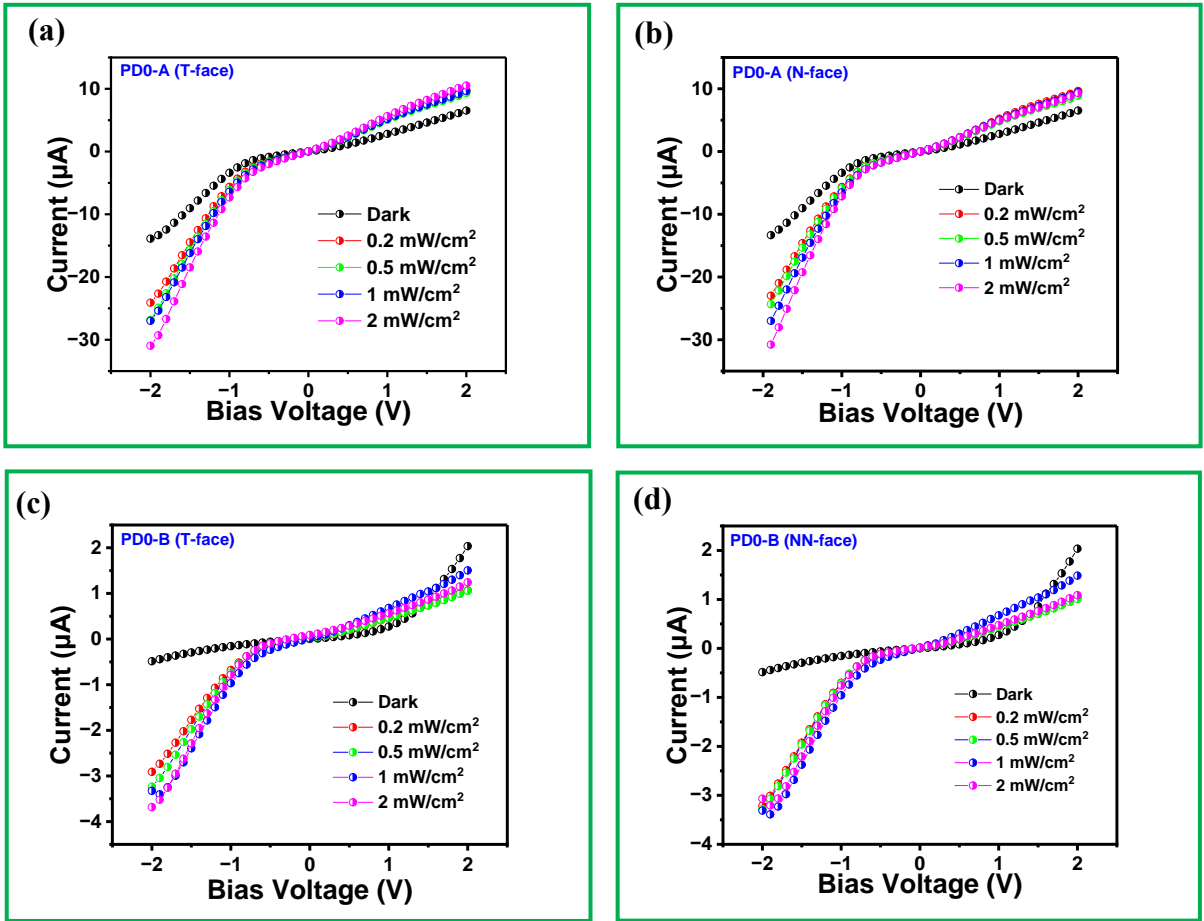


Figure 24: Current-voltage (i-v) characteristics for the PDOs of the fabricated photodetectors: (a) PD0-A (T-face), (b) PD0-A (N-face), (c) PD-B (T-face), and (d) PD0-B (NN-face).

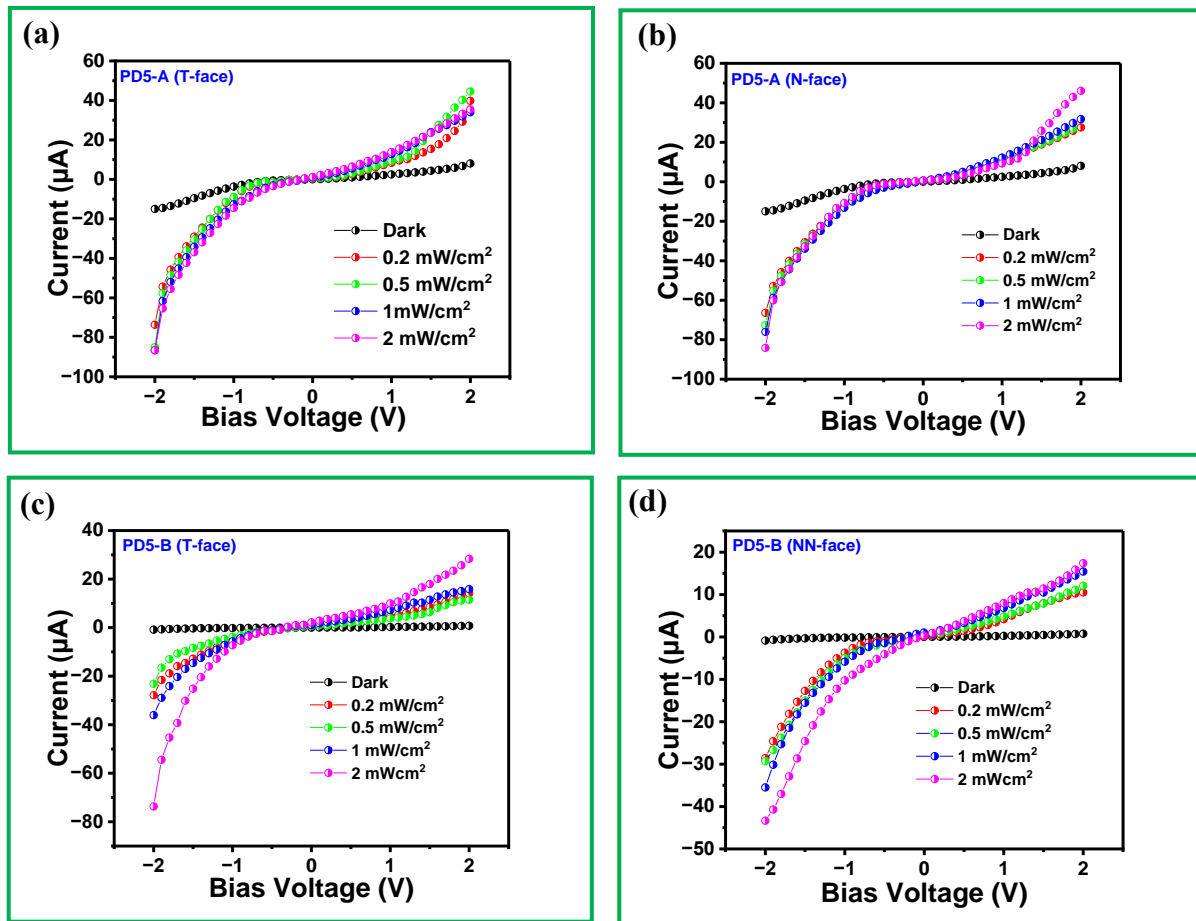


Figure 25: Current-voltage (i-v) characteristics for the fabricated PD5s: (a) PD5-A (T-face), (b) PD5-A (N-face), (c) PD5-B (T-face), and (d) PD5-B (NN-face).

4.3 Photodetector Figures of Merit

The performance metrics, otherwise called figures of merit for the PDs, such as external quantum efficiency (EQE), responsivity (R), detectivity (D^*), linear dynamic range (LDR), and transient photoresponse play crucial roles in assessing their performance.

4.3.1 Figures of Merit of PDs Fabricated with Different LiI Molar Concentrations

EQE, which gives the ratio of collected charge carriers to the incident photons was calculated using equation (2.9) at 550 nm which is the wavelength the material shows maximum absorbance. This is similar to the method reported by Hu, X. *et al*²³⁰ and Liu M. *et al*²³¹. The Responsivity, a key indicator of photocurrent generation efficiency, is calculated using equation (2.8), where I_{ph} represents photocurrent magnitude, I_{dk} denotes dark current magnitude, and P_{hv} signifies incident light power. With incident light intensity of 1.2 mW/cm², a bias voltage of 2V, and at standard laboratory conditions, the estimated maximum responsivity values for NF-faces of PD0, PD2, PD5, PD7, and PD10 are 0.34, 0.56, 366, 117.41, and 34.57 mA/W, respectively, and for NN-faces are 0.06, 0.43, 10.17, 19.93, and 16.96 mA/W, respectively. Consequently, PDs following the PD5 architecture exhibit superior photon-to-current conversion efficiencies compared to the other fabricated devices. The exceptional electrical performance of PD5 can be attributed to multiple factors, including its superior film coverage and crystallinity, heightened light-absorbing capabilities, and decreased trap states which reduce non-radiative recombination. This combination of features contributes to its outstanding performance. The responsivity values achieved in this study surpass or are in a similar order to the values reported for perovskite photodetectors employing both vertical^{232–236} and lateral^{237–241} designs.

$$D^* = \frac{R\sqrt{A}}{\sqrt{2eI_{dk}}} \quad (4.1)$$

$$LDR = 20 \log \left[\frac{I_{ph}}{I_{dk}} \right] \quad (4.2)$$

The measure of photodetector performance concerning noise, known as detectivity, can be calculated using equation (4.1), where A represents the active areas of the photodetector and e is the magnitude of the electronic charge. If shot noise predominantly contributes to the total noise current in photodiodes, then equation (4.1) is applicable. In cases where other noise sources, like thermal noise, have a significant influence, further adjustments are necessary. Based on equation (4.1), the maximum detectivity values estimated for PD0, PD2, PD5, PD7, and PD10 are 2.931×10^{10} , 0.21×10^{10} , 14.98×10^{10} , 11.02×10^{10} , and 2.08×10^{10} jones for NF-faces, and 0.51×10^{10} , 0.16×10^{10} , 0.42×10^{10} , 1.87×10^{10} , and 1.02×10^{10} jones for NN-faces respectively. These values are in a similar order to the detectivity values of perovskite photodiodes found in the literature, whether they are based on vertical^{227,232,236,242} or lateral²³⁸⁻²⁴¹ designs. Similarly, LDR, which is a measure of the span between the smallest and largest detectable signals a system can handle while maintaining a linear response was also calculated based on equation (4.2), and the values are given in Table 3.

The transient photoresponse behavior of the fabricated PDs is illustrated through current-time (i-t) curves depicted in Figure 26 a-f. These curves demonstrate consistent and repeatable on/off switching behavior under a 10-mW helium-neon laser, confirming the reliability of the fabricated devices. In photodetection, the response time (τ) is a crucial parameter that indicates the time required for the output current to stabilize when exposed to light or after light removal. This time

characteristic includes both the rise or response time (τ_r) and the fall or decay time (τ_f). The rise time signifies the duration for the photocurrent to increase from 10% to 90%, representing the transition from a low to a high current state ("ON" condition). Conversely, the fall time indicates the time for the photocurrent to decrease from 90% to 10%, illustrating the quick return to a baseline current state after light cessation ("OFF" condition). These parameters are vital for optimizing photodetector designs for applications that demand fast responses, such as imaging or communication systems. The estimated rise and fall times parameters are given in Table 3.

Table 3: Figures of merit for the fabricated photodetectors in this work.

Device Code	Quantum Efficiency (%)		Responsivity (mA/W)		Detectivity (Jones)		Linear Dynamic Range (dB)		Rise/Fall Times (ms)	
	NF-face	NN-face	NF-face	NN-face	NF-face	NN-face	NF-face	NN-face	NF-face	NN-face
PD0	0.14	0.099	0.63	0.44	2.93×10^{10}	0.51×10^{10}	59.67	44.48	389/372	349/354
PD2	0.13	0.097	0.56	0.43	0.2×10^{10}	0.16×10^{10}	12.71	11.21	620/1307	542/901
PD5	82.67	2.23	366	10.17	14.98×10^{10}	0.42×10^{10}	20.68	2.09	509/619	522/603
PD7	26.52	4.50	117.41	19.93	11.07×10^{10}	1.87×10^{10}	32.19	17.77	703/685	454/792
PD10	7.81	3.83	34.57	16.96	2.08×10^{10}	1.02×10^{10}	15.27	10.51	1182/1031	1258/1281

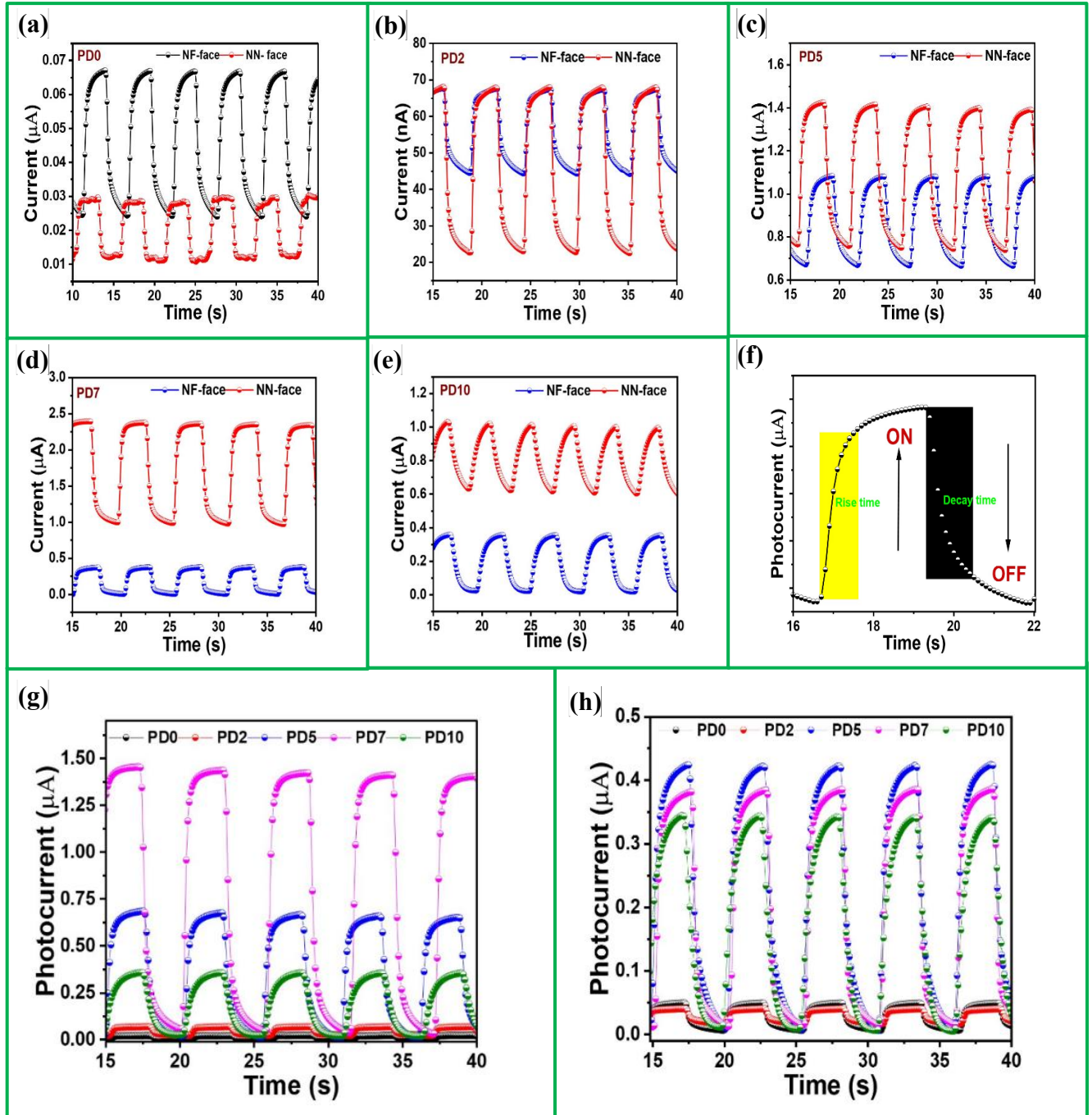


Figure 26: (a-e) Transient photoresponse of the photodetectors corresponding to optical switching conditions. (f) Estimation of Rise and Fall times during light ON and OFF times. (g) combined i-t curves for NF-faces, and (h) combined i-t curves for the NN-faces.

4.3.2 Figures of Merit of PDs with Single and Double-Absorber Layer Configurations

Under standard laboratory conditions with an incident light intensity of 1.2 mW/cm² and a bias of 2V, the estimated maximum responsivities for T-faces of PD0-A, PD0-B, PD5-A, and PD5-B are 8.89, 0.63, 512.58 and 366 mA/W, respectively. For N-faces of PD0-A and PD5-A, the values are 5.86 and 8.25mA/W, respectively, and for NN-faces of PD0-B and PD5-B, the values are 0.44 and 10.17 mA/W, respectively. The values of EQE for each of these devices was also computed using equation (2.9) in similar method cited above and are given in Table 4. The performance of the PDs against noise is assessed in terms of detectivity (D^*), calculated using equation (4.1), The maximum detectivities estimated for T-faces of PD0-A, PD0-B, PD5-A, and PD5-B are 1.04×10^{10} , 0.15×10^{10} , 5.06×10^{11} , and 1.5×10^{11} Jones, respectively. For N-faces of PD0-A and PD5-A, the values are 0.67×10^{10} and 0.84×10^{10} Jones, respectively, and for NN-faces of PD0-B and PD5-B, the values are 0.11×10^{10} and 0.42×10^{10} Jones, respectively. These detectivity values align with those reported for perovskite photodiodes in the literature, irrespective of the design, whether vertical^{211,232,236,242} or lateral^{238,240–243}. The calculated LDR values are presented in Table 4.

The transient photoresponse behavior of the fabricated PDs is illustrated through current-time (i-t) curves depicted in Figure 27a-f. These curves demonstrate consistent and repeatable on/off switching behavior under a 10-mW helium-neon laser, confirming the reliability of the fabricated devices. These parameters are vital for optimizing photodetector designs for applications that demand fast responses, such as imaging or communication systems. The estimated rise and fall times are detailed in Table 4.

Notably, PD5-A exhibits superior photon-to-current conversion efficiency, linearity, and fast response time compared to other fabricated PDs, attributed to its simpler structure (reduced number of interfaces), and enhanced light-absorbing capabilities which stem from superior film coverage, crystallinity, and reduced trap states, minimizing non-radiative recombination. These exceptional features contribute to its outstanding performance, surpassing or aligning with reported values for perovskite PDs employing various designs.

Table 4: Figures of merit for the fabricated photodetectors in this work

Device Architecture	Face Designation	Quantum Efficiency (%)	Responsivity (mA/W)	Detectivity (Jones)	Linear Dynamic Range (dB)	Rise/Fall Times (ms)
PD0-A	T-face	2.01	8.89	1.04×10^{10}	13.79	463/462
PD0-A	N-face	1.32	5.86	0.67×10^{10}	12.21	452/438
PD0-B	T-face	0.14	0.63	2.93×10^{10}	59.67	389/372
PD0-B	NN-face	0.099	0.44	0.51×10^{10}	44.48	349/354
PD5-A	T-face	115.78	512.58	5.06×10^{11}	45.72	179/154
PD5-A	N-face	1.86	8.25	0.84×10^{10}	12.78	167/197
PD5-B	T-face	82.67	366	1.5×10^{11}	20.68	509/619
PD5-B	NN-face	2.23	10.17	0.42×10^{10}	2.09	522/603

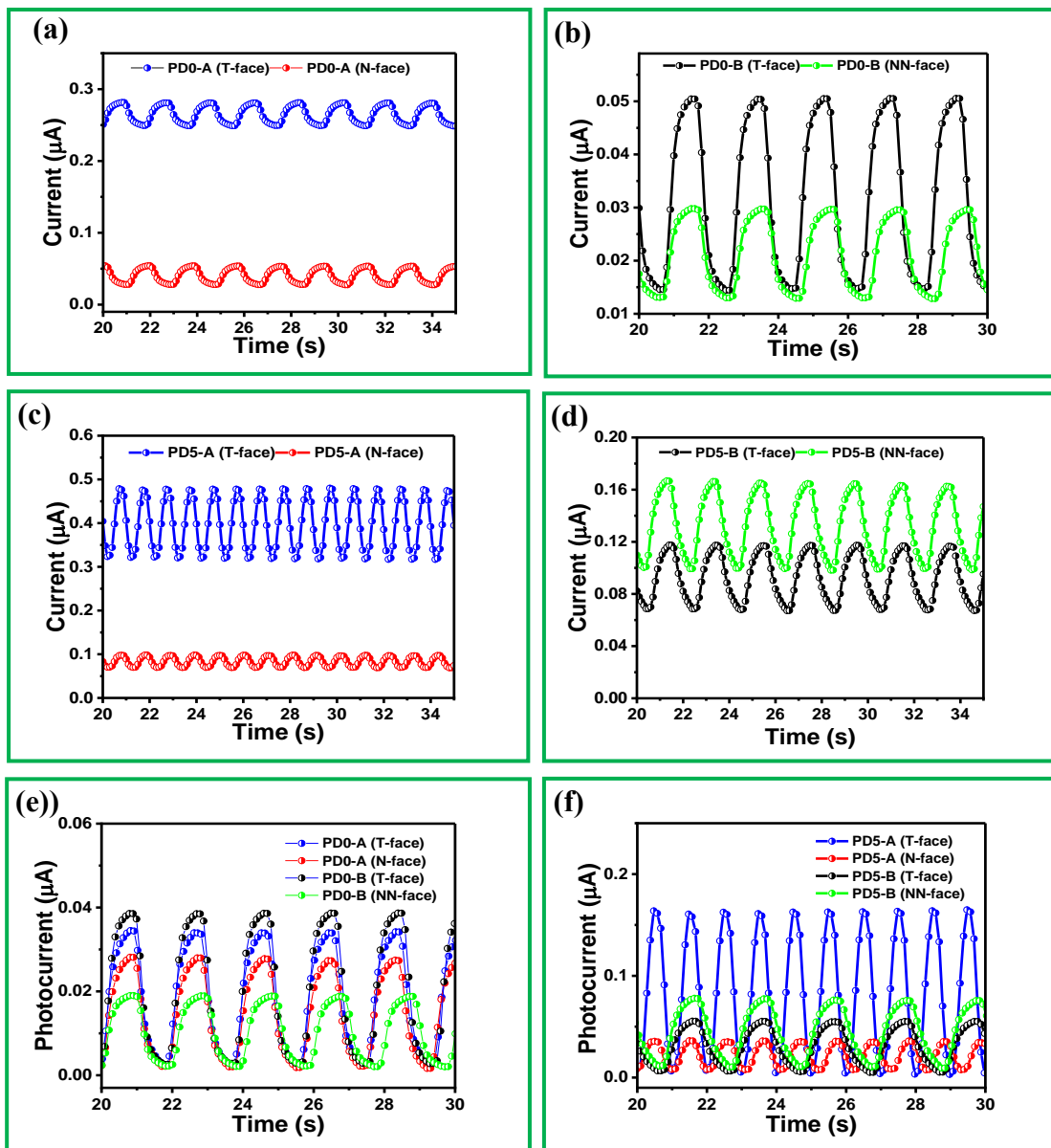


Figure 27: (a-d) Transient photoresponse (i-t curves) for the fabricated PDs; (e-f) combined normalized i-t curves for the faces of the fabricated PDs.

4.4 Performance Evaluations of This Work

The performance of photodetectors, as indicated by parameters such as external quantum efficiency, responsivity, detectivity, linear dynamic range, and response times, varies significantly across different configurations. Among the configurations analyzed, PD5 consistently emerges as the most promising option, showcasing remarkable quantum efficiency, responsivity, and detectivity, especially in configurations with T-face architecture. This superior performance positions PD5 as an ideal choice for applications demanding high sensitivity and the detection of weak optical signals. The exceptionally high responsivity and detectivity observed in PD5-A with T-face (512.58 mA/W and $5.06 \times 10^{11} \text{ Jones}$, respectively) underscore its potential for critical applications where signal detection at low light levels is paramount. In contrast, the PD0 configurations, with 0mol% LiI concentration and NF-face designations, offer moderately high performance across some parameters. Notably, the NF-face configurations of PD0 exhibit a broader linear dynamic range, suggesting their suitability for applications requiring the detection of a wide range of optical power levels with high precision. However, despite their competitive performance, PD0 configurations generally fall short of the exceptional sensitivity and detectivity achieved by PD5. PD2 exhibits the poorest performance among the photodetectors, attributed to various factors such as suboptimal LiI concentration, incomplete doping, inadequate material morphology and quality. These factors collectively contribute to reduced EQE for PD2, highlighting the importance of optimizing doping levels, enhancing material quality, and engineering interfaces to improve photodetector performance. PD7 configurations display competitive performance, particularly in responsivity and detectivity, especially for NF-face

designs. While exhibiting promising characteristics, such as high responsivity and detectivity, PD7 device faced limitations in terms of linear dynamic range and response times compared to PD5 configurations. Thus, while suitable for certain applications requiring high sensitivity, PD7 may not offer the same level of performance across all parameters as PD5. PD10 configurations present moderate performance across all parameters analyzed, indicating a balanced performance profile suitable for applications where a compromise between sensitivity, dynamic range, and response time is acceptable. This moderate performance makes PD10 configurations versatile and applicable across a wide range of optical sensing and detection applications, where achieving a balance between various performance metrics is essential.

Summarily, the selection of the optimal photodetector configuration should be guided by the specific requirements of the intended application. While PD5 configurations excel in sensitivity and detectivity, PD0, PD7, and PD10 offer varying degrees of performance across different parameters, catering to a spectrum of application needs. Further research and optimization efforts are necessary to enhance the performance and applicability of these photodetectors, ultimately driving advancements in optical sensing and detection technologies.

4.5 Comparison with the Existing Literature

Comparing this work with the literature, several key aspects such as material composition, cost, stability, and performance metrics can be analyzed to assess the relative merits and potential areas for improvement in our photodetector configurations. Table 5 presents the metrics of some perovskite-based photodetectors in the literature.

This work utilizes $\text{CH}_3\text{NH}_3\text{PbI}_3$ (Perovskite) as the active material in conjunction with LiI for doping. The literature presents a variety of materials, incorporated into the device constructions, including Si, TiO_2 , Al_2O_3 , PCBM, Spiro-OMeTAD, ZnO, Ag, and Au, among others. Notably, the use of Perovskite-based materials is common in both our work and literature, underscoring the material's significance and versatility in photodetector applications. The choice of materials in this work appears to be well-aligned with current trends in photodetector research, emphasizing the potential of Perovskite-based materials for high-performance photodetectors. While specific cost data are not provided in the tables, it is generally understood that the fabrication of Perovskite-based devices, including the use of $\text{CH}_3\text{NH}_3\text{PbI}_3$, can be relatively cost-effective compared to traditional semiconductor materials like Si. The choice of material composition in our photodetector configurations, particularly the use of MAPbI_3 , TiO_2 , Ni_2O_3 , and FTO as the active material, ETL, HTL, and electrodes respectively, aligns well with cost-effective materials selection strategies. By prioritizing cost-efficient materials without compromising on performance, our work demonstrates a practical approach to developing high-performance photodetectors that are economically viable. Spiro-OMeTAD, often used as a hole transport material (HTM) in Perovskite solar cells and photodetectors, is known to be relatively expensive. Additionally, noble metals such as gold and silver, frequently used as electrode materials due to their excellent conductivity and stability, further contribute to the overall cost of the device. In contrast, the materials used in this work are more cost-effective and abundantly available, making our work an attractive choice for applications where cost efficiency is a significant consideration, compared to devices

incorporating Spiro-OMeTAD, gold, and silver. This cost advantage can be particularly beneficial for large-scale manufacturing and commercialization of photodetector devices.

Furthermore, while specific stability data are not provided herein, the literature offer an insight on a range of stability performance across various materials and device architectures. Some devices in literature, despite achieving high performance in responsivity and detectivity, may suffer from stability issues due to the inherent properties of the materials used or the device fabrication processes employed. In contrast, this work, incorporating LiI as a dopant in Perovskite-based materials, may offer improved stability compared to some devices in literature relying solely on Perovskite materials or less stable components like Spiro-OMeTAD and PEDOT: PSS. Enhancing the stability of photodetectors is essential for their practical applications, especially in environments where the devices may be exposed to varying conditions, including humidity, temperature fluctuations, and mechanical stress. Our work's emphasis on stability, as evidenced by the incorporation of LiI dopant, aligns with the industry's focus on developing robust and reliable photodetectors suitable for real-world applications. However, comprehensive stability tests under relevant operating conditions are necessary to validate and quantify the stability improvements achieved by our photodetector configurations compared to literature examples.

Comparing the performance metrics of your photodetector configurations with devices in the existing literature reveals several noteworthy observations. In terms of responsivity (R), our configurations exhibit competitive values, with PD5 configurations demonstrating a responsivity of 512.58 mA/W and 366 mA/W for T-faces. These values compare favorably with literature

examples provided in Table 5, indicating the superior sensitivity of your configurations. Similarly, in detectivity (D), the configurations, particularly PD5 with T-face, exhibit remarkable values, with detectivities reaching up to 5.06×10^{11} Jones. This surpasses the detectivity values reported for many devices in the existing literature, highlighting the superior sensitivity and signal detection capabilities of your photodetector configurations.

Furthermore, the configurations in this work demonstrate rapid response times, particularly in PD5 with T-face, with rise/fall times of 179/154 ms and 167/197 ms for T-face and NN-face, respectively. Although some literature examples, such as FTO/TiO₂/Al₂O₃/PCBM/CH₃NH₃PbI₃/Spiro-OMeTAD/Au/Ag, reported extremely fast response times 1.2/3.2 μ s²⁴³, the response times of our configurations are competitive and indicate their suitability for applications requiring rapid signal detection and processing.

Table 5: Figures of merit from existing literature.

MATERIAL	R (A/W)	D (Jones)	R/F time	REF
FTO/c-TiO ₂ /m-TiO ₂ /MAPbI ₃ :(Li)/Ni ₂ O ₃ /FTO	0.513	5.06 x 10 ¹¹	179/154 ms	This work
FTO/c-TiO ₂ /m-TiO ₂ /MAPbI ₃ /MAPbI ₃ : (Li)/Ni ₂ O ₃ /FTO	0.366	1.5 x 10 ¹¹	167/197 ms	This work
Si/SiO ₂ /IGZO/CH ₃ NH ₃ PbI ₃ /Mo/PMMA	0.025	9.5 × 10 ⁹	40/100 ms	²⁴⁴
FTO/TiO ₂ /Al ₂ O ₃ /PCBM/CH ₃ NH ₃ PbI ₃ /Spiro- OMeTAD/Au/Ag	0.4	10 ¹²	1.2/3.2 μs	²⁴⁵
FTO/TiO ₂ /MAPbI ₃ /Spiro-OMeTAD/Au	1.0	-	17/20 μs	²⁴⁶
FTO/PEDOT:PSS+Ag NPs/CH ₃ NH ₃ PbI ₃ /Al	0.25	1.53 × 10 ¹¹	110/72 ms	²⁴⁷
CsPbBr ₃ –Cs ₄ PbBr ₆ /FTO/TiO ₂ /CH ₃ NH ₃ PbI ₃ /Spiro- OMeTAD/Ag	0.004	1.2 × 10 ¹²	7.8/33.6 μs	²⁴⁸
Si/SiO ₂ /CsPbBr ₃ /Au	0.034	7.5 × 10 ¹²	0.6/0.9 ms	²⁴⁹
FTO/TiO ₂ /CH ₃ NH ₃ PbI ₃ /FTO	0.00049	6.1 × 10 ¹⁰	20/20 ms	²⁵⁰
Au/NCs/Au	0.01	4.56 × 10 ⁸	0.2/1.2 ms	²⁵¹
FTO/ZnO/CsPbBr ₃ /MoO ₃ /Au	0.3	1.15 × 10 ¹³	200/500 ms	²⁵²

CHAPTER 5

CONCLUSIONS

In conclusion, our systematic exploration of lithium iodide (LiI) incorporation into solution processed MAPbI₃ for enhanced photodetection applications has provided valuable insights. Contrary to the traditional roles of alkali metals as surface passivation, our study reveals that lithium doping in MAPbI₃ acts as an effective n-type dopant, entering the lattice and suppressing photocarrier trapping and facilitating more efficient extraction of charge carriers, allowing for enhanced radiative recombination processes as corroborated by photoluminescence measurement. This doping strategy not only enhances perovskite material crystallinity but also improves light absorption and overall optoelectronic performance in photodetector devices.

The study provides a comprehensive analysis of the influence of LiI doping on the optoelectrical and charge transfer properties of perovskite-based photodetectors (PDs). Our findings reveal that the incorporation of LiI significantly enhances the Ultraviolet-Visible (UV-vis) light absorption and photoluminescence capabilities of the perovskite films without altering their optical bandgaps. This enhancement is attributed to improved film coverage, crystal quality, and reduced trap states, leading to enhanced photoluminescence and charge carrier extraction efficiency.

The morphological and crystalline assessment demonstrates that Li doping introduces structural changes without compromising the integrity of the perovskite lattice. XRD patterns remained consistent, indicating stable crystal structures. Advanced characterization techniques, including

XPS and EDS, confirm the presence of Li ions within the perovskite film, providing valuable insights into the chemical states and locations of lithium atoms in the lattice. The study also emphasizes the impact of LiI on photoelectrical characteristics, revealing a nuanced concentration-dependent effect on light absorption.

Furthermore, our charge transfer and recombination mechanism studies elucidate the efficient movement of electrons and holes within the perovskite material and between the transport materials and electrodes. The alignment of energy levels across the device interfaces, coupled with reduced trap density in LiI-doped films, promotes efficient charge carrier extraction and reduces recombination losses at the interface, contributing to the overall enhanced device performance. The fabricated devices demonstrated promising figures of merit, including high responsivity and detectivity values, underscoring their potential for efficient photodetection applications. Particularly, the PDs with a single MAPbI₃ absorber layer exhibited superior current-voltage characteristics compared to double-layered counterparts, attributed to reduced interface resistance, enhanced charge carrier transport across the interface, and improved charge collection efficiency.

The standout achievement in this research is the champion photodetector, PD5-A, constructed with a single absorber layer which incorporated 5 mol% LiI. PD5 exhibited superior performance metrics, including responsivity, detectivity, and linear dynamic range. With an estimated maximum responsivity of 512.58 mA/W, a detectivity of about 5.06×10^{11} jones, and an excellent linear dynamic range, outperforming other fabricated devices, showcasing the remarkable potentials of lithium doping for advancing the development of efficient and stable perovskite-

based photodetectors. This systematic exploration contributes significantly to the growing body of knowledge on alkali metal doping in perovskite materials, offering a pathway for the optimization of photodetector devices.

These findings collectively emphasize the significance of LiI doping and device engineering strategies in tailoring the functionality and performance of perovskite-based PDs. By offering insights into the intricate relationship between LiI doping, charge transfer mechanisms, and interface properties, this study contributes to the advancement of perovskite-based PDs and paves the way for their broader applications in optoelectronic devices and systems.

Recommendation for Further Studies

For future studies, it is recommended to explore material optimization strategies by investigating alternative dopants, compositional variations, and hybrid Perovskite materials to enhance device performance and stability. Additionally, innovative device architecture designs, including inverted structures or tandem configurations, should be considered to optimize charge transport and minimize recombination losses. Performance enhancement can be achieved by optimizing fabrication processes and integrating nanostructured materials or quantum dots to improve light absorption and charge carrier dynamics. Cost-effective materials selection and sustainability considerations should be prioritized to develop environmentally friendly and economically viable photodetector technologies. Comprehensive stability assessments and advanced encapsulation techniques are essential to validate device reliability and operational lifetime, facilitating their

practical implementation and commercialization in various optical sensing and detection applications.

References

1. Ballif, C., Haug, F. J., Boccard, M., Verlinden, P. J. & Hahn, G. Status and perspectives of crystalline silicon photovoltaics in research and industry. *Nature Reviews Materials* **2022** 7:8 7, 597–616 (2022).
2. Battaglia, C., Cuevas, A. & De Wolf, S. High-efficiency crystalline silicon solar cells: status and perspectives. *Energy Environ Sci* **9**, 1552–1576 (2016).
3. Bati, A. S. R. *et al.* Next-generation applications for integrated perovskite solar cells. *Communications Materials* **2023** 4:1 4, 1–24 (2023).
4. Miyasaka, T., Kulkarni, A., Kim, G. M., Öz, S. & Jena, A. K. Perovskite Solar Cells: Can We Go Organic-Free, Lead-Free, and Dopant-Free? *Adv Energy Mater* **10**, (2020).
5. Mitzi, D. B. Introduction: Perovskites. *Chem Rev* **119**, 3033–3035 (2019).
6. Vidal, R., Alberola-Borràs, J. A., Sánchez-Pantoja, N. & Mora-Seró, I. Comparison of Perovskite Solar Cells with other Photovoltaics Technologies from the Point of View of Life Cycle Assessment. *Advanced Energy and Sustainability Research* **2**, 2000088 (2021).
7. Senno, M. & Tinte, S. Mixed formamidinium-methylammonium lead iodide perovskite from first-principles: hydrogen-bonding impact on the electronic properties. *Physical Chemistry Chemical Physics* **23**, 7376–7385 (2021).
8. Liu, D., Li, Q. & Wu, K. Ethylammonium as an alternative cation for efficient perovskite solar cells from first-principles calculations. *RSC Adv* **9**, 7356–7361 (2019).
9. Tang, Z. K. *et al.* Enhanced optical absorption via cation doping hybrid lead iodine perovskites. *Sci Rep* **7**, (2017).
10. Handley, C. M. *et al.* Dynamic tilting in perovskites. *Acta Crystallogr A Found Adv* **79**, 163–170 (2023).
11. Motta, C., El-Mellouhi, F. & Sanvito, S. Charge carrier mobility in hybrid halide perovskites. *Scientific Reports* **2015** 5:1 5, 1–8 (2015).
12. Liu, T., Tang, W., Luong, S. & Fenwick, O. High charge carrier mobility in solution processed one-dimensional lead halide perovskite single crystals and their application as photodetectors. *Nanoscale* **12**, 9688–9695 (2020).

13. Ou, Q. *et al.* Band structure engineering in metal halide perovskite nanostructures for optoelectronic applications. *Nano Materials Science* **1**, 268–287 (2019).
14. Zhao, Y. & Zhu, K. Charge transport and recombination in perovskite (CH₃NH₃)PbI₃ sensitized TiO₂ Solar Cells. *Journal of Physical Chemistry Letters* **4**, 2880–2884 (2013).
15. Shi, D. *et al.* Solar cells. Low trap-state density and long carrier diffusion in organolead trihalide perovskite single crystals. *Science* **347**, 519–522 (2015).
16. Stranks, S. D. *et al.* Electron-hole diffusion lengths exceeding 1 micrometer in an organometal trihalide perovskite absorber. *Science (1979)* **342**, 341–344 (2013).
17. Dong, Q. *et al.* Electron-hole diffusion lengths > 175 μm in solution-grown CH₃NH₃PbI₃ single crystals. *Science (1979)* **347**, 967–970 (2015).
18. Yan, C. *et al.* Ambipolar-transport wide-bandgap perovskite interlayer for organic photovoltaics with over 18% efficiency. *Matter* **5**, 2238–2250 (2022).
19. Li, F. *et al.* Ambipolar solution-processed hybrid perovskite phototransistors. *Nature Communications 2015 6:1* **6**, 1–8 (2015).
20. He, C. & Liu, X. The rise of halide perovskite semiconductors. *Light: Science & Applications 2023 12:1* **12**, 1–2 (2023).
21. Shamsi, J., Urban, A. S., Imran, M., De Trizio, L. & Manna, L. Metal Halide Perovskite Nanocrystals: Synthesis, Post-Synthesis Modifications, and Their Optical Properties. *Chem Rev* **119**, 3296–3348 (2019).
22. Heo, S. *et al.* Deep level trapped defect analysis in CH₃NH₃PbI₃ perovskite solar cells by deep level transient spectroscopy. *Energy Environ Sci* **10**, 1128–1133 (2017).
23. Tan, H. *et al.* Efficient and stable solution-processed planar perovskite solar cells via contact passivation. *Science* **355**, 722–726 (2017).
24. Zheng, X. *et al.* Defect passivation in hybrid perovskite solar cells using quaternary ammonium halide anions and cations. *Nature Energy 2017 2:7* **2**, 1–9 (2017).
25. Li, X. *et al.* CsPbX₃ Quantum Dots for Lighting and Displays: Room-Temperature Synthesis, Photoluminescence Superiorities, Underlying Origins and White Light-Emitting Diodes. *Adv Funct Mater* **26**, 2435–2445 (2016).

26. Xing, G. *et al.* Low-temperature solution-processed wavelength-tunable perovskites for lasing. *Nature Materials* 2014 13:5 **13**, 476–480 (2014).
27. Abdi-Jalebi, M. *et al.* Maximizing and stabilizing luminescence from halide perovskites with potassium passivation. *Nature* 2018 555:7697 **555**, 497–501 (2018).
28. Zhao, W. *et al.* Alkali Metal Doping for Improved CH₃NH₃PbI₃ Perovskite Solar Cells. *Advanced Science* **5**, 1700131 (2018).
29. Atourki, L. *et al.* Impact of Li doping on the photophysical properties of perovskite absorber layer FAPbI₃. *J Alloys Compd* **850**, 156696 (2021).
30. Xie, A. *et al.* Lithium-doped two-dimensional perovskite scintillator for wide-range radiation detection. *Communications Materials* 2020 1:1 **1**, 1–10 (2020).
31. Fang, Z., He, H., Gan, L., Li, J. & Ye, Z. Understanding the Role of Lithium Doping in Reducing Nonradiative Loss in Lead Halide Perovskites. *Advanced Science* **5**, 1800736 (2018).
32. Jiang, Q. *et al.* Electrochemical Lithium Doping Induced Property Changes in Halide Perovskite CsPbBr₃ Crystal. *ACS Energy Lett* **3**, 264–269 (2018).
33. Cao, J. *et al.* Interstitial Occupancy by Extrinsic Alkali Cations in Perovskites and Its Impact on Ion Migration. *Advanced Materials* **30**, 1707350 (2018).
34. Zhao, W., Yang, D. & Liu, S. F. Organic–Inorganic Hybrid Perovskite with Controlled Dopant Modification and Application in Photovoltaic Device. *Small* **13**, 1604153 (2017).
35. Dawson, J. A. *et al.* Mechanisms of Lithium Intercalation and Conversion Processes in Organic-Inorganic Halide Perovskites. *ACS Energy Lett* **2**, 1818–1824 (2017).
36. Mabrouk, S. *et al.* Higher efficiency perovskite solar cells using additives of LiI, LiTFSI and BMImI in the PbI₂ precursor. *Sustain Energy Fuels* **1**, 2162–2171 (2017).
37. Jiang, Q. *et al.* Electrochemical Doping of Halide Perovskites with Ion Intercalation. *ACS Nano* **11**, 1073–1079 (2017).
38. Hu, Q., Zheng, W., Lin, R., Xu, Y. & Huang, F. Oxides/graphene heterostructure for deep-ultraviolet photovoltaic photodetector. *Carbon N Y* **147**, 427–433 (2019).

39. Li, P., Shivananju, B. N., Zhang, Y., Li, S. & Bao, Q. High performance photodetector based on 2D CH₃NH₃PbI₃ perovskite nanosheets. *J Phys D Appl Phys* **50**, 094002 (2017).
40. Zhao, H. *et al.* Self-driven visible-near infrared photodetector with vertical CsPbBr₃/PbS quantum dots heterojunction structure. *Nanotechnology* **31**, 035202 (2020).
41. Mei, F. *et al.* Recent progress in perovskite-based photodetectors: the design of materials and structures. <https://doi.org/10.1080/23746149.2019.1592709> **4**, 1592709 (2019).
42. Li, W. *et al.* Chemically diverse and multifunctional hybrid organic–inorganic perovskites. *Nature Reviews Materials* **2017 2:3 2**, 1–18 (2017).
43. Mabate, T. P., Maqunga, N. P., Ntshibongo, S., Maumela, M. & Bingwa, N. Metal oxides and their roles in heterogeneous catalysis: special emphasis on synthesis protocols, intrinsic properties, and their influence in transfer hydrogenation reactions. *SN Applied Sciences* **2023 5:7 5**, 1–25 (2023).
44. Zhang, L. *et al.* Advances in the Application of Perovskite Materials. *Nano-Micro Letters* **2023 15:1 15**, 1–48 (2023).
45. Akkerman, Q. A. & Manna, L. What Defines a Halide Perovskite? *ACS Energy Lett* **5**, 604 (2020).
46. Hirose, K., Sinmyo, R. & Hernlund, J. Perovskite in Earth’s deep interior. *Science* (1979) **358**, 734–738 (2017).
47. Popoola, A., Oloore, L. E. & Popoola, I. K. A Demystified Guide on Fabrication and Characterization of Perovskites-Based Optoelectronic Devices. *Adv Photonics Res* **3**, 2100122 (2022).
48. Mitchell, R. H., Welch, M. D. & Chakhmouradian, A. R. Nomenclature of the perovskite supergroup: A hierarchical system of classification based on crystal structure and composition. *Mineral Mag* **81**, 411–461 (2017).
49. Luo, D., Li, X., Dumont, A., Yu, H. & Lu, Z. H. Recent Progress on Perovskite Surfaces and Interfaces in Optoelectronic Devices. *Adv Mater* **33**, (2021).
50. Li, Jun. & Lunds universitet. Effects of Environment on Charge Recombination in Organo-Metal-Halide Perovskite Observed by Photoluminescence Microscopy and Spectroscopy. (2021).

51. Stoddart, A. Purely organic perovskites. *Nat Rev Mater* **3**, 226 (2018).
52. Zhu, J. *et al.* Perovskite oxides: Preparation, characterizations, and applications in heterogeneous catalysis. *ACS Catal* **4**, 2917–2940 (2014).
53. Ha, S. T., Su, R., Xing, J., Zhang, Q. & Xiong, Q. Metal halide perovskite nanomaterials: synthesis and applications. *Chem Sci* **8**, 2522–2536 (2017).
54. Bystrický, R., Tiwari, S. K., Hutár, P., Vančo, L. & Sýkora, M. Synthesis of Sulfide Perovskites by Sulfurization with Boron Sulfides. *Inorg Chem* **61**, 18823–18827 (2022).
55. Geng, S. & Xiao, Z. Can Nitride Perovskites Provide the Same Superior Optoelectronic Properties as Lead Halide Perovskites? *ACS Energy Lett* **8**, 2051–2057 (2023).
56. Schouwink, P. *et al.* Structure and properties of complex hydride perovskite materials. *Nature Communications* **5**, 1–10 (2014).
57. Schouwink, P. *et al.* Bimetallic Borohydrides in the System $M(\text{BH}_4)_2\text{-KBH}_4$ ($M = \text{Mg}, \text{Mn}$): On the Structural Diversity. *Journal of Physical Chemistry C* **116**, 10829–10840 (2012).
58. (4) (PDF) Flowers, Forests and Fields in Physics. https://www.researchgate.net/publication/267751335_Flowers_Forests_and_Fields_in_Physics/figures?lo=1.
59. Peña, M. A. & Fierro, J. L. G. Chemical structures and performance of perovskite oxides. *Chem Rev* **101**, 1981–2017 (2001).
60. Wang, Y. *et al.* Nanocasted synthesis of mesoporous LaCoO_3 perovskite with extremely high surface area and excellent activity in methane combustion. *Journal of Physical Chemistry C* **112**, 15293–15298 (2008).
61. Sadakane, M., Asanuma, T., Kubo, J. & Ueda, W. Facile procedure to prepare three-dimensionally ordered macroporous (3DOM) perovskite-type mixed metal oxides by colloidal crystal templating method. *Chemistry of Materials* **17**, 3546–3551 (2005).
62. Comparotto, C., Ström, P., Donzel-Gargand, O., Kubart, T. & Scragg, J. J. S. Synthesis of BaZrS_3 Perovskite Thin Films at a Moderate Temperature on Conductive Substrates. *ACS Appl Energy Mater* (2022) doi:10.1021/ACSAEM.2C00704/ASSET/IMAGES/LARGE/AE2C00704_0009.JPEG.

63. Pilania, G. *et al.* Anion order in oxysulfide perovskites: origins and implications. *npj Computational Materials* 2020 6:1 **6**, 1–11 (2020).
64. Peng, H. *et al.* High-performance cadmium sulphide-based planar perovskite solar cell and the cadmium sulphide/perovskite interfaces. *J Photonics Energy* **6**, 022002 (2016).
65. Fu, L. *et al.* Bismuth Telluride Interlayer for All-Inorganic Perovskite Solar Cells with Enhanced Efficiency and Stability. *Solar RRL* **3**, 1900233 (2019).
66. Sarmiento-Pérez, R., Cerqueira, T. F. T., Körbel, S., Botti, S. & Marques, M. A. L. Prediction of Stable Nitride Perovskites. *Chemistry of Materials* **27**, 5957–5963 (2015).
67. Zhang, H. *et al.* Prediction and Synthesis of a Selenide Perovskite for Optoelectronics. *Chemistry of Materials* **35**, 4135 (2022).
68. Hydrogen storage properties of bimetallic borohydrides, $MM'(BH_4)_n$. | Download Table. https://www.researchgate.net/figure/Hydrogen-storage-properties-of-bimetallic-borohydrides-MMBH-4-n_tb11_49609090.
69. He, C. & Liu, X. The rise of halide perovskite semiconductors. *Light: Science & Applications* 2023 12:1 **12**, 1–2 (2023).
70. Huang, Y. T., Kavanagh, S. R., Scanlon, D. O., Walsh, A. & Hoyer, R. L. Z. Perovskite-inspired materials for photovoltaics and beyond—from design to devices. *Nanotechnology* **32**, (2021).
71. Liu, X. K. *et al.* Metal halide perovskites for light-emitting diodes. *Nature Materials* 2020 20:1 **20**, 10–21 (2020).
72. Seok, S. Il & Guo, T. F. Halide perovskite materials and devices. *MRS Bull* **45**, 427–430 (2020).
73. Li, K. *et al.* Electronic structures and elastic properties of a family of metal-free perovskites. *Mater Chem Front* **3**, 1678–1685 (2019).
74. Li, W. *et al.* In situ induced core/shell stabilized hybrid perovskites via gallium (III) acetylacetonate intermediate towards highly efficient and stable solar cells. *Energy Environ Sci* **11**, 286–293 (2018).
75. Wang, X., Tang, R., Wu, C., Zhu, C. & Chen, T. Development of antimony sulfide–selenide $Sb_2(S, Se)_3$ -based solar cells. *Journal of Energy Chemistry* **27**, 713–721 (2018).

76. Zhang, Z., Zhu, Y., Zhong, Y., Zhou, W. & Shao, Z. Anion Doping: A New Strategy for Developing High-Performance Perovskite-Type Cathode Materials of Solid Oxide Fuel Cells. *Adv Energy Mater* **7**, (2017).
77. Zhang, P., Yang, J. & Wei, S. H. Manipulation of cation combinations and configurations of halide double perovskites for solar cell absorbers. *J Mater Chem A Mater* **6**, 1809–1815 (2018).
78. Sahu, M. *et al.* Triple perovskite-based triboelectric nanogenerator: a facile method of energy harvesting and self-powered information generator. *Mater Today Energy* **20**, 100639 (2021).
79. Kim, N. I. *et al.* Oxygen-deficient triple perovskites as highly active and durable bifunctional electrocatalysts for oxygen electrode reactions. *Sci Adv* **4**, (2018).
80. Reyna, Y. *et al.* Performance and stability of mixed FAPbI₃(0.85)MAPbBr₃(0.15) halide perovskite solar cells under outdoor conditions and the effect of low light irradiation. *Nano Energy* **30**, 570–579 (2016).
81. Yang, H., Cai, T., Dube, L. & Chen, O. Synthesis of double perovskite and quadruple perovskite nanocrystals through post-synthetic transformation reactions. *Chem Sci* **13**, 4874–4883 (2022).
82. Patil, J. V., Mali, S. S. & Hong, C. K. A thiourea additive-based quadruple cation lead halide perovskite with an ultra-large grain size for efficient perovskite solar cells. *Nanoscale* **11**, 21824–21833 (2019).
83. Susic, I., Gil-Escrig, L., Palazon, F., Sessolo, M. & Bolink, H. J. Quadruple-Cation Wide-Bandgap Perovskite Solar Cells with Enhanced Thermal Stability Enabled by Vacuum Deposition. *ACS Energy Lett* **7**, 1355–1363 (2022).
84. Zhang, W., Eperon, G. E. & Snaith, H. J. *Metal Halide Perovskites for Energy Applications*.
85. Zhou, Y. & Saliba, M. Zooming in on Metal Halide Perovskites: New Energy Frontiers Emerge. *ACS Energy Lett* **6**, 2750–2754 (2021).
86. Hao, J. & Xiao, X. Recent Development of Optoelectronic Application Based on Metal Halide Perovskite Nanocrystals. *Front Chem* **9**, (2022).

87. Dong, H. *et al.* Metal Halide Perovskite for next-generation optoelectronics: progresses and prospects. *eLight* 2023 3:1 **3**, 1–16 (2023).
88. Mohapatra, A., Kar, M. R. & Bhaumik, S. Recent Progress and Prospects on Metal Halide Perovskite Nanocrystals as Color Converters in the Fabrication of White Light-Emitting Diodes. *Frontiers in Electronic Materials* **2**, (2022).
89. Mohapatra, A., Kar, M. R. & Bhaumik, S. Recent Progress and Prospects on Metal Halide Perovskite Nanocrystals as Color Converters in the Fabrication of White Light-Emitting Diodes. *Frontiers in Electronic Materials* **2**, 9 (2022).
90. Duan, D. *et al.* Recent progress with one-dimensional metal halide perovskites: from rational synthesis to optoelectronic applications. *NPG Asia Materials* 2023 15:1 **15**, 1–22 (2023).
91. Meng, Q. *et al.* Effect of temperature on the performance of perovskite solar cells. *Journal of Materials Science: Materials in Electronics* **32**, 12784–12792 (2021).
92. Reddy, S. H., Di Giacomo, F. & Di Carlo, A. Low-Temperature-Processed Stable Perovskite Solar Cells and Modules: A Comprehensive Review. *Adv Energy Mater* **12**, 2103534 (2022).
93. Gupta, R. *et al.* Room temperature synthesis of perovskite (MAPbI₃) single crystal by anti-solvent assisted inverse temperature crystallization method. *J Cryst Growth* **537**, 125598 (2020).
94. Sunny, F. *et al.* Metal Halide Hybrid Perovskites. *Recent Advances in Multifunctional Perovskite Materials* (2022) doi:10.5772/INTECHOPEN.106410.
95. Yan, J. *et al.* Advances in the Synthesis of Halide Perovskite Single Crystals for Optoelectronic Applications. *Chemistry of Materials* (2022) doi:10.1021/ACS.CHEMMATER.2C03505/ASSET/IMAGES/LARGE/CM2C03505_0020.JPEG.
96. Cai, Y. *et al.* Graded 2D/3D (CF₃-PEA)₂FA_{0.85}MA_{0.15}Pb₂I₇/FA_{0.85}MA_{0.15}PbI₃ heterojunction for stable perovskite solar cell with an efficiency over 23.0%. *Journal of Energy Chemistry* **65**, 480–489 (2022).
97. Kahwagi, R. F., Thornton, S. T., Smith, B. & Koleilat, G. I. Dimensionality engineering of metal halide perovskites. *Frontiers of Optoelectronics* **13**, 196–224 (2020).

98. Wang, F. *et al.* 2D-Quasi-2D-3D Hierarchy Structure for Tin Perovskite Solar Cells with Enhanced Efficiency and Stability. *Joule* **2**, 2732–2743 (2018).
99. Qin, Z. *et al.* Revealing the Origin of Luminescence Center in 0D Cs₄PbBr₆ Perovskite. *Chemistry of Materials* (2019) doi:10.1021/acs.chemmater.9b03426.
100. Cao, L. *et al.* Recent progress in all-inorganic metal halide nanostructured perovskites: Materials design, optical properties, and application. *Front Phys (Beijing)* **16**, (2021).
101. Xu, Y., Cao, M. & Huang, S. Recent advances and perspective on the synthesis and photocatalytic application of metal halide perovskite nanocrystals. *Nano Res* **14**, 3773–3794 (2021).
102. Seok, S. Il & Guo, T. F. Halide perovskite materials and devices. *MRS Bull* **45**, 427–430 (2020).
103. Zhang, J., Shum, P. P. & Su, L. A review of geometry-confined perovskite morphologies: From synthesis to efficient optoelectronic applications. *Nano Res* **15**, 7402–7431 (2022).
104. Parikh, N. *et al.* Two-dimensional halide perovskite single crystals: principles and promises. *Emergent Mater* **4**, 865–880 (2021).
105. Xu, L. J., Worku, M., He, Q. & Ma, B. Advances in light-emitting metal-halide perovskite nanocrystals. *MRS Bull* **45**, 458–466 (2020).
106. Xie, Y., Zhou, A., Zhang, X., Ou, Q. & Zhang, S. Metal cation substitution of halide perovskite nanocrystals. *Nano Res* **15**, 6522–6550 (2022).
107. Sun, S. *et al.* 0D Perovskites: Unique Properties, Synthesis, and Their Applications. *Advanced Science* vol. 8 Preprint at <https://doi.org/10.1002/advs.202102689> (2021).
108. Zhang, J. *et al.* Low-dimensional halide perovskites and their advanced optoelectronic applications. *Nano-Micro Letters* vol. 9 Preprint at <https://doi.org/10.1007/s40820-017-0137-5> (2017).
109. Zhu, T. & Gong, X. Low-dimensional perovskite materials and their optoelectronics. *InfoMat* vol. 3 1039–1069 Preprint at <https://doi.org/10.1002/inf2.12211> (2021).
110. Yang, J. *et al.* Stable, High-Sensitivity and Fast-Response Photodetectors Based on Lead-Free Cs₂AgBiBr₆ Double Perovskite Films. *Adv Opt Mater* **7**, (2019).

111. Wooster, W. A. & M, C. K. Crystal Structure and Photoconductivity of Cæsium Plumbohalides. *Nature 1958 182:4647* **182**, 1436–1436 (1958).
112. Weber, D. CH₃NH₃SnBr_xI_{3-x} (x = 0–3), ein Sn(II)-System mit kubischer Perowskitstruktur. *Zeitschrift für Naturforschung - Section B Journal of Chemical Sciences* **33**, 862–865 (1978).
113. Mitzi, D. B., Feild, C. A., Harrison, W. T. A. & Guloy, A. M. Conducting tin halides with a layered organic-based perovskite structure. *Nature 1994 369:6480* **369**, 467–469 (1994).
114. Kagan, C. R., Mitzi, D. B. & Dimitrakopoulos, C. D. Organic-inorganic hybrid materials as semiconducting channels in thin-film field-effect transistors. *Science* **286**, 945–947 (1999).
115. Mitzi, D. B., Chondroudis, K. & Kagan, C. R. Organic-inorganic electronics. *IBM J Res Dev* **45**, 29–45 (2001).
116. Green, M. A., Ho-Baillie, A. & Snaith, H. J. The emergence of perovskite solar cells. *Nature Photonics 2014 8:7* **8**, 506–514 (2014).
117. Kojima, A., Teshima, K., Shirai, Y. & Miyasaka, T. Organometal halide perovskites as visible-light sensitizers for photovoltaic cells. *J Am Chem Soc* **131**, 6050–6051 (2009).
118. Tan, Z. K. *et al.* Bright light-emitting diodes based on organometal halide perovskite. *Nat Nanotechnol* **9**, 687–692 (2014).
119. Protesescu, L. *et al.* Nanocrystals of Cesium Lead Halide Perovskites (CsPbX₃, X = Cl, Br, and I): Novel Optoelectronic Materials Showing Bright Emission with Wide Color Gamut. *Nano Lett* **15**, 3692–3696 (2015).
120. Zhang, F. *et al.* Brightly luminescent and color-tunable colloidal CH₃NH₃PbX₃ (X = Br, I, Cl) quantum dots: Potential alternatives for display technology. *ACS Nano* **9**, 4533–4542 (2015).
121. Akkerman, Q. A. *et al.* Tuning the optical properties of cesium lead halide perovskite nanocrystals by anion exchange reactions. *J Am Chem Soc* **137**, 10276–10281 (2015).
122. Schmidt, L. C. *et al.* Nontemplate synthesis of CH₃NH₃PbBr₃ perovskite nanoparticles. *J Am Chem Soc* **136**, 850–853 (2014).
123. Tyagi, P., Arveson, S. M. & Tisdale, W. A. Colloidal Organohalide Perovskite Nanoplatelets Exhibiting Quantum Confinement. *J Phys Chem Lett* **6**, 1911–1916 (2015).

124. Xiao, Z., Meng, W., Wang, J., Mitzi, D. B. & Yan, Y. Searching for promising new perovskite-based photovoltaic absorbers: the importance of electronic dimensionality. *Mater Horiz* **4**, 206–216 (2017).
125. Protesescu, L. *et al.* Nanocrystals of Cesium Lead Halide Perovskites (CsPbX₃, X = Cl, Br, and I): Novel Optoelectronic Materials Showing Bright Emission with Wide Color Gamut. *Nano Lett* **15**, 3692–3696 (2015).
126. Deschler, F. *et al.* High photoluminescence efficiency and optically pumped lasing in solution-processed mixed halide perovskite semiconductors. *Journal of Physical Chemistry Letters* **5**, 1421–1426 (2014).
127. Talapin, D. V., Lee, J. S., Kovalenko, M. V. & Shevchenko, E. V. Prospects of colloidal nanocrystals for electronic and optoelectronic applications. *Chem Rev* **110**, 389–458 (2010).
128. Jung, E. H. *et al.* Efficient, stable and scalable perovskite solar cells using poly(3-hexylthiophene). *Nature* **567**, 511–515 (2019).
129. Tan, H. *et al.* Efficient and stable solution-processed planar perovskite solar cells via contact passivation. *Science (1979)* **355**, 722–726 (2017).
130. Kojima, A., Teshima, K., Shirai, Y. & Miyasaka, T. Organometal halide perovskites as visible-light sensitizers for photovoltaic cells. *J Am Chem Soc* **131**, 6050–6051 (2009).
131. Furukawa, H., Cordova, K. E., O’Keeffe, M. & Yaghi, O. M. The chemistry and applications of metal-organic frameworks. *Science (1979)* **341**, (2013).
132. Kieslich, G., Sun, S. & Cheetham, A. K. Solid-state principles applied to organic–inorganic perovskites: new tricks for an old dog. *Chem Sci* **5**, 4712–4715 (2014).
133. Jeon, N. J. *et al.* Solvent engineering for high-performance inorganic–organic hybrid perovskite solar cells. *Nature Materials* **2014** *13*:9 **13**, 897–903 (2014).
134. Zhou, H. *et al.* Photovoltaics. Interface engineering of highly efficient perovskite solar cells. *Science* **345**, 542–546 (2014).
135. Chen, D. *et al.* *Brightness and Lifetime Improved Light-Emitting Diodes from Sr-Doped Quasi-Two-Dimensional Perovskite Layers.* vol. 28 <http://creativecommons.org/licenses/by/4.0/> (2023).

136. Chen, D. *et al.* *Brightness and Lifetime Improved Light-Emitting Diodes from Sr-Doped Quasi-Two-Dimensional Perovskite Layers.* vol. 28 <http://creativecommons.org/licenses/by/4.0/> (2023).
137. Zhang, H. *et al.* Spectrally Stable Blue Light-Emitting Diodes Based on All-Inorganic Halide Perovskite Films. *Nanomaterials* **12**, 2906 (2022).
138. Miao, Y. *et al.* Microcavity top-emission perovskite light-emitting diodes. *Light Sci Appl* **9**, 89–89 (2020).
139. Sun, C. *et al.* High-performance large-area quasi-2D perovskite light-emitting diodes. *Nat Commun* **12**, (2021).
140. Liu, R. & Xu, K. Blue perovskite light-emitting diodes (LEDs): A minireview. <https://doi.org/10.1080/10739149.2020.1762643> **48**, 616–636 (2020).
141. Zhao, C., Zhang, D. & Qin, C. Perovskite Light-Emitting Diodes. *CCS Chemistry* **2**, 859–869 (2020).
142. Wu, X. gang *et al.* Revealing the vertical structure of in-situ fabricated perovskite nanocrystals films toward efficient pure red light-emitting diodes. *Fundamental Research* (2022) doi:10.1016/J.FMRE.2022.05.004.
143. Wang, H. *et al.* In-situ growth of low-dimensional perovskite-based insular nanocrystals for highly efficient light emitting diodes. *Light Sci Appl* **12**, 2047–7538 (2023).
144. (1) Perovskite light-emitting diodes based on solution-processed self-organized multiple quantum wells | Request PDF. https://www.researchgate.net/publication/316641956_Perovskite_light-emitting_diodes_based_on_solution-processed_self-organized_multiple_quantum_wells.
145. High-Quality Perovskite Films for Efficient and Stable Light-Emitting Diodes - Heyong Wang - Google Books. [https://books.google.com.sa/books?id=SrgKEAAQBAJ&pg=PA59&lpg=PA59&dq=Wang,+N.+et+al.+Perovskite+light-emitting+diodes+based+on+solution-processed+selforganized+multiple+quantum+wells.+Nat.+Photonics+10,+699-704+\(2016\).&source=bl&ots=4h7jFDQE3P&sig=ACfU3U0Z5ECgJYxwi2KAQ04dqAR8kYcMQ&hl=en&sa=X&ved=2ahUKEwiT7MXO19f-AhU6gP0HHcEDBsEQ6AF6BAGcEAM#v=onepage&q=Wang%2C%20N.%20et%20al.%20Perovskite%20light-emitting%20diodes%20based%20on%20solution-](https://books.google.com.sa/books?id=SrgKEAAQBAJ&pg=PA59&lpg=PA59&dq=Wang,+N.+et+al.+Perovskite+light-emitting+diodes+based+on+solution-processed+selforganized+multiple+quantum+wells.+Nat.+Photonics+10,+699-704+(2016).&source=bl&ots=4h7jFDQE3P&sig=ACfU3U0Z5ECgJYxwi2KAQ04dqAR8kYcMQ&hl=en&sa=X&ved=2ahUKEwiT7MXO19f-AhU6gP0HHcEDBsEQ6AF6BAGcEAM#v=onepage&q=Wang%2C%20N.%20et%20al.%20Perovskite%20light-emitting%20diodes%20based%20on%20solution-)

- processed%20selforganized%20multiple%20quantum%20wells.%20Nat.%20Photonics%2010%2C%20699-704%20(2016).&f=false.
146. Han, D. *et al.* Efficient light-emitting diodes based on in situ fabricated FAPbBr₃ nanocrystals: The enhancing role of the ligand-assisted reprecipitation process. *ACS Nano* **12**, 8808–8816 (2018).
 147. Liu, Y. *et al.* Efficient blue light-emitting diodes based on quantum-confined bromide perovskite nanostructures. *Nat Photonics* **13**, 760–764 (2019).
 148. Cao, Y. *et al.* Perovskite light-emitting diodes based on spontaneously formed submicrometre-scale structures. *Nature* **562**, 249–253 (2018).
 149. Perovskite Photovoltaics and Optoelectronics: From Fundamentals to Advanced ... - Tsutomu Miyasaka - Google Books. [https://books.google.com.sa/books?id=8RdNEAAAQBAJ&pg=PA373&lpg=PA373&dq=Wang,+N.+et+al.+Perovskite+light-emitting+diodes+based+on+solution-processed+selforganized+multiple+quantum+wells.+Nat.+Photonics+10,+699-704+\(2016\).&source=bl&ots=PAD9KYncZM&sig=ACfU3U1KC38LWgai3yiXRvVbKoZG8i7wK0Q&hl=en&sa=X&ved=2ahUKEwji9Lbf19f-AhVC7rsIHYNdDVY4ChDoAXoECAMQAw#v=onepage&q=Wang%2C%20N.%20et%20al.%20Perovskite%20light-emitting%20diodes%20based%20on%20solution-processed%20selforganized%20multiple%20quantum%20wells.%20Nat.%20Photonics%2010%2C%20699-704%20\(2016\).&f=false](https://books.google.com.sa/books?id=8RdNEAAAQBAJ&pg=PA373&lpg=PA373&dq=Wang,+N.+et+al.+Perovskite+light-emitting+diodes+based+on+solution-processed+selforganized+multiple+quantum+wells.+Nat.+Photonics+10,+699-704+(2016).&source=bl&ots=PAD9KYncZM&sig=ACfU3U1KC38LWgai3yiXRvVbKoZG8i7wK0Q&hl=en&sa=X&ved=2ahUKEwji9Lbf19f-AhVC7rsIHYNdDVY4ChDoAXoECAMQAw#v=onepage&q=Wang%2C%20N.%20et%20al.%20Perovskite%20light-emitting%20diodes%20based%20on%20solution-processed%20selforganized%20multiple%20quantum%20wells.%20Nat.%20Photonics%2010%2C%20699-704%20(2016).&f=false).
 150. Lei, L., Dong, Q., Gundogdu, K. & So, F. Metal Halide Perovskites for Laser Applications. *Adv Funct Mater* **31**, (2021).
 151. Hu, Z. *et al.* Advances in metal halide perovskite lasers: synthetic strategies, morphology control, and lasing emission. *AdPho* **3**, 034002 (2021).
 152. Zhao, F. *et al.* Toward Continuous-Wave Pumped Metal Halide Perovskite Lasers: Strategies and Challenges. *ACS Nano* (2021) doi:10.1021/ACSNANO.1C11539/ASSET/IMAGES/LARGE/NN1C11539_0016.JPEG.
 153. Liu, A. *et al.* Metal Halide Perovskites toward Electrically Pumped Lasers. *Laser Photon Rev* **16**, (2022).
 154. Hao, J. & Xiao, X. Recent Development of Optoelectronic Application Based on Metal Halide Perovskite Nanocrystals. *Front Chem* **9**, (2021).

155. Hu, Z. *et al.* Robust Cesium Lead Halide Perovskite Microcubes for Frequency Upconversion Lasing. *Adv Opt Mater* **5**, (2017).
156. Liao, Q., Jin, X. & Fu, H. Tunable Halide Perovskites for Miniaturized Solid-State Laser Applications. *Adv Opt Mater* **7**, (2019).
157. Yang, M. *et al.* Advances of metal halide perovskite large-size single crystals in photodetectors: from crystal materials to growth techniques. *J Mater Chem C Mater* (2023) doi:10.1039/D2TC04913A.
158. Xia, B. *et al.* Flexible Metal Halide Perovskite Photodetector Arrays via Photolithography and Dry Lift-Off Patterning. *Adv Eng Mater* **24**, (2022).
159. Veeramalai, C. P. *et al.* Lead halide perovskites for next-generation self-powered photodetectors: a comprehensive review. *Photonics Research, Vol. 9, Issue 6, pp. 968-991* **9**, 968–991 (2021).
160. Raza, E., Ahmad, Z., Mishra, A. & Aziz, F. Metal halide-based photodetector using one-dimensional MAPbI₃ micro rods. *Journal of Materials Science: Materials in Electronics* **31**, 12109–12115 (2020).
161. Mei, F. *et al.* Recent progress in perovskite-based photodetectors: The design of materials and structures. *Adv Phys X* **4**, (2019).
162. Miao, J. & Zhang, F. Recent progress on highly sensitive perovskite photodetectors. *J Mater Chem C Mater* **7**, 1741–1791 (2019).
163. Liu, Z. *et al.* Metal Halide Perovskite and Phosphorus Doped g-C₃N₄ Bulk Heterojunctions for Air-Stable Photodetectors. *ACS Energy Lett* **4**, 2315–2322 (2019).
164. 王焯 *et al.* Metal halide perovskite photodetectors: Material features and device engineering. *中国物理B* **28**, 18502–018502 (2019).
165. High Performance and Stable All-Inorganic Metal Halide Perovskite-Based Photodetectors for Optical Communication Applications - Universidad de Chile. https://bibliotecadigital.uchile.cl/discovery/fulldisplay?docid=cdi_swepub_primary_oai_DiVA_org_liu_151638&context=PC&vid=56UDC_INST:56UDC_INST&lang=es&adaptor=Primo%20Central&tab=Everything&query=sub,exact,%20Electrical%20Engineering,%20Electronic%20Engineering,%20Information%20Engineering,AND&mode=advanced.

166. Wang, H. P. *et al.* Low-Dimensional Metal Halide Perovskite Photodetectors. *Advanced Materials* **33**, (2021).
167. Xie, H. *et al.* MXene-based metal halide perovskite vertical field-effect transistors: Toward high current-density and high photodetection performance. *Appl Phys Lett* **122**, 153301 (2023).
168. Yu, J. *et al.* Perovskite CsPbBr₃ crystals: Growth and applications. *J Mater Chem C Mater* **8**, 6326–6341 (2020).
169. Wang, H. & Kim, D. H. Perovskite-based photodetectors: Materials and devices. *Chem Soc Rev* **46**, 5204–5236 (2017).
170. Zhou, Y., Herz, L. M., Jen, A. K. Y. & Saliba, M. Advances and challenges in understanding the microscopic structure–property–performance relationship in perovskite solar cells. *Nature Energy* **2022 7:9 7**, 794–807 (2022).
171. Momma, K. & Izumi, F. VESTA 3 for three-dimensional visualization of crystal, volumetric and morphology data. *urn:issn:0021-8898* **44**, 1272–1276 (2011).
172. Goldschmidt, V. M. Die Gesetze der Krystallochemie. *Naturwissenschaften* **14**, 477–485 (1926).
173. Goldschmidt, V. M. Die Gesetze der Krystallochemie. *Naturwissenschaften* **14**, 477–485 (1926).
174. Saparov, B. & Mitzi, D. B. Organic-Inorganic Perovskites: Structural Versatility for Functional Materials Design. *Chem Rev* **116**, 4558–4596 (2016).
175. Shannon, R. D. & IUCr. Revised effective ionic radii and systematic studies of interatomic distances in halides and chalcogenides. *urn:issn:0567-7394* **32**, 751–767 (1976).
176. George, J. *et al.* The Limited Predictive Power of the Pauling Rules. *Angewandte Chemie International Edition* **59**, 7569–7575 (2020).
177. Travis, W., Glover, E. N. K., Bronstein, H., Scanlon, D. O. & Palgrave, R. G. On the application of the tolerance factor to inorganic and hybrid halide perovskites: a revised system. *Chem Sci* **7**, 4548–4556 (2016).

178. Zhou, Y. *et al.* Manipulating Crystallization of Organolead Mixed-Halide Thin Films in Antisolvent Baths for Wide-Bandgap Perovskite Solar Cells. *ACS Appl Mater Interfaces* **8**, 2232–7 (2016).
179. Yan, J. *et al.* Advances in the Synthesis of Halide Perovskite Single Crystals for Optoelectronic Applications. *Chemistry of Materials* **35**, 2683–2712 (2023).
180. Liu, Y. *et al.* Steady and transient optical properties of CsPbBr₃/Pb₃(PO₄)₂ perovskite quantum dots for white light-emitting diodes. *J Mater Chem C Mater* **10**, 16679–16686 (2022).
181. Wurfel, P. The chemical potential of radiation. *Journal of Physics C: Solid State Physics* **15**, 3967 (1982).
182. Kirchartz, T., Márquez, J. A., Stolterfoht, M. & Unold, T. Photoluminescence-Based Characterization of Halide Perovskites for Photovoltaics. *Adv. Energy Mater.* 1904134 (2020).
183. Chen, W. *et al.* Nonlinear Photonics Using Low-Dimensional Metal-Halide Perovskites: Recent Advances and Future Challenges. *Advanced Materials* **33**, 2004446 (2021).
184. Ferrando, A., Martínez Pastor, J. P. & Suárez, I. Toward Metal Halide Perovskite Nonlinear Photonics. *Journal of Physical Chemistry Letters* **9**, 5612–5623 (2018).
185. Xing, G. *et al.* Low-temperature solution-processed wavelength-tunable perovskites for lasing. *Nature Materials* 2014 13:5 **13**, 476–480 (2014).
186. Deschler, F. *et al.* High photoluminescence efficiency and optically pumped lasing in solution-processed mixed halide perovskite semiconductors. *Journal of Physical Chemistry Letters* **5**, 1421–1426 (2014).
187. Zhang, Q., Ha, S. T., Liu, X., Sum, T. C. & Xiong, Q. Room-temperature near-infrared high-Q perovskite whispering-gallery planar nanolasers. *Nano Lett* **14**, 5995–6001 (2014).
188. March, S. A. *et al.* Simultaneous observation of free and defect-bound excitons in CH₃NH₃PbI₃ using four-wave mixing spectroscopy. *Scientific Reports* 2016 6:1 **6**, 1–7 (2016).

189. March, S. A. *et al.* Four-wave mixing in perovskite photovoltaic materials reveals long dephasing times and weaker many-body interactions than GaAs. *ACS Photonics* **4**, 1515–1521 (2016).
190. Maehrlein, S. F. *et al.* Decoding ultrafast polarization responses in lead halide perovskites by the two-dimensional optical Kerr effect. *Proc Natl Acad Sci U S A* **118**, e2022268118 (2021).
191. Huber, L. *et al.* 2D Optical- and THz-Kerr Effect in Lead Halide Perovskites. *International Conference on Infrared, Millimeter, and Terahertz Waves, IRMMW-THz 2021-August*, (2021).
192. Sorokin, E., Naumov, S. & Sorokina, I. T. Ultrabroadband infrared solid-state lasers. *IEEE Journal on Selected Topics in Quantum Electronics* **11**, 690–712 (2005).
193. Kovalenko, M. V., Protesescu, L. & Bodnarchuk, M. I. Properties and potential optoelectronic applications of lead halide perovskite nanocrystals. *Science* **358**, 745–750 (2017).
194. Shamsi, J., Urban, A. S., Imran, M., De Trizio, L. & Manna, L. Metal Halide Perovskite Nanocrystals: Synthesis, Post-Synthesis Modifications, and Their Optical Properties. *Chem Rev* **119**, 3296–3348 (2019).
195. Zhang, W., Eperon, G. E. & Snaith, H. J. Metal halide perovskites for energy applications. *Nat Energy* **1**, (2016).
196. Gao, P., Bin Mohd Yusoff, A. R. & Nazeeruddin, M. K. Dimensionality engineering of hybrid halide perovskite light absorbers. *Nature Communications* *2018 9:1* **9**, 1–14 (2018).
197. Wang, C. *et al.* Crystal structure engineering of metal halide perovskites for photocatalytic organic synthesis. *Chemical Communications* **59**, 3122–3125 (2023).
198. Dipta, S. S. & Uddin, A. Stability Issues of Perovskite Solar Cells: A Critical Review. *Energy Technology* **9**, 2100560 (2021).
199. Zhou, Y. & Zhao, Y. Chemical stability and instability of inorganic halide perovskites. *Energy Environ Sci* **12**, 1495–1511 (2019).
200. Zhou, Y., Sternlicht, H. & Padture, N. P. Transmission Electron Microscopy of Halide Perovskite Materials and Devices. *Joule* **3**, 641–661 (2019).

201. Zhou, Y., Zhou, H., Deng, J., Cha, W. & Cai, Z. Decisive Structural and Functional Characterization of Halide Perovskites with Synchrotron. *Matter* **2**, 360–377 (2020).
202. Stranks, S. D. & Snaith, H. J. Metal-halide perovskites for photovoltaic and light-emitting devices. *Nat Nanotechnol* **10**, 391–402 (2015).
203. Acta crystallographica. Section A, Crystal physics, diffraction, theoretical and general crystallography | Welch Medical Library. <https://welch.jhmi.edu/journal?t=Acta%20crystallographica.%20Section%20A%2C%20Crystal%20physics%2C%20diffraction%2C%20theoretical%20and%20general%20crystallography>.
204. Azadeh, M. PIN and APD Detectors. 157–175 (2009) doi:10.1007/978-1-4419-0304-4_6.
205. Azadeh, M. Fiber Optic Communications: A Review. 1–27 (2009) doi:10.1007/978-1-4419-0304-4_1.
206. Senior, J. M. & Jamro, M. Yousif. Optical fiber communications : principles and practice. 1075 (2009).
207. Senior, J. M. & Jamro, M. Y. Optical fibre communications Principles and Practices. (1976).
208. Zenk, H. Ionization by quantized electromagnetic fields: The photoelectric effect. *Reviews in Mathematical Physics* **20**, 367–406 (2008).
209. Optical fiber communications : Keiser, Gerd : Free Download, Borrow, and Streaming : Internet Archive. https://archive.org/details/opticalfibercomm0000keis_j3m4.
210. Juntunen, M. A. *et al.* Near-unity quantum efficiency of broadband black silicon photodiodes with an induced junction. *Nature Photonics* 2016 10:12 **10**, 777–781 (2016).
211. Popoola, A. J., Gondal, M. A., Popoola, I. K., Oloore, L. E. & Bakr, O. M. Fabrication of bifacial sandwiched heterojunction photoconductor – Type and MAI passivated photodiode – Type perovskite photodetectors. *Org Electron* **84**, 105730 (2020).
212. Supasai, T., Rujisamphan, N., Ullrich, K., Chemseddine, A. & Dittrich, T. Formation of a passivating CH₃NH₃PbI₃/PbI₂ interface during moderate heating of CH₃NH₃PbI₃ layers. *Appl Phys Lett* **103**, 183906 (2013).

213. Tang, Z. *et al.* Modulations of various alkali metal cations on organometal halide perovskites and their influence on photovoltaic performance. *Nano Energy* **45**, 184–192 (2018).
214. Cao, J., Tao, S. X., Bobbert, P. A., Wong, C. P. & Zhao, N. Interstitial Occupancy by Extrinsic Alkali Cations in Perovskites and Its Impact on Ion Migration. *Advanced Materials* **30**, (2018).
215. Alahbakhshi, M. *et al.* Bright and Effectual Perovskite Light-Emitting Electrochemical Cells Leveraging Ionic Additives. *ACS Energy Lett* **4**, 2922–2928 (2019).
216. Phung, N. *et al.* The Doping Mechanism of Halide Perovskite Unveiled by Alkaline Earth Metals. *J Am Chem Soc* **142**, 2364–2374 (2020).
217. Zhou, Y., Chen, J., Bakr, O. M. & Sun, H. T. Metal-Doped Lead Halide Perovskites: Synthesis, Properties, and Optoelectronic Applications. *Chemistry of Materials* **30**, 6589–6613 (2018).
218. Yang, F. *et al.* Magnesium-Doped MAPbI₃ Perovskite Layers for Enhanced Photovoltaic Performance in Humid Air Atmosphere. *ACS Appl Mater Interfaces* **10**, 24543–24548 (2018).
219. Casillas-Trujillo, L. *et al.* Experimental and theoretical evidence of charge transfer in multi-component alloys – how chemical interactions reduce atomic size mismatch. *Mater Chem Front* **5**, 5746–5759 (2021).
220. Tseng, T. C. *et al.* Charge-transfer-induced structural rearrangements at both sides of organic/metal interfaces. *Nature Chemistry* **2**, 374–379 (2010).
221. Jiang, J. *et al.* The Doping of Alkali Metal for Halide Perovskites. *ES Materials and Manufacturing* **7**, 25–33 (2020).
222. Luo, H. *et al.* Addition of Lithium Iodide into Precursor Solution for Enhancing the Photovoltaic Performance of Perovskite Solar Cells. *Energy Technology* **5**, 1814–1819 (2017).
223. Ke, W. *et al.* Employing Lead Thiocyanate Additive to Reduce the Hysteresis and Boost the Fill Factor of Planar Perovskite Solar Cells. *Advanced Materials* **28**, 5214–5221 (2016).

224. Zhang, M. *et al.* High-Performance Photodiode-Type Photodetectors Based on Polycrystalline Formamidinium Lead Iodide Perovskite Thin Films. *Scientific Reports* 2018 8:1 **8**, 1–9 (2018).
225. Kwon, K. C. *et al.* Inhibition of Ion Migration for Reliable Operation of Organolead Halide Perovskite-Based Metal/Semiconductor/Metal Broadband Photodetectors. *Adv Funct Mater* **26**, 4213–4222 (2016).
226. Elseman, A. M., Luo, L. & Song, Q. L. Self-doping synthesis of trivalent Ni₂O₃ as a hole transport layer for high fill factor and efficient inverted perovskite solar cells. *Dalton Transactions* **49**, 14243–14250 (2020).
227. Popoola, A. J., Gondal, M. A., Popoola, I. K., Oloore, L. E. & Bakr, O. M. Fabrication of bifacial sandwiched heterojunction photoconductor – Type and MAI passivated photodiode – Type perovskite photodetectors. *Org Electron* **84**, 105730 (2020).
228. Eames, C. *et al.* Ionic transport in hybrid lead iodide perovskite solar cells. *Nat Commun* **6**, (2015).
229. Eames, C. *et al.* Ionic transport in hybrid lead iodide perovskite solar cells. *Nature Communications* 2015 6:1 **6**, 1–8 (2015).
230. Hu, X. *et al.* High-Performance Flexible Broadband Photodetector Based on Organolead Halide Perovskite. *Adv Funct Mater* **24**, 7373–7380 (2014).
231. Li, T., Liu, M., Li, Q., Chen, R. & Liu, X. Hybrid photodetector based on CsPbBr₃ perovskite nanocrystals and PC71BM fullerene derivative. *Chem Phys Lett* **699**, 208–211 (2018).
232. Xue, J. *et al.* Narrowband Perovskite Photodetector-Based Image Array for Potential Application in Artificial Vision. *Nano Lett* **18**, 7628–7634 (2018).
233. Lim, J. W. *et al.* Self-powered reduced-dimensionality perovskite photodiodes with controlled crystalline phase and improved stability. *Nano Energy* **57**, 761–770 (2019).
234. Popoola, A., Gondal, M. A., Popoola, I. K. & Oloore, L. E. Self-Driven, Quadridirectional Carrier Transport, Bifacial MAPbI₃-Perovskites Photodiodes Fabricated via Laterally Aligned Interconnected Sandwiched Type Architecture. *ACS Appl Electron Mater* **2**, 2479–2488 (2020).

235. Du, S. *et al.* Oxide Semiconductor Phototransistor with Organolead Trihalide Perovskite Light Absorber. *Adv Electron Mater* **3**, 1600325 (2017).
236. Tong, G. *et al.* Enhancing Hybrid Perovskite Detectability in the Deep Ultraviolet Region with Down-Conversion Dual-Phase (CsPbBr₃-Cs₄PbBr₆) Films. *Journal of Physical Chemistry Letters* **9**, 1592–1599 (2018).
237. Li, S. *et al.* Fabrication of morphology-controlled and highly-crystallized perovskite microwires for long-term stable photodetectors. *Solar Energy Materials and Solar Cells* **191**, 275–282 (2019).
238. Dias, S. & Ganesh, N. Perovskite-Based Photodetectors in the Lateral Device Geometry. *J Electron Mater* **50**, 7214–7221 (2021).
239. Wang, Y. *et al.* Solution-Processed MoS₂/Organolead Trihalide Perovskite Photodetectors. *Advanced Materials* **29**, (2017).
240. Wu, L. *et al.* High-Sensitivity Light Detection via Gate Tuning of Organometallic Perovskite/PCBM Bulk Heterojunctions on Ferroelectric Pb_{0.92}La_{0.08}Zr_{0.52}Ti_{0.48}O₃ Gated Graphene Field Effect Transistors. *ACS Appl Mater Interfaces* **10**, 12824–12830 (2018).
241. Lin, D. *et al.* High-Performance Directly Patterned Nanograting Perovskite Photodetector with Interdigitated Electrodes. *Adv Opt Mater* **10**, 2201516 (2022).
242. Upadhyaya, A., Singh Negi, C. M., Yadav, A., Gupta, S. K. & Verma, A. S. I-V and impedance characterization of a solution processed perovskite-based heterojunction photodetector. *Superlattices Microstruct* **122**, 410–418 (2018).
243. Wang, Y. *et al.* Solution-Processed MoS₂/Organolead Trihalide Perovskite Photodetectors. *Advanced Materials* **29**, (2017).
244. Du, S. *et al.* Oxide Semiconductor Phototransistor with Organolead Trihalide Perovskite Light Absorber. *Adv Electron Mater* **3**, 1600325 (2017).
245. Sutherland, B. R. *et al.* Sensitive, Fast, and Stable Perovskite Photodetectors Exploiting Interface Engineering. *ACS Photonics* **2**, 1117–1123 (2015).

246. Li, D., Dong, G., Li, W. & Wang, L. High performance organic-inorganic perovskite-optocoupler based on low-voltage and fast response perovskite compound photodetector. *Scientific Reports* 2015 5:1 **5**, 1–6 (2015).
247. Ghosh, J., Natu, G. & Giri, P. K. Plasmonic hole-transport-layer enabled self-powered hybrid perovskite photodetector using a modified perovskite deposition method in ambient air. *Org Electron* **71**, 175–184 (2019).
248. Tong, G. *et al.* Enhancing Hybrid Perovskite Detectability in the Deep Ultraviolet Region with Down-Conversion Dual-Phase (CsPbBr₃-Cs₄PbBr₆) Films. *J Phys Chem Lett* **9**, 1592–1599 (2018).
249. Yu, J. *et al.* A high-performance self-powered broadband photodetector based on a CH₃NH₃PbI₃ perovskite/ZnO nanorod array heterostructure. *J Mater Chem C Mater* **4**, 7302–7308 (2016).
250. Li, X. *et al.* Healing All-Inorganic Perovskite Films via Recyclable Dissolution–Recrystallization for Compact and Smooth Carrier Channels of Optoelectronic Devices with High Stability. *Adv Funct Mater* **26**, 5903–5912 (2016).
251. Dong, Y. *et al.* Improving All-Inorganic Perovskite Photodetectors by Preferred Orientation and Plasmonic Effect. *Small* **12**, 5622–5632 (2016).
252. Xue, M. *et al.* Investigation of the stability for self-powered CsPbBr₃ perovskite photodetector with an all-inorganic structure. *Solar Energy Materials and Solar Cells* **187**, 69–75 (2018).

Vitae

Name : AbdurRahman Imam

Nationality : Nigerian

Date of Birth : 2/2/1987

Email : imamabdurrahman44@gmail.com

Permanent HomeAddress : Building No. 0346, Chief Imam's residence, Gwadara, Talata Mafara, Zamfara State, Nigeria.

Postal Address: : Department of Applied Sciences, Abdu Gusau Polytechnic, P.M.B 1021, along Sokoto-Gusau road, Talata Mafara, Zamfara State, Nigeria.

Academic Background

1. Master of Science, Physics 2021-2024
King Fahd University of Petroleum and Minerals, Dhahran, Saudi Arabia.
2. Bachelor of Science, Physics 2009-2012
Bayero University Kano, Nigeria.
3. National Diploma in Science Laboratory Technology 2006-2008
Abdu Gusau Polytechnic Talata Mafara, Nigeria.

Publications from This Work

1. **A. Imam**, M.A. Gondal, Y.S. Wudil, Systematic investigation of LiI incorporation effects into MAPbI₃-precursors for enhanced photodetection applications, *Applied Materials Today*, Volume 37, 2024, 102152, ISSN 2352-9407, <https://doi.org/10.1016/j.apmt.2024.102152>.
2. **Imam**, M.A. Gondal, Y.S. Wudil, “Enhanced Optoelectrical Properties of Single and Tandem Absorber Layer Photodetectors Based on Li-doped Halide Perovskite with Dual-Face Detection Potential”, Manuscript ID: el-2024-00598p, Status: Under Review, Submitted: on 04 April 2024 to ACS Applied Electronic Materials.

Other Publications

1. Y.S. Wudil, **A. Imam**, M.A. Gondal, U.F. Ahmad, Mohammed A. Al-Osta, “Application of machine learning regressors in estimating the thermoelectric performance of Bi₂Te₃-based materials”, *Sensors and Actuators A: Physical*, Volume 351, 2023, 114193, ISSN 0924-4247, <https://doi.org/10.1016/j.sna.2023.114193>.
2. U.F. Ahmad, Y.S. Wudil, **A. Imam**, N.F. Isa, M.A. Gondal, Mohammed A. Al-Osta, “Applications of carbon-based diamond detectors: A critical review”, *Materials Today Communications*, Volume 36, 2023, 106409, ISSN 2352-4928, <https://doi.org/10.1016/j.mtcomm.2023.106409>.
3. Al-Najjar, O.A., Wudil, Y.S., Al-Osta, **A. Imam**, M.A. et al. Laser-Induced Breakdown Spectroscopy-Based Assessment of Unconfined Compressive Strength of Normal and Chemically Stabilized Soils. *Arab J Sci Eng* 49, 1047–1061 (2024). <https://doi.org/10.1007/s13369-023-08055-6>.